Planar microwave resonators on $SrTiO_3$ substrates

Master-Thesis verfasst von
Vincent Engl

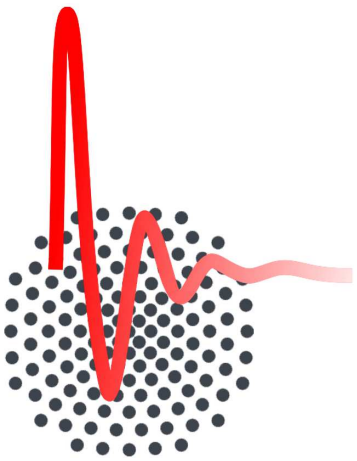

1. Physikalisches Institut
Universität Stuttgart

Hauptberichter:	**Prof. Dr. Martin Dressel**
Mitberichter:	**Prof. Dr. Jürgen Weis**
Betreuer:	**Dr. Marc Scheffler**

09. April 2019

Contents

1. Motivation

Complex oxide interfaces are an intriguing and highly up-to-date field of research in solid state physics driven forward by the recent progresses in oxide thin-film growth technology during the last decade [1, 2]. These interfaces can exhibit a variety of fascinating and unconventional electronic properties or phases such as superconductivity, ferroelectricity or magnetism which are not observed in their respective parent compounds. Said properties occur when reducing the dimensionality of an electronic structure leading to carrier confinement. Although there has been intensive research in the last years, there are still many open questions under heavy debate. Answers to these questions are of great potential not only for fundamental research but also for new useful device applications in the field of applied physics.

One particularly fascinating interface of this kind is the one between the two separately insulating complex perovskite oxides $LaAlO_3$ (LAO) and $SrTiO_3$ (STO), the so called LAO/STO interface [3]. Under the right conditions, a two-dimensional electron gas (2DEG) with highly conducting properties is formed in this heterointerface, although the materials LAO and STO are both separately band insulators. Electron-doping the interface leads to a carrier mobility exceeding values of $10\,000\,\mathrm{cm^2V^{-1}s^{-1}}$ [3]. The reasons for the rise of the 2DEG are still unknown as it could be oxygen vacancies in the STO substrate ('extrinsic'), the polar nature of the LAO layers ('intrinsic' or polar catastrophe model), an interplay of both of them or even structural deformations [4]. There is also 2D-superconductivity reported in the electron gas below a temperature of 200 mK [5]. When no external voltage is applied the temperature dependence of the superconducting gap Δ and the superfluid density ρ are reported to be consistent with a clean s-wave superconductor [6, 7]. The critical temperature T_c as well as the superfluid density are tunable upon applying an external electric field. This reveals a dome-shaped behavior on the charge carrier density n with a quantum critical point marking a superconductor to insulator transition [8, 9]. The normal conductivity is tunable as well making it possible to also drive a metal to insulator transition [10]. Besides the electrical conductivity and superconductivity, also ferromagnetic/electric orders [11, 12], a large negative in-plane magnetoresistance [13] and strong spin-orbit coupling [13, 14] were observed in the LAO/STO interface.

Planar microwave resonators are a powerful tool to study the electromagnetic properties of bulk as well as ultra thin samples as they offer direct experimental access to their properties. This has successfully been applied over the last decades with a variety of many different materials and measurement methods [15–19]. However, when it comes down to realizing a microwave resonator on the substrate STO, there are some difficulties. STO has a very high, anisotropic and temperature dependent dielectric constant ϵ_1 being 300 at room temperature and in the order of 10^4 at very low temperatures [20–22]. In addition to that, STO has a higher (and also temperature dependent) loss tangent $\tan\delta$ than the usual resonator substrates e.g. Al_2O_3 [23, 24]. This makes it enormously challenging to match the characteristic impedance

Z_0 of the resonator to the coaxial cable standard of $50\,\Omega$ and thus to realize microwave resonator operation. Nevertheless, it has been shown in a few previous works that it is still feasible not only for single STO [22, 25–27] but also for the interplay of LAO and STO [7, 28]. However, the frequency range achieved with the LAO/STO devices does not exceed values of $\nu \approx 400\,\mathrm{MHz}$, while the quality factors Q are relatively low compared to commonly used resonant devices. In the interest of revealing fundamental superconducting properties e.g. the superconducting gap energy Δ and developing new quantum electronic devices such as qubits [29], it is of great interest to expand the accessible frequency range to higher values and to increase the quality factors.

The approach to an LAO/STO resonator with experimental access to the LAO/STO interface in this work is to firstly realize superconducting resonators on STO with a known superconducting material. This is necessary to see if the resonator operation method is generally possible and to probe some standard resonator quantities, e.g. the quality factor Q. In a previous step before that, metallic coplanar resonators on STO have already been realized in a preceding bachelor project to probe the behavior in a broad temperature range from $300\,\mathrm{K}$ down to $15\,\mathrm{K}$ [27]. With the knowledge of these two steps, the long-term perspective of this thesis would be a gateable LAO/STO resonator where an ultra thin structure of LAO is deposited on a bulk substrate of STO letting the 2DEG form the actual resonator. The realization of the LAO/STO resonator would make it possible to probe the interesting quantities of the 2DEG, e.g. the superfluid density, critical temperature or superconducting gap energy in dependence of the frequency, temperature and electrostatic gating by monitoring the resonance frequencies and microwave losses of the resonator.

This thesis starts with an introduction to the theoretical principles necessary to understand the following chapters. Then, an introduction to the material STO and the state of art about microwave spectroscopy on the LAO/STO interface is presented. Afterwards, the development of possible resonator models is worked out. The main part of this thesis is the simulations done on the resonator models followed by experiments and respective discussion. The thesis is concluded with a summary and an outlook.

2. Theoretical principles

2.1. Dielectric properties of solids

The interaction of light and matter can be described macroscopically and microscopically. On the macroscopic scale, it is well described by the Maxwell equations [30] and by material parameters and equations. The Maxwell equations in matter are given by [31]

$$\nabla \cdot \mathbf{D} = 4\pi\rho\,, \tag{2.1}$$
$$\nabla \cdot \mathbf{B} = 0\,, \tag{2.2}$$
$$\nabla \times \mathbf{E} = -\frac{1}{c}\frac{\partial}{\partial t}\mathbf{B}\,, \tag{2.3}$$
$$\nabla \times \mathbf{H} = \frac{1}{c}\frac{\partial}{\partial t}\mathbf{D} + \frac{4\pi}{c}\mathbf{j}\,. \tag{2.4}$$

Here, $\mathbf{E}$ and $\mathbf{H}$ are the electric and the magnetic field and $\mathbf{D}$ and $\mathbf{B}$ are the displacement field and the magnetizing field, respectively. c is the speed of light, ρ is the charge density and $\mathbf{j} = \sigma\mathbf{E}$ is the current density induced by an applied electric field $\mathbf{E}$ connected to the electrical conductivity σ by Ohm's law [31].

When an insulator is penetrated by an electric field $\mathbf{E}$, it leads to a displacement of charges and therefore a polarization $\mathbf{P}$. The displacement and the magnetizing field are connected to the electric and magnetic field by material parameters as [31, 32]

$$\mathbf{D} = \epsilon\mathbf{E} = \mathbf{E} + 4\pi\mathbf{P}\,, \tag{2.5}$$
$$\mathbf{B} = \mu\mathbf{H} = \mathbf{H} + 4\pi\mathbf{M}\,. \tag{2.6}$$

$\mathbf{P}$ and $\mathbf{M}$ are the polarization and the magnetization, respectively. ϵ and μ are the characteristic material parameters permittivity and permeability, which are scalars for cubic crystals and amorphous solids ('electrically isotropic') [32]. To take phase shifts between the electric field $\mathbf{E}$ and the displacement field $\mathbf{D}$ into account, the dielectric constant (or dielectric function) gets defined as a complex quantity [31]

$$\hat{\epsilon} = \epsilon_1 + \mathrm{i}\epsilon_2 = \epsilon_1 + \mathrm{i}\frac{4\pi}{\omega}\sigma_1 = 1 + \mathrm{i}\frac{4\pi}{\omega}\hat{\sigma} \tag{2.7}$$

with the angular frequency ω of the applied electric field $\mathbf{E}$. In general, the permittivity describes how a material influences an external electric field. It is frequency dependent as it shows different effects of the material depending on frequency varying from dipole over ionic to electronic contributions [33]. When probing the electromagnetic properties of solids e.g. with planar microwave resonators, the permittivity $\hat{\epsilon}$ is of great interest as the real part of

the permittivity ϵ_1 gives information about the lossless dispersion and the imaginary part of the permittivity ϵ_2 gives information about the absorption losses of the material. The loss tangent of a material can be defined as [31]

$$\tan\delta = \frac{\epsilon_2}{\epsilon_1}\,. \tag{2.8}$$

Measuring the permittivity also gives direct access to the electrical conductivity $\hat{\sigma}$ (see equation (2.7)).

2.1.1. Ferro- and paraelectricity

Materials that have a spontaneous electric polarization even without an applied electric field are called pyroelectric. This behavior can only be present in a crystal that has one polar axis. If there are more than one polar axes, the material is piezoelectric and can thus change its polarization by mechanical deformation. A material is called ferroelectric (due to the phenomenological analogies to ferromagnetism) when the following two criteria are met: It has a spontaneous electric polarization even without an applied electric field and this polarization can be flipped with an oppositely directed electric field, meaning the polarization is reversible. Hence, all ferroelectrics are pyroelectrics but not vice versa. If a ferroelectric is warmed up above its material specific temperature T_C, the spontaneous polarization is lost and the material turns paraelectric with a static dielectric constant following the Curie-Weiss law [32]

$$\epsilon = \frac{a_0}{T - T_\mathrm{C}}\,. \tag{2.9}$$

Here, T is the temperature, a_0 is the Curie-constant and T_C is the Curie-temperature. Paraelectricity means the material can become polarized in an applied electric field even without permanent electric dipoles but the polarization is vanishing if the electric field is removed. The phase transition from the ferroelectric to the paraelectric state can be a phase transition of first or second order and is often accompanied by a structural phase transition [32].

2.2. Superconductivity

Superconductors are materials which have a vanishing DC-resistance below their specific critical temperature T_c. Thus, they are perfect conductors and perfect diamagnets with a magnetic susceptibility $\chi = -1$ as they form screening currents shielding out any external magnetic field from its inside (Meißner-Ochsenfeld effect). The vanishing DC-resistance makes them of great interest for spectroscopy measurements e.g. the conducting material of a planar microwave resonator can be superconducting. Besides a critical temperature T_c, superconductivity also gets destroyed by a critical magnetic field B_c or a critical current j_c. Since the discovery of superconductivity, several accepted theories describing this state have been evolved. On a macroscopic scale, one accepted theory is the London theory where a

two-fluid model with normal conducting charge carriers on the one hand and superconducting charge carriers on the other hand are assumed [34]. The density of superconducting charge carriers can empirically be described as

$$n_\mathrm{s}(T) = 1 - \left(\frac{T}{T_\mathrm{c}}\right)^4 . \tag{2.10}$$

The behavior of the superconducting charge carriers in an electric field is decribed by the first London equation [32, 35]

$$\frac{\partial}{\partial t}\mathbf{j}_\mathrm{s} = \frac{n_\mathrm{s} e^2}{m_\mathrm{s}}\mathbf{E} . \tag{2.11}$$

Here, $\mathbf{j}_\mathrm{s}$ is the superconducting current density and n_s the density of superconducting charge carriers with charge e and mass m_s. Plugging this equation into the third Maxwell equation (2.3) yields the second London equation

$$\nabla \times \mathbf{j}_\mathrm{s} = -\frac{n_\mathrm{s} e^2}{m_\mathrm{s} c}\mathbf{B} . \tag{2.12}$$

This equation describes the Meißner-Ochsenfeld effect and the small penetration of a magnetic field $\mathbf{B}$ into the superconductor as there has to be some interplay for the shielding currents to occur. Solving a differential equation obtained from the London and the Maxwell equations leads to the London penetration depth

$$\lambda_\mathrm{L}(T) = \sqrt{\frac{m_\mathrm{s} c^2}{4\pi e^2 n_\mathrm{s}(T)}} . \tag{2.13}$$

The London penetration depth describes the length scale on which the magnetic field has exponentially decreased to 1/e in the superconductor compared to the external field. It is temperature dependent since the superconducting charge carrier density heavily depends on temperature being maximum at $T = 0$ and vanishing at T_c. The Gorter-Casimir relation empirically describes this dependence for temperatures close to T_c as [36]

$$\lambda_\mathrm{L}(T) = \frac{\lambda_\mathrm{L}(0)}{\sqrt{1 - \left(\frac{T}{T_\mathrm{c}}\right)^4}} . \tag{2.14}$$

The temperature dependence of λ_L and of the superconducting charge carrier density n_s is plotted in figure 2.1.

A microscopic theory was found by Bardeen, Cooper and Schrieffer in their so called BCS-theory [37]. The main point of this theory is the formation of a bounded state with two electrons called Cooper-pair despite the repulsive Coulomb interaction between them. In a simple BCS-superconductor, they get formed by an interaction with phonons. A lattice deformation induced by a first electron leads to a positive polarization of the lattice attracting a second electron forming an electron-electron-pair. Electrons have an electrical charge of $-e$

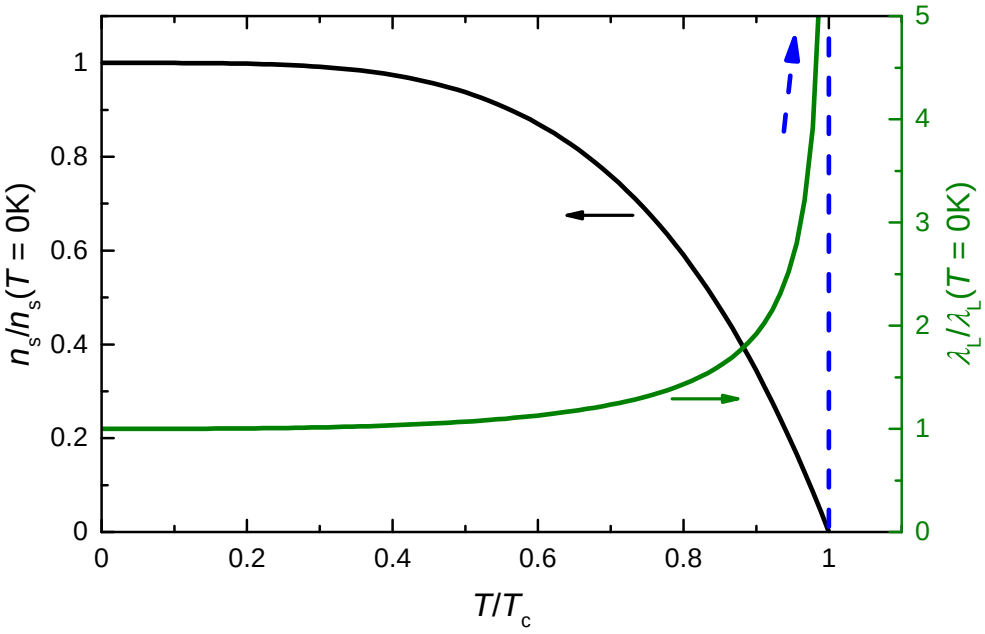

Fig. 2.1.: Temperature dependence of the normalized superconducting charge carrier density n_s and the normalized London penetration depth λ_L. At $T = T_\mathrm{c}$ the superconducting charge carrier density vanishes whereas the London penetration depth diverges.

and a spin of $S = 1/2$, thus Cooper-pairs have an electrical charge of $-2e$ and an integer spin (bosons). As the total wave function of a two-electron-system has to be antisymmetric and the spatial wave function is symmetric, the spin wave function of the Cooper-pairs has to be antisymmetric. Hence, the spin is $S = 0$ making them bosons. Bosons, unlike fermions, can occupy the same quantum state allowing them to condense into a collective macroscopic ground state. This coherent ground state can be described by a single macroscopic wave function [32]

$$\psi = \psi_0 \exp\left(\mathrm{i}\varphi(r)\right) = \sqrt{n_\mathrm{s}} \exp\left(\mathrm{i}\varphi(r)\right) \tag{2.15}$$

with $n_\mathrm{s} = |\psi_0|^2$. The existence of a macroscopic wave function is responsible for the variety of special properties a superconductor has. The energy required to break a Cooper-pair and excite the BCS-ground state is the energy gap Δ of a superconductor. With increasing temperature, the energy gap gets smaller vanishing at the transition temperature T_c. In the BCS-theory, there is a universal relation between the zero-temperature gap and the critical temperature written as [37]

$$\frac{\Delta_0}{k_\mathrm{B} T_\mathrm{c}} \approx 1.76\,. \tag{2.16}$$

This relation and describing the isotope effect ($T_\mathrm{c} \propto \omega_\mathrm{D} \propto M^{-1/2}$ with the Debye frequency ω_D and the isotope mass M) was one of the early successes of the BCS-theory.

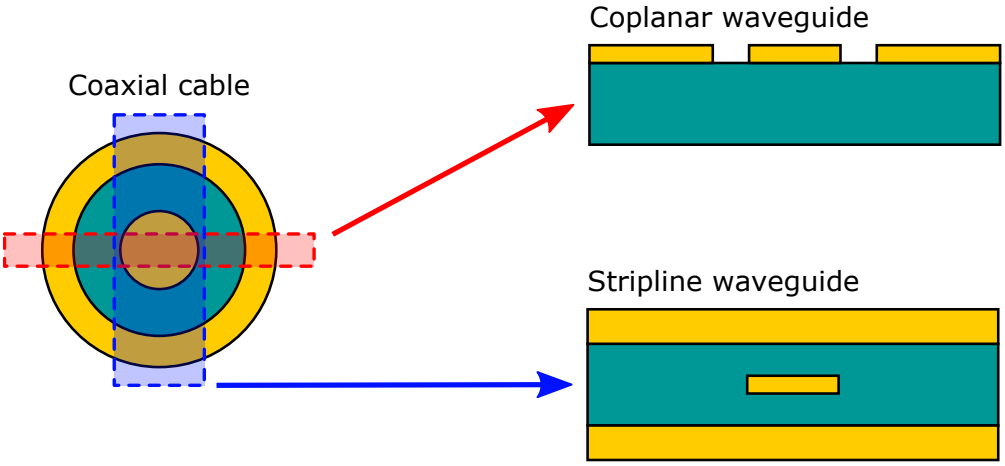

Fig. 2.2.: Schematic cross section of a basic coaxial cable and two planar waveguides: A coplanar waveguide on the upper-hand side and a stripline waveguide on the lower-hand side with their respective derivation from a coaxial cable.

2.3. Planar microwave resonators

Planar waveguides can carry energy in form of electromagnetic waves interacting with the surrounding matter making them a powerful tool to study the electromagnetic properties of dielectric solids. Probing of the materials is conctactless via the electric and magnetic fields and can ideally cover a broad frequency range [18, 38, 39]. Depending on the conducting material either being a superconductor [40, 41] or a metal [39, 42], a small or a very large temperature area can be accessed, respectively. The spectroscopy with planar microwave resonators not only allows probing of the dielectric but also of the conductor by using a known and ideally non-lossy dielectric. Their extremly versatile field of use and their usability in external magnetic fields make them also applicable e.g. for electron spin resonance (ESR) [39, 43, 44] spectroscopy.

In general, a planar waveguide can be understood as a transformation of a basic coaxial cable (see figure 2.2). The coplanar waveguide can be seen as a thin horizontal cut through the middle of the coaxial cable whereas the stripline waveguide can be understood as the coaxial cable squeezed flat. Both models therefore consist, like the coaxial cable, of an inner conductor, an outer conductor or ground planes and a dielectric which often is the sample under investigation. The sample can also be placed externally on top of the resonator to act as a perturbation to the unperturbated resonator [17].

2.3.1. Coplanar microwave resonators

In this work, coplanar microwave resonators are used to probe the material STO. Coplanar resonators have some advantages in their use: They can probe not only bulk samples but also thin films [45, 46] in a broad frequency range and reach substantial quality factors. Their small surface design makes them very compact and therefore accessible in nearly every setup ranging to very low temperatures e.g. in a dilution refrigerator and the sample is not

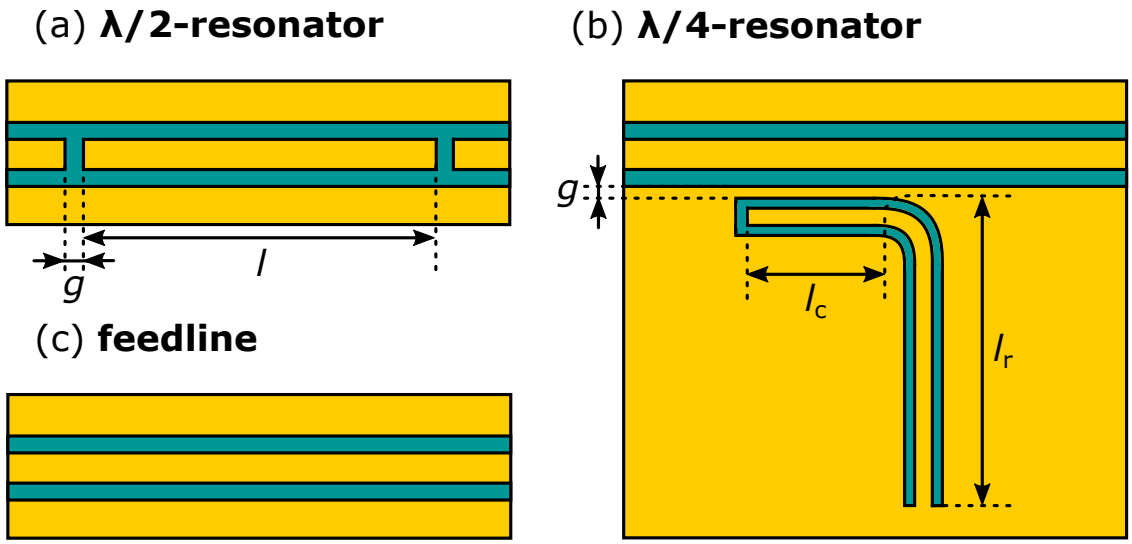

Fig. 2.3.: Schematic top view sketch of (a) a $\lambda/2$-resonator with length l and the coupling gap g (b) a $\lambda/4$-resonator with total length $l = l_c + l_r$, the coupling length l_c and the coupling gap g (c) a feedline.

required to cover the whole resonator chip, necessarily. In addition to that, the fabrication process is rather fast and easy [17, 19]. Because of said reasons and the fact that particularly with regard to the motivation, namely the LAO/STO interface, the realization of a gateable LAO/STO resonator is more suitable with the coplanar geometry, coplanar waveguides are used in the present work.

The transition from a coplanar waveguide to a coplanar $\lambda/2$-resonator is realized by the introduction of two capacitively coupling gaps forming an impedance mismatch in the inner conductor (see figure 2.3(a)). The length l from gap to gap where the microwave signal partially gets reflected forms the resonator. The size of the gaps g is a measure of the coupling strength into the resonator. There are resonances in the wave propagation when multiples of $\lambda/2$ of the microwave signal match the length l of the resonator and standing waves can occur.

Resonator operation is also possible with a $\lambda/4$ setup (see figure 2.3(b)). Here, on one end of the resonator, the signal gets coupled inductively from a feedline (see figure 2.3(c)) while the other end is left open (with respect to the magnetic field amplitude). The measure of the coupling strength is realized by the coupling length l_c of the parallel arm next to the feedline and the distance g between them. Resonances in this resonator appear if odd multiples of $\lambda/4$ match the complete resonator length $l = l_c + l_r$. The resonance conditions can be written as [47]

$$\nu_{0,n} = \frac{nc}{\sqrt{\epsilon_{\text{eff}}} l} \begin{cases} 1/2 & n = 1, 2, 3, \ldots \quad (\lambda/2\text{-resonators}) \\ 1/4 & n = 1, 3, 5, \ldots \quad (\lambda/4\text{-resonators}) \end{cases} \tag{2.17}$$

with the number of the mode n, the speed of light c, the effective dielectric constant ϵ_{eff} and the length of the resonator l. This is the condition for the resonance frequency where a standing

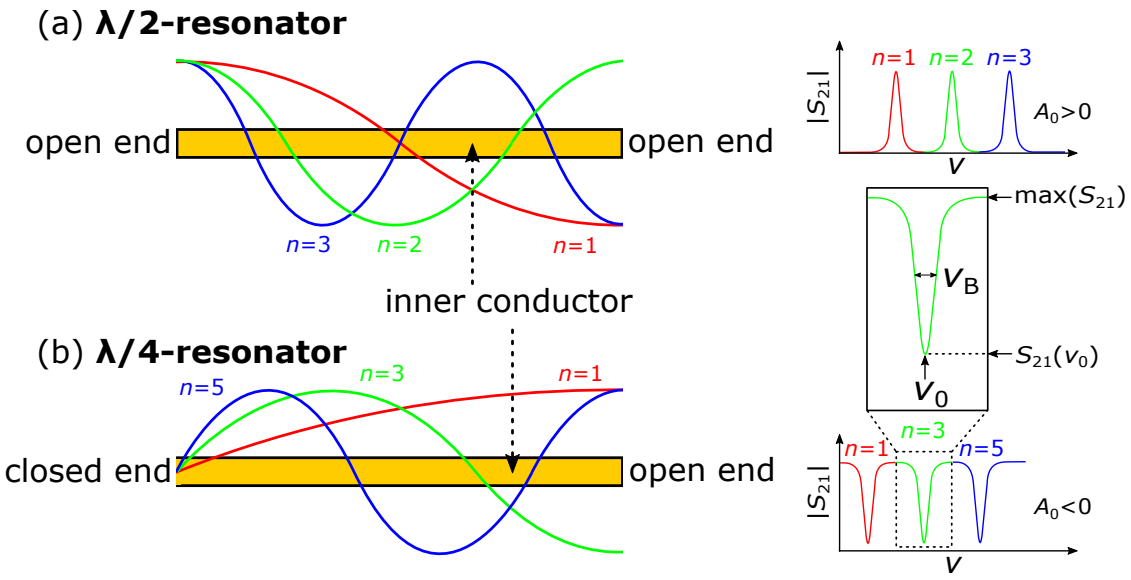

Fig. 2.4.: Electric field distribution and schematic transmission spectrum of the first three modes of (a) a coplanar $\lambda/2$-resonator and (b) a coplanar $\lambda/4$-resonator with identical resonator lengths l. The $\lambda/2$-resonator has two open ends and therefore two antinodes, whereas the $\lambda/4$-resonator has one closed and one open end and therefore a node at the closed and an antinode at the open end (and only odd modes excited).

wave and therefore constructive interference occurs. As one can see in equation (2.17), for $\lambda/4$-resonators, there are only odd modes n = 1,3,5,... because of the one open end whereas for the $\lambda/2$-resonators, every mode n = 1,2,3,... can be excited. The electric field distributions of the first three modes in a straight inner conductor of a $\lambda/2$-resonator as well as a $\lambda/4$-resonator are plotted in figure 2.4.

In the measured transmission spectrum, such a resonance evolves as a Lorentzian shaped function (see figure 2.4 right side) of the form

$$L(\nu) = y_0 + A_0 \frac{\nu_\mathrm{B}}{4(\nu - \nu_0)^2 + \nu_\mathrm{B}^2} \,. \tag{2.18}$$

Here, y_0 is the offset, A_0 the amplitude, ν_B the full width at half maximum (FWHM) and ν_0 the resonance frequency. Note that for $\lambda/2$-resonators the parameter A_0 is positive as the resonance increases the measured signal making it a peak. Whereas for $\lambda/4$-resonators, the resonance forms a dip in the measured feedline signal as the resonator absorbs this signal. Thus, the parameter A_0 is negative. This is summarized on the right side of figure 2.4.

From the ratio of the resonance frequency ν_0 and the full width at half maximum ν_B, one can define the quality factor of a resonance [47]

$$Q = \frac{\nu_0}{\nu_\mathrm{B}} \,. \tag{2.19}$$

The quality factor characterizes the ratio of energy stored to energy dissipated in one cycle and hence is a very useful magnitude to classify the quality of a resonance. It describes the

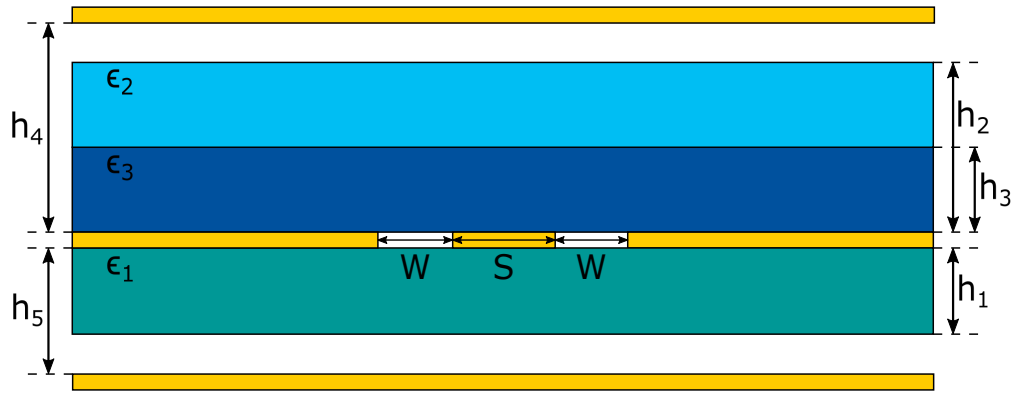

Fig. 2.5.: Schematic cross section of a coplanar waveguide with inner conductor width S, distance to outer conductor W, one substrate below and two substrates above the waveguide sandwiched between two ground planes of respective heights h_i.

ability of a resonator to store electromagnetic energy or the number of photons in it. The coupling parameters described earlier strongly affect the quality factor as better coupling leads to a lower quality factor and vice versa. The quality factor obtained in a measurement is the 'loaded' quality factor consisting of the internal and external quality factor as [47]

$$\frac{1}{Q_\mathrm{L}} = \frac{1}{Q_\mathrm{int}} + \frac{1}{Q_\mathrm{ext}}\,. \tag{2.20}$$

In many systems, the resonator is weakly coupled meaning $Q_\mathrm{int} \ll Q_\mathrm{ext}$ which makes the coupling to the external circuit negligible. This leads to $Q_\mathrm{L} \approx Q_\mathrm{int}$ making the measured quality factor a good measure for the internal quality factor describing the resonant system.

2.3.2. Conformal mapping technique

The cross section of a coplanar waveguide can be seen in figure 2.5. It consists of an inner conductor with width S separated to the outer conductors by gaps of distance W, three layers of dielectrics with corresponding heights h_i $(i = 1, 2, 3)$ and dielectric constants ϵ_i $(h = 1, 2, 3)$ and the distances of the ground planes h_4 and h_5. The geometric dimensions of these quantities determine the effective dielectric constant ϵ_eff and the characteristic impedance Z_0 of the waveguide, which are both of immense importance to operate it. The effective dielectric constant ϵ_eff directly impacts the resonance frequency ν_0 of a resonator (see equation (2.17)) and the characteristic impedance Z_0 ideally has to match the coaxial cable standard of $50\,\Omega$, otherwise signal losses due to reflection will occur. To calculate the effective dielectric constant ϵ_eff and the characteristic impedance Z_0, the theory of conformal mapping [48–50] is used which subdivides the structure into different parts with corresponding capacitances C_i. The following assumptions and calculations are taken out of [48] and expanded by one more dielectric layer on top of the waveguide. Hereby, it is assumed that the conductor is infinitesimally thin and perfectly conducting and the dielectrics are isotropic and lossless. Furthermore, it is assumed that the electric field is only present in the respective regions

with magnetic wall boundaries between all the layers. The total capacitance is calculated by linearly adding the separate capacitances of the layers yielding

$$C_{\mathrm{CPW}} = C_1 + C_2 + C_3 + C_{\mathrm{air}}\,. \tag{2.21}$$

C_i are the capacitances with only the respective layer present and C_{air} is the capacitance in absence of all three dielectric layers.

The respective capacitances are calculated by

$$C_1 = 2\epsilon_0(\epsilon_{r1}-1)\frac{K(k_1)}{K(k_1')} \quad \text{and} \quad C_2 = 2\epsilon_0(\epsilon_{r2}-1)\frac{K(k_2)}{K(k_2')}\,, \tag{2.22}$$

$$C_3 = 2\epsilon_0(\epsilon_{r3}-\epsilon_{r2})\frac{K(k_3)}{K(k_3')} \quad \text{and} \quad C_{\mathrm{air}} = 2\epsilon_0\left(\frac{K(k_4)}{K(k_4')}+\frac{K(k_5)}{K(k_5')}\right) \tag{2.23}$$

with the modulus of the complete elliptic integrals $K(k_i)$ and $K(k_i')$ for the dielectric capacitances

$$k_i = \frac{\sinh\left(\frac{\pi S}{4h_i}\right)}{\sinh\left(\frac{\pi(S+2W)}{4h_i}\right)} \quad \text{and} \quad k_i' = \sqrt{1-k_i^2} \tag{2.24}$$

and for the air capacitance

$$k_i = \frac{\tanh\left(\frac{\pi S}{4h_i}\right)}{\tanh\left(\frac{\pi(S+2W)}{4h_i}\right)} \quad \text{and} \quad k_i' = \sqrt{1-k_i^2}\,. \tag{2.25}$$

The effective dielectric constant ϵ_{eff} can then be calculated by the ratio of the capacitance of the coplanar waveguide and the capacitance in absence of all the dielectric layers

$$\epsilon_{\mathrm{eff}} = \frac{C_{\mathrm{CPW}}}{C_{\mathrm{air}}}\,. \tag{2.26}$$

Plugging in the capacitances from equation (2.22) and equation (2.23) in equation (2.21) and then in equation (2.26) yields

$$\epsilon_{\mathrm{eff}} = 1 + q_1(\epsilon_{r1}-1) + q_2(\epsilon_{r2}-1) + q_3(\epsilon_{r3}-\epsilon_{r2}) \tag{2.27}$$

with the partial filling factors

$$q_i = \frac{K(k_i)}{K(k_i')}\left(\frac{K(k_4)}{K(k_4')}+\frac{K(k_5)}{K(k_5')}\right)^{-1}\,. \tag{2.28}$$

The characteristic impedance Z_0 is defined as

$$Z_0 = \frac{1}{C_{\mathrm{CPW}} v_{\mathrm{ph}}} \tag{2.29}$$

with the phase velocity $v_{\mathrm{ph}} = c/\sqrt{\epsilon_{\mathrm{eff}}}$. With equation (2.23), (2.26) and (2.29), it follows

$$Z_0 = \frac{1}{cC_{\mathrm{air}}\sqrt{\epsilon_{\mathrm{eff}}}} = \frac{60\pi}{\sqrt{\epsilon_{\mathrm{eff}}}}\left(\frac{K(k_4)}{K(k_4')}+\frac{K(k_5)}{K(k_5')}\right)^{-1}\,. \tag{2.30}$$

3. Approaching the $LaAlO_3/SrTiO_3$ interface with microwaves

3.1. Introduction to $SrTiO_3$

STO is a perovskite oxide band insulator with a lattice parameter of 3.905 Å at room temperature [51]. It has an indirect band gap of 3.25 eV and a direct band gap of 3.75 eV placing it at the boundary to semiconductors [52]. The upper valence band mainly consists of states from the O $2p$ electronic orbital with a bandwidth of 5 eV. The conduction band mainly consists of states from the Ti $3d$ t_{2g} and e_g orbitals and at higher energy states from the Sr $4d$ t_{2g} and e_g orbitals. This allows interband transitions from the upper valence band to the conduction band ranging from the indirect band gap of 3.25 eV to 15 eV which corresponds to excitations in free electron like states at higher energies [52, 53].

The crystal structure of STO consists, as the chemical formula $SrTiO_3$ reveals, of Sr^{2+}, Ti^{4+} and O^{2-} ions. Figure 3.1 shows the crystal structure of STO at room temperature. The eight Sr^{2+} ions form a cubic unit cell with one atom in each corner and the Ti^{4+} ion is located at the center of that cube. The Ti^{4+} ion is surrounded by six O^{2-} ions at the face center of the cube forming an octahedron [54]. The bonds within the TiO_6 octahedron are reported to be covalent [55] whereas the bonds between the Sr^{2+} and O^{2-} ions are ionic [56]. Thus, the overall bonding character of STO is a mixture of ionic and covalent.

The crystal structure of a solid is mainly responsible for the dielectric response in an external electric field. This response is well described by the dielectric function $\hat{\epsilon}$ as defined in equation (2.7) with ϵ_1 describing the lossless dispersion and ϵ_2 the absorption losses. Upon cooling from room temperature to very low temperatures, the crystal structure of STO changes several times. Hence, the dielectric properties of STO are strongly temperature dependent and anisotropic leading to differences in the dielectric constant ϵ_1 for different crystal orientations in the range up to a factor of around 2 [57]. At around 105 K, a structural phase transition of second order occurs changing the cubic crystal structure to a tetragonal one. This is due to opposite rotation of the oxygen octahedra leading to a change of the electronic band properties and a rise in the dielectric constant ϵ_1 [58]. Another phase transition to a orthorhombic structure occurs at around 65 K [51, 54]. There is possibly a rhombohedral one at around 10 K which is suggested by some authors but not experimentally proven [59].

Figure 3.2 shows the dielectric constant ϵ_1, the dielectric losses ϵ_2 and the loss tangent $\tan\delta$ of bulk single crystal STO from room temperature to low temperatures. The dielectric constant ϵ_1 follows the Curie-Weiss law $\epsilon = a_0/(T - T_C)$ according to equation (2.9) for temperatures from room temperature to around 65 K yielding a Curie temperature T_C in the range of 30 to 40 K depending on the study [20–22, 54]. At around 105 K, the dielectric

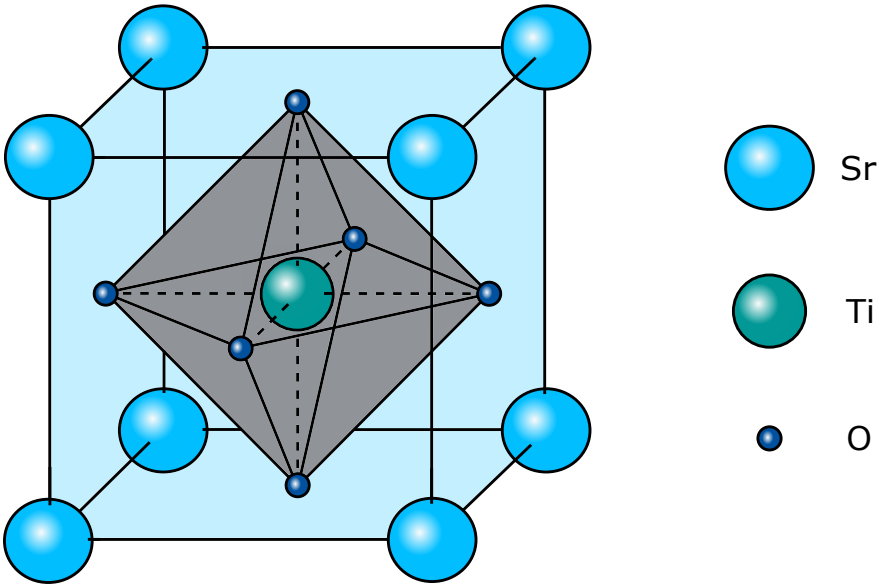

Fig. 3.1.: Cubic perovskite crystal structure of STO at room temperature.

constant ϵ_1 heavily rises due to the phase transition from the cubic to the tetragonal crystal structure. The antiferrodistortion instabilities caused by the opposite rotations of the oxygen octahedra dominate over ferroelectricity distortions due to lattice displacement of the whole cell in respect to the oxygen atoms [51, 58]. Further increase of the dielectric constant ϵ_1 when approaching low temperatures is due to quantum fluctuations of an evolving ferroelectric phase. This increase can be described by the 'soft mode' model [54, 60]. The frequency of a temperature dependent low-frequency transverse optic phonon mode decreases ('softens') with decreasing temperature leading to a rise of the dielectric constant ϵ_1. This is confirmed by the Lyddane-Sachs-Teller relation [54]

$$\frac{\omega_{\mathrm{L}}^2}{\omega_{\mathrm{T}}^2} = \frac{\epsilon_0}{\epsilon_\infty} \tag{3.1}$$

with ω_{T} and ω_{L} referring to the frequency of the long-wavelength transverse optic phonon and the longitudinal optic phonon, respectively and ϵ_0 and ϵ_∞ referring to the dielectric constant at lower and higher frequencies with respect to ω_{T}. It is reported that only the transverse optic phonon mode with the lowest frequency out of four is strongly temperature dependent, the so called 'soft mode' [54, 60]. As the frequency of this mode approaches zero for decreasing temperatures following an ω_{T}^2 behavior, the dielectric constant ϵ_1 of STO follows an increase characteristic for a ferroelectric lattice-caused phase transition [60].

At around 4 K, another anomaly occurs: Instead of continuously increasing with T approaching absolute zero, the dielectric constant of STO levels off at a value in the range of 10^4 and stays constant to the lowest temperature. This is due to the quantum ferroelectric fluctuations which occur below 4 K in the paraelectric phase. STO therefore stays a paraelectric for all finite temperatures and is called an intrinsic quantum paraelectric [20, 21].

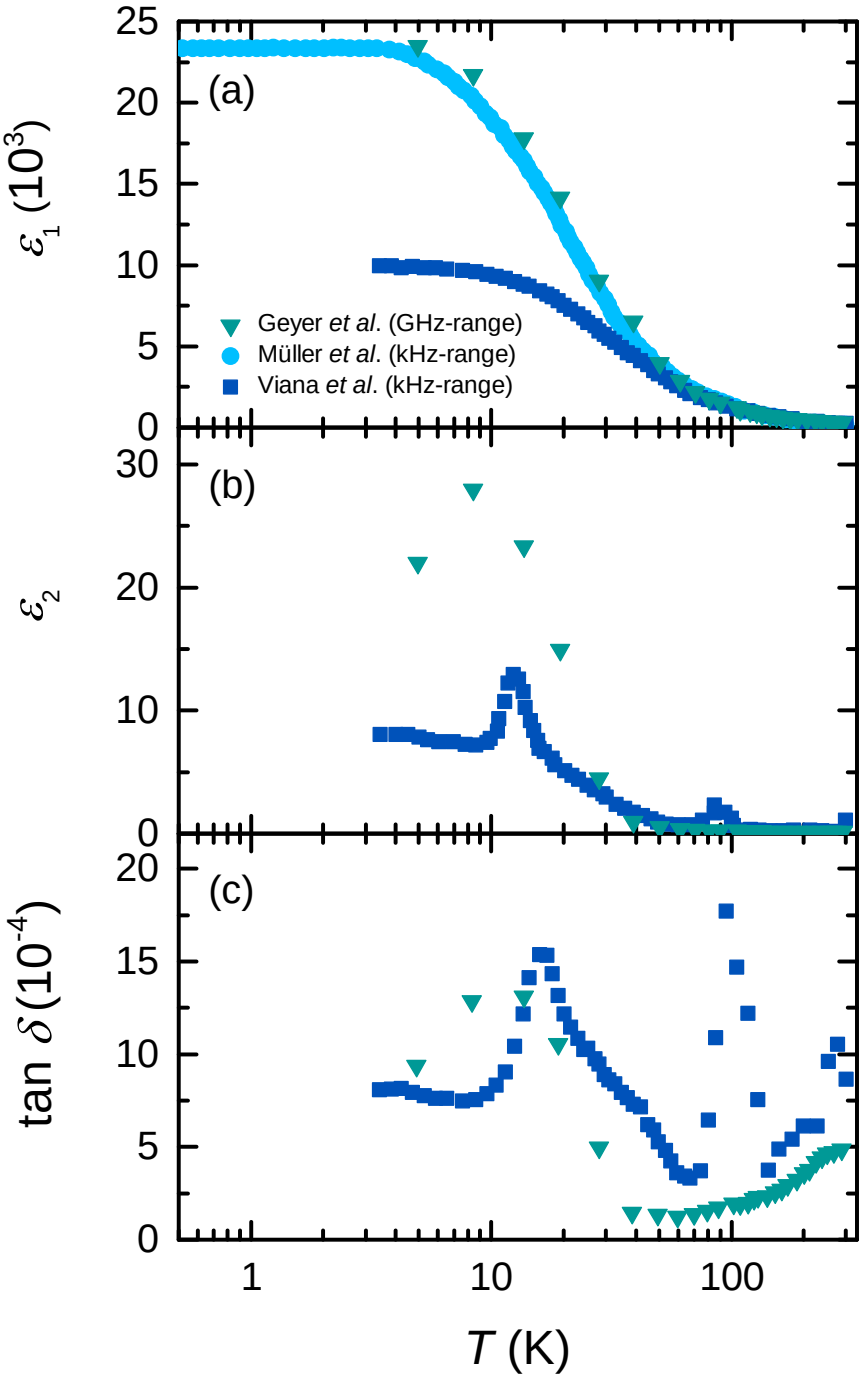

Fig. 3.2.: Temperature dependence of (a) the dielectric constant ϵ_1 (b) the dielectric losses ϵ_2 and (c) the loss tangent $\tan\delta$ of bulk single crystal STO. The light blue data points are taken from Müller *et al.* [20], the dark blue ones from Viana *et al.* [21] and the green ones from Geyer *et al.* [22].

The ferroelectric phase however can be stabilized by applying an external electric field [54, 61], exchanging the oxygen isotope [62], chemical substitutions [63] or applying a large strain to the STO crystal [64, 65].

The dielectric losses ϵ_2 of STO are in the range of values from 0 to around 30 (see figure 3.2(b)) which is relatively higher compared to commonly used microwave resonator substrates e.g. Al_2O_3 [23, 24]. The graph shows two characteristic loss peaks (see figure 3.2(c)): The first one is at around 105 K and originates from the structural phase shift from cubic to tetragonal crystal structure mentioned earlier. The second one at around 15 K denotes to the quantum fluctuations of the ferroelectric phase transition. The loss tangent $\tan\delta$ is in the order of 10^{-4} to 10^{-3} and follows the behavior of the dielectric losses ϵ_2 scaled down by the temperature dependent dielectric constant ϵ_1 as it is defined as $\tan\delta = \epsilon_2/\epsilon_1$.

3.2. Microwave spectroscopy on the $LaAlO_3/SrTiO_3$ interface

3.2.1. Suitability of microwaves

The fascinating and not fully understood properties in the LAO/STO interface give rise to an intensive and highly up-to-date research area. Especially the origin of the superconducting ground state and the electric field tuning with a dome-shaped behavior remain unclear. Superconductivity in general is an intensively researched area in solid state physics, mainly to gain knowledge about both the fundamental processes, but also to find useful and new applications. The significant quantity when probing a superconductor is the gap energy Δ. Within the context of the BCS-theory, the energy gap is directly linked to the critical temperature T_c by equation (2.16) being $\Delta_0/(k_B T_c) \approx 1.76$. This places the energy gap of typical superconductors with T_c in the range of a few K well within the microwave regime [66]. The LAO/STO interface in particular has a critical temperature of $T_c \approx 300\,\mathrm{mK}$, placing its energy gap at a frequency of about $\nu \approx 20\,\mathrm{GHz}$. This is in the typical frequency range accessed with planar microwave resonators and therefore gives rise to probe the LAO/STO using them. However, the highest frequency of published resonators probing the LAO/STO interface does not exceed values of $\nu \approx 400\,\mathrm{MHz}$ so far [7, 28]. Thus, increasing this range to higher values is of enormous interest.

Superconductivity in the LAO/STO interface with no external voltage applied is reported to be in good agreement with the BCS-theory [6, 7]. When applying an external electric field however, the situation complicates. The critical temperature as well as the superfluid density are tunable upon applying an external electric field [8]. Figure 3.3(a) and (b) show the sheet resistance R_{sheet} of the LAO/STO interface in dependence of the temperature for gate voltages in the range of $-300\,\mathrm{V}$ to $320\,\mathrm{V}$ on (a) a semi-logarithmic resistance scale and (b) a linear resistance scale. In the normal state, the resistance can be tuned by two orders of magnitude in dependence of the external field. In dependence of the temperature, the normal state resistance decreases with higher T indicating an insulating ground state [8].

In the superconducting state, starting with high negative gate voltages (small charge carrier density), a rising gate voltage firstly increases the critical temperature from $T_c = 0\,\mathrm{mK}$ to

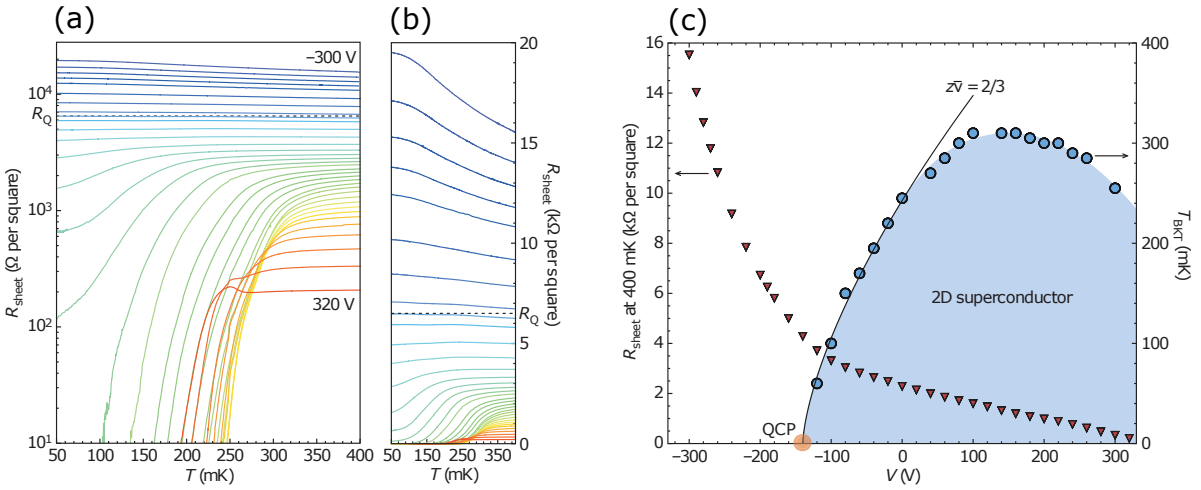

Fig. 3.3.: Effects of the electrostatic gating on the supeconducting properties of the LAO/STO interface. (a) Sheet resistance R_{sheet} in dependence of the temperature on a semi-logarithmic scale for gate voltages in the range of −300 V to 320 V. (b) Same data as in (a) but with linear sheet resistance scale. (c) Superconducting phase diagram (critical temperature T_{BKT}, right axis) and the normal state sheet resistance at $T = 400\,\mathrm{mK}$ (left axis) in dependence of the applied gate voltage. Taken from [8].

a maximum of $T_c \approx 310\,\mathrm{mK}$ and then decreases it down to $T_c \approx 260\,\mathrm{mK}$ in the overdoped regime at a gate voltage of $V = 320\,\mathrm{V}$. Thus, it is possible to drive a superconductor to insulator transition in the LAO/STO interface by electrostatic tuning. The normal state sheet resistance is strongly dependent on the charge carrier density as revealed in figure 3.3(c). The sheet resistance at a constant temperature of $T = 400\,\mathrm{mK}$ is dependent on the gate voltage with a linear behavior and a remarkable change in slope at the quantum critical point (QCP) [8].

Figure 3.3(c) depicts the dome-shaped behavior of the critical temperature on the gate voltage. Reducing the charge carrier density with decreasing gate voltage firstly increases the critical temperature to around 310 mK at $V = 150\,\mathrm{V}$ and then decreases it down to a value of $T_c = 0$ at the quantum critical point marking the superconductor to insulator transition [8, 9]. These measurements reveal the need of mK-temperature experiments to probe the superconducting properties of the LAO/STO interface in dependence of the temperature and electrostatic gating. Measurements in the microwave regime are of great interest to directly measure the superconducting gap energy, which was only revealed by tunneling experiments so far and is assumed to show a similar pseudogap behavior as found in high temperature superconductors (HTSCs) [6].

The peculiar behavior of a superconducting dome is not only observed in the LAO/STO interface. It is found in systems where the critical temperature T_c depends on a tuning parameter such as doping, external field or pressure. Examples of such systems are Nb-doped STO tuned by doping [67, 68], granular Al tuned by dc-resistivity through grain coupling [69, 70], heavy fermion compounds tuned by pressure [71] and HTSCs tuned by pressure or doping [72]. For all of these systems, the question of the mechanism which upon increasing

the tuning parameter firstly leads to an increase, a saturation and then to a decrease in the critical temperature T_c is under heavy debate. In many of these systems, the superconducting dome is terminated by a quantum critical point at $T_c = 0$. The superconductivity is either suppressed by the breaking of Cooper-pairs or by the loss of macroscopic phase coherence, where a competition of both is reported to be the reason in the LAO/STO interface [28]. One main difference of the LAO/STO interface to most other systems is, that no magnetically ordered phase is present near the superconducting dome which eventually vanishes with increasing tuning parameter revealing the dome [73].

In addition to the fundamental understanding of the superconducting phase diagram in dependence of doping and the mechanisms behind that, microwave measurements on the LAO/STO interface are also of great interest when it comes to applications. The field-tunability of the superconducting state in the LAO/STO interface gives a high potential for new quantum electronic devices. Such applications are e.g. superconducting quantum interference devices (SQUIDs) realized in the LAO/STO interface [74] or superconducting qubits which operate in the microwave regime [29]. This also drives forward the need of increasing the highest accessible frequency of LAO/STO devices.

3.2.2. Experimental state of art

Another reason for still unsolved questions concerning the LAO/STO interface is the extremely challenging experimental access to it. Usual magnetotransport measurements fail to directly measure the superfluid density of the 2DEG. Nevertheless, using a scanning SQUID method, it was possible to measure the magnetization and susceptibility in the LAO/STO interface and then excerpt the penetration depth and superfluid density [11].

As coplanar microwave resonators offer a direct access to the superconducting properties of its conductor, this can be expanded to a resonator consisting of a thin film of LAO deposited on bulk STO letting the 2DEG of the interface in between form the actual resonator. One then can directly probe the temperature dependent superconducting properties like the superconducting density and the critical temperature of the 2DEG by monitoring the resonance frequencies of the resonator in dependence of the temperature. It is also suitable for the application of a gate voltage to reveal the dome-shaped behavior of said quantities. Though, the strongly tem-

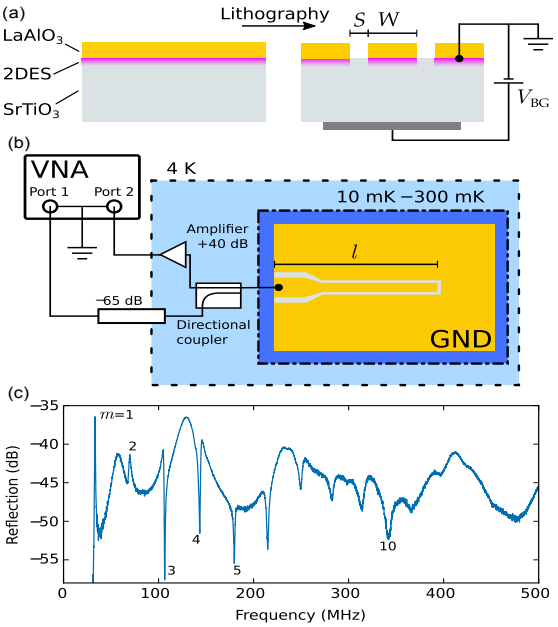

Fig. 3.4.: Coplanar LAO/STO resonator studied in reflection geomerty by Manca *et al.* (a) Schematic cross section of the resonator. (b) Experimental setup. (c) Reflection spectrum of the cpw up to 500 MHz. Taken from [7].

perature dependent dielectric properties of STO with the extremely high dielectric constant ϵ_1 and the comparably high dielectric losses ϵ_2 make the realization of a coplanar microwave resonator with a substrate of STO an immense challenge.

However, very recently, Manca *et al.* presented a coplanar resonator in the LAO/STO interface to explore its superconducting phase diagram in dependence of not only the temperature but also the electrostatic gating. Figure 3.4(a) shows a schematic cross sectional sketch of their resonator model before (left) and after (right) the lithographic process. The experimental setup can be seen in figure 3.4(b). They deposited a 12 unit cell thin film of LAO on a bulk TiO_2-terminated STO substrate (100). The resonator structure in the LAO layer was formed using electron beam lithography and ecthing by Ar-milling to remove the LAO parts. It has an inner conductor width of $S = 40\,\mu m$, gaps to the outer conductor of $W = 10\,\mu m$ and a length of $l = 2.5\,mm$ (note that the authors use S and W the other way round in figure 3.4(a) than it is used in this work). Thus, the actual resonator is formed by the 2DEG between the LAO and the STO layer. The resonator length defines the fundamental mode at a frequency of around $\nu_0 = 30\,MHz$, close to the lower boundary of the microwave spectrum. One end of the resonator is isolated from the ground and partially reflects the electromagnetic signal, hence realizing a nearly $\lambda/2$-resonator. The other end is connected to a vector network analyzer (VNA) to couple the electromagnetic signal into the resonator. A directional coupler separates incoming and outcoming signal from port 1 to port 2 of the VNA making it possible to measure the reflection signal with the S_{21}-parameter and to insert an attenuator and an additional amplifier in two separate cryogenic transmission lines for the incoming and reflected signals, respectively. An applied gate voltage between a backgate and the interface (see figure 3.4(a)) allows to measure the reflection signal in dependence of an external electric field. Figure 3.4(c) shows the reflection spectrum for $11\,mK$, $V_{BG} = 0\,V$, $P = -95\,dBm$ and in the frequency range of $30 - 500\,MHz$. It shows that the resonance frequencies are visible up to the 10th mode at a frequency of around $300\,MHz$. The disappearing mode amplitude primarily is due to damping because of coupling, quasiparticles and losses in the STO substrate. With this setup, the frequency shift of the modes can be monitored in dependence of the temperature and the external gate voltage and subsequently, the superfluid density and the critical temperature can be extracted.

The main findings of the authors is the superconducting phase diagram of the LAO/STO interface in dependence of the temperature and the electrostatic gating. The temperature dependence for $V_{BG} = 0\,V$ is in agreement with a clean s-wave BCS-superconductor. The superfluid density as well as the critical temperature follow a dome-shaped behavior in dependence of the gating but are not monotonically related. This is due to the ground state which the authors interpret as a Josephson junction array shifting from short range order in the underdoped region to long range order in the overdoped region. The overdoped region therefore is consistent with BCS-behavior.

A different approach to realize a resonant device to probe the LAO/STO interface in the microwave regime was presented by Singh *et al.* [28]. They enabled experimental access to the superfluid density of the 2DEG by a dynamic transport measurement using an equivalent circuit model. It measures the change of the resonance frequency of an RLC circuit evoked by an inserted LAO/STO element.

The authors epitaxially deposited an 8 unit cell thin film of LAO on a 200 µm thick TiO_2-terminated substrate of single crystal (001) STO by pulsed laser deposition. On the backside of the STO substrate they applied a weakly conducting backgate for the gating process. This LAO/STO element was then inserted in a cpw transmission line connecting the inner conductor with the outer conductor. This can be seen in figure 3.5(a) depicting the schematic experimental setup of the resonator. Parallel to the LAO/STO element, there is a RLC circuit with an inductor L_1 and a resistor R_1 which are surface mounted microwave devices (SMDs) (see figure 3.5(c)). The capacitor is provided by the to the 2DEG (Z_{2D}) parallel connected STO substrate and thus called C_{STO}. Because of the very high dielectric constant of STO at mK-temperatures, the RLC circuit gets dominated by C_{STO}. C_P are protective capacitors that prevent ac current flowing through the inductor and resistor disturbing the measurement. The cpw transmission line is connected to port 1 of a VNA from which the microwave signal is coupled into it, terminating it with Z_0 of the transmission line (see figure 3.5(b)). A directional coupler splits the incoming and outcoming signal guiding the outcoming signal to port 2 of the VNA, hence the reflected signal of interest from the LAO/STO element is measured by monitoring S_{21} with the VNA. It also makes it possible to use several attenuators and a bias-tee for the incoming signal and a high electron mobility transistor amplifier (HEMT amp.) for the reflected signal. The S_{21}-parameter is directly connected to the reflection coefficient [28]

$$\Gamma(\omega) = \frac{A^{\text{out}}(\omega)}{A^{\text{in}}(\omega)} = \frac{Z_L(\omega) - Z_0}{Z_L(\omega) + Z_0} \tag{3.2}$$

where A^{out} and A^{in} represent the complex wave amplitude of the reflected and incoming signal, respectively, Z_L the load impedance of the RLC circuit and Z_0 the characteristic impedance of the cpw transmission line. The load impedance Z_L of the RLC circuit thus directly links to the 2DEG. The resonance frequency ω_0 of the RLC circuit gets affected by the kinetic inductance of the 2DEG in the superconducting state. Monitoring ω_0 in dependence of the temperature and the external gate voltage therefore gives direct experimental access to the superconducting phase properties of the 2DEG.

The main results in this paper are the measurements of the superfluid stiffness (cost of a phase twist of the Cooper-pairs) in the LAO/STO interface in dependence of the temperature and the electrostatic doping. The authors report that for the overdoped region, agreement for the superfluid stiffness and the gap energy with the BCS-theory is given. This is also in close agreement with the findings of Manca *et al.* For the underdoped region, the quantum critical point is reached because of the loss of macroscopic phase coherence of the Cooper-pairs rather than breaking of them. The portion of charge carriers in the superconducting state is reported to be only a fraction of the total electrons. The reasons for the superconductivity in dependence of the gating is proposed to be due to the weak filling of the d_{xz}/d_{yz} bands.

Note, that the same group of Singh *et al.* also investigated the differently crystallographic oriented (110)-LAO/STO interface with the same experimental setup. They discovered a electrostatic-tunable transition from single band to two band superconductivity with a decreasing critical temperature while the second band is populated [75].

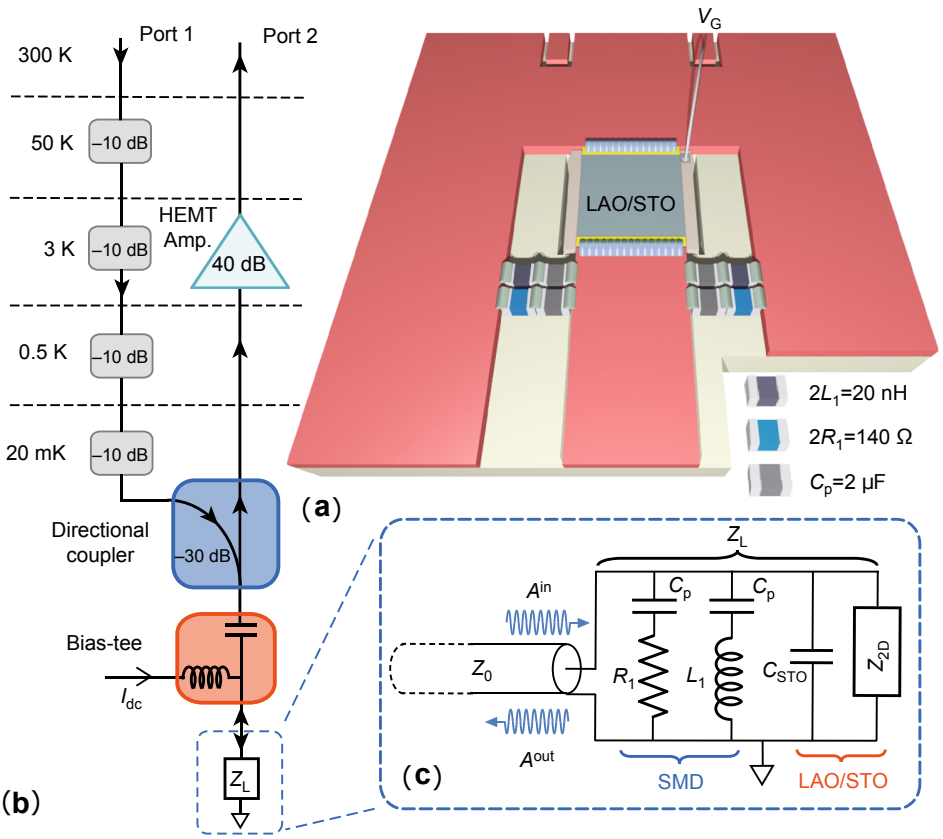

Fig. 3.5.: (a) Schematic setup of the coplanar resonator realizing the RLC circuit with the LAO/STO element. (b) Scheme of the experimental setup between the VNA and the coplanar resonator. (c) Schematic circuit of the load impedance Z_L (RLC circuit) with the SMDs and the LAO/STO element. Taken from [28].

4. Development of possible resonator models

In this chapter, three different superconducting coplanar resonator models which can directly be transferred to the LAO/STO interface are presented. Firstly, the general and explicit requirements to the resonator models for that purpose are stated before introducing and evaluating the models separately stating their advantages and disadvantages.

4.1. Requirements

The resonator model of interest is a superconducting coplanar resonator on the substrate STO. The coplanar geometry is the favored one because this geometry allows the direct transfer of the resonator geometry to an LAO/STO resonator. By replacing the conducting layer of the resonator with a thin film of LAO, the 2DEG gets formed between LAO and STO in the shape of the resonator structure. The stripline geometry is not suitable for this procedure as the inner conductor is sandwiched between two dielectrics heavily complicating the realization and gating of the interface.

The conductor of the superconducting resonator should be a mechanically robust conventional BCS-superconductor with critical temperature T_c of at least several K e.g. Nb. The response of STO can therewith be probed at convenient cryogenic temperatures and with the conductor in the superconducting state. The LAO/STO resonator would operate in its superconducting state at mK-temperatures.

When designing the resonators on STO, one should consider the high and heavily temperature dependent dielectric constant ϵ_1 and the high dielectric losses ϵ_2 of STO. These properties have been addressed in section 3.1 of this thesis. The high dielectric constant ϵ_1 at low temperatures leads to an enormous impedance mismatch to the coaxial cable standard of $Z_S = 50\,\Omega$. The geometric parameters of the inner conductor S and the gap to the outer conductor W cannot compensate for the high effective dielectric constant ϵ_{eff}. The extend of the impedance mismatch gets clear by taking equation (2.30) into consideration, $Z_0 = (cC_{\text{air}}\sqrt{\epsilon_{\text{eff}}})^{-1}$ which leads to a very large reflection coefficient $r = (Z_0 - Z_S)/(Z_0 + Z_S)$ and thus a very small signal coupling into the resonator assuming a coplanar $\lambda/2$-resonator. Hence, the amplitude and therefore the visibility of the resonant modes would be very low and decaying for higher mode numbers n. This problem is also strongly intensified by the high dielectric losses in the STO substrate.

The high dielectric constant also shifts the resonance frequency ν_0 (see equation (2.17)) to very low frequency values. A variation of the resonator length l has to define the resonance frequency in the microwave regime. But as the resonator length has a minimal length,

this is also quite a challenge when designing possible resonator models. The resonance frequency ν_0 of the fundamental mode ideally lies in the lower range of the microwave regime to cover a frequency range as broad as possible and to match the energy scale of the superconducting 2DEG in the LAO/STO interface which is expected to have its energy gap Δ at a corresponding frequency of $\nu \approx 20\,\mathrm{GHz}$.

Another requirement that the resonator model should meet is the possibility to apply an external gate voltage onto the LAO/STO interface to reveal the dome-shaped behavior of the superconducting properties in dependence of the electrostatic doping. The order of this gate voltage is in the range of up to around 50 V. There are two possible difficulties arising from this applied gate voltage:

One is that the dielectric constant ϵ_1 is field dependent [54, 61] and therefore could interfere with the measurements on the 2DEG which are being monitored by the resonance frequency shift. By assuming a 500 µm thick substrate of STO which is also the distance of the backgate to the resonator conductors or the 2DEG and an applied gate voltage of 50 V, the electric field and thus the impact on the change in the dielectric constant can be estimated. This leads to an electric field of 1000 V/cm which does not impact the dielectric constant to a degree that would impact the measurement of the 2DEG [54, 61]. This is also approved in [7]. In the work of Singh *et al.* [28], the impact of the electric field on the dielectric constant of STO was observed, but the superconducting effects of the 2DEG were evaluated by sweeping the temperature at constant external electric fields making the effect also negligible. An option to account for undesired resonance frequency shifts induced by the electric field is a reference measurement with a resonator out of a known superconductor e.g. Nb on STO applying the same gate voltages as with the LAO/STO resonator.

The other difficulty is that the gate voltage should not impair or prevent resonator operation at any applied voltages which therefore sets an upper boundary for the absolute value of the voltage. The maximal electric field a material can persevere is given by the material specific dielectric strength. Electrical breakdown in the STO substrate can immediately be ruled out because the mentioned applied fields are well below the dielectric strength of STO, which is in the order of 100 kV/cm and more [76]. The other area through which the gate voltage could break onto other parts is high vacuum surrounding the resonator chip in a dilution refrigerator where the LAO/STO resonator would be measured. The dielectric strength of high vacuum is in the range of $200 - 400\,\mathrm{kV/cm}$ [77, 78]. The typical geometrical distances for microwave resonators are in the range of 10 µm and more. The dielectric strength of vacuum being $20 - 40\,\mathrm{V/\mu m}$ should therefore lead to no complications considering the order of the applied voltage.

The material of the backgate for applying the gate voltage could either be a weakly conducting metal with a high resistance or a superconductor to not influence the measurement of the 2DEG or the resonator operation.

Finally, the fabrication possibilities of the resonator model have to be considered in the means of substrates as well as conductors. Fabricating and mounting different substrates in-plane and next to each other with µm-precision is very challenging, so placing them on top of each other is more favorable. The usual thickness of a resonator substrate ranges from $200 - 500\,\mu\mathrm{m}$. The conductors typically have a thickness of $500 - 900\,\mathrm{nm}$ for a metal and 300 nm for a conventional superconductor.

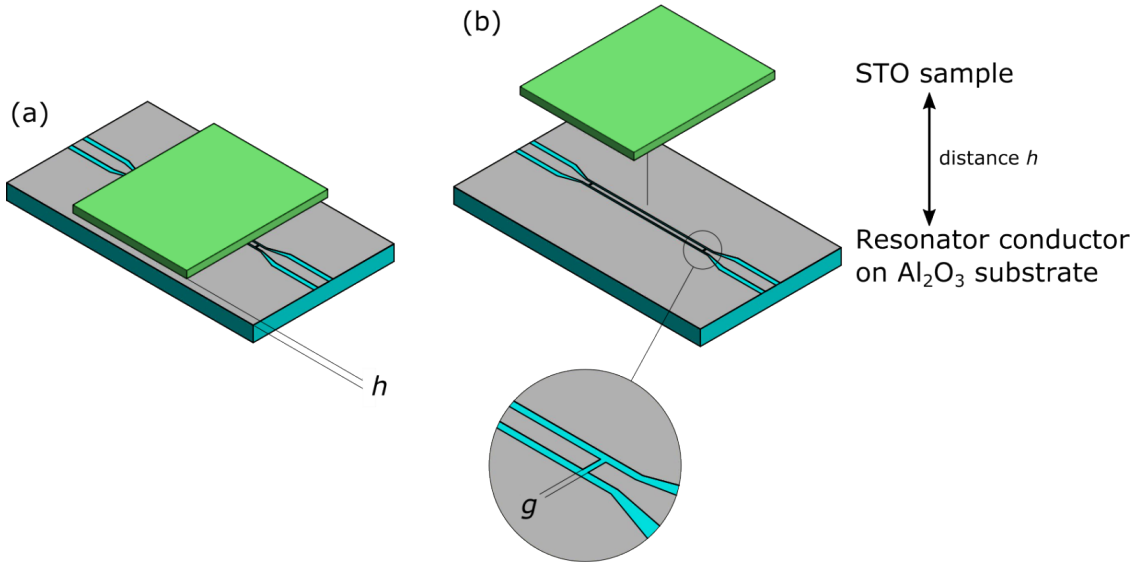

Fig. 4.1.: (a) Schematic sketch of the mounted coplanar resonator model on an Al_2O_3 substrate (light blue) where an STO sample (green) is externally placed at a distance h over the conductor. (b) Expanded sketch of the resonator model. The inset shows the coupling parameter g which defines the size of the capacitive coupling gap.

With these requirements in mind, three different concepts for the resonator layout are being considered in detail.

4.2. Conventional coplanar half-wavelength resonator

The first presented resonator model is a conventional coplanar superconducting $\lambda/2$-resonator on an Al_2O_3 substrate with an external STO sample as a perturbation at a given distance h over the resonator chip. Figure 4.1 shows a schematic sketch of this resonator. This conventional coplanar resonator geometry was used intensively over the last years not only at the 1. Physikalisches Institut but also by research groups world wide. Therefore, a vast knowledge about the geometry and the behavior in a cryogenic environment is already available. The fabrication of the resonator chips is rather easy and fast. Placing the STO sample over the resonator chip is challenging, though. To analyze the resonator model quantitatively, it is of great interest to precisely know the distance h of the STO sample to the resonator conductor as it directly impacts the effective dielectric constant and therefore the resonance frequency of the resonator (see equation (2.17)). Therefore a µm-precise mounting and ideal controlling of the STO sample is significant but enormously challenging. Possible solutions are the use of small pillars of an insulating material with a low dielectric constant e.g. Teflon or Al_2O_3.

The coupling into the resonator can be controlled via the only coupling parameter, the gap size g. This creates an impedance mismatch and leads to the partial reflection and transmission of the incoming electromagnetic microwaves. The impedance mismatch created

by the high dielectric constant ϵ_1 of the STO sample though is more impactful. Assuming the coaxial cable standard impedance of $Z_S = 50\,\Omega$ and a characteristic impedance $Z_0 = 1\,\Omega$ of a coplanar resonator with an STO sample of very high dielectric constant ϵ_1, it yields a reflection coefficient of $r \approx 0.96$. Hence, only a fraction of around 4 % of the microwave signal couples into the actual resonator. The resonance modes therefore have a very low amplitude but are still detectable and analyzable as shown in [27]. To avoid undesired impedance mismatches and accompanied reflections, the boundaries of the STO sample are placed exactly in the middle of the coupling gaps.

The transition from a single STO sample to the LAO/STO interface would be done by depositing an ultra thin layer of LAO under the STO substrate. Thus, the LAO/STO interface is probed as an external perturbation to the coplanar resonator operating on the sapphire substrate. The experimental access to the 2DEG is not optimal and not as good as with the approach where the 2DEG itself constitutes the resonator.

The gating could be realized quite straightforward by placing a backgate on top of the STO substrate and then gating directly into the interface. The requirement of the gate voltage not impairing or preventing resonator operation by an electrical breakdown mentioned in section 4.1 puts extra emphasis on the need of precise distance adjustment of the LAO/STO element. The distance of the backgate to the resonator conductor of the coplanar resonator is the decisive measure for a possible electrical breakdown. So increasing either the STO substrate thickness or the distance h has to be addressed. The latter is more convenient and therefore addressed. As mentioned in section 4.1 the dielectric strength of vacuum is about $20 - 40\,\mathrm{V/\mu m}$, so placing the LAO/STO element in a distance of $h \approx 50\,\mu\mathrm{m}$ should be sufficient and seems feasible.

4.3. Capacitively coupled half-wavelength resonator

The second resonator model is a flipped coplanar superconducting $\lambda/2$-resonator capacitively coupled over a feedline on an Al_2O_3 substrate at a distance h. An earlier version of this resonator model, but with the resonator not being flipped by 180°, was presented in the master thesis of M. Beutel in 2016 [26]. To make this model more viable in an experimental setup and to change the coupling process of the microwave signal from the lossy STO substrate to air/vacuum, the resonator is being flipped by 180° before mounted on top of the feedline as shown in figure 4.2. The main advantage of given geometry is that the impedance mismatch generated by the STO substrate directly forms the resonator but does not impact the line impedance and therefore lowers the signal of the feedline to a high degree. The resonator is ideally aligned in such a way that the resonator line exactly lines up with the feedline.

The coupling is controlled by three coupling parameters: The distance h of the resonator conductor to the feedline conductor, the feed length l_f which describes the length of the overlap of the resonator ground planes and the feedline ground planes and the size of the gap g of the resonator. These three coupling parameters allow a controlling of the coupling and therefore the quality factor Q to a certain and considerable degree. One advantage is also that the distance h has little to no impact on the resonance frequency of the resonator like for the model presented in section 4.2 but rather on the coupling.

The fabrication of the resonator structure and the feedline structure can be done separately and is rather fast and easy. However, changing the coupling parameters l_f and g would always need a separate design and fabrication of a whole new resonator chip as well as a feedline chip.

The mounting of the resonator over the feedline is an enormous challenge. The resonator has to be precisely aligned in the following directions: To guarantee correct resonator operation, the alignment of the resonator line and the feedline has to be matched very precisely. Additionally, to control the coupling, the distance h and the feed length l_f have to be met and known to a certain degree. This thus requires very precise alignment and measuring in all three dimensions in space on the µm-scale.

The transition from the superconducting resonator to the LAO/STO resonator can easily be done with this model by replacing the superconducting layer shaped in the resonator form by an LAO layer. As a consequence, the 2DEG would form the actual resonator like it is also done in [7]. The resonance frequency and its temperature and gate dependent shift would then give direct experimental access to the conducting and superconducting properties of the 2DEG.

The gating procedure is rather complicated: The backgate could be placed on top of the STO substrate but then connecting it with the inner and outer conductor of the resonator is a tremendous task as they are separated by the gap of the inner and outer conductor W. It could be done by just gating the outer conductor and then putting the backgate and the inner conductor on the same ground but this is challenging in terms of the fabrication as well as in the experiment. The gate voltage should also not break down through the air/vacuum onto the feedline while resonator operation but as shown in section 4.1, a distance $h \approx 50\,\mu\text{m}$ should be sufficient. Adjusting the distance h therefore is of great interest for this resonator model taking the coupling and the gate voltage into account.

The behavior of this resonator model is nearly completly unknown as only the earlier version of it with the flipped resonator has been studied in simulations so far [26] and has not been realized for an experiment, thus empirical values are completely missing.

4.4. Inductively coupled quarter-wavelength resonator

The third resonator model is a flipped coplanar superconducting $\lambda/4$-resonator coupled over a feedline on an Al_2O_3 substrate at a distance h. The coupling into this resonator is realized inductively and in contrast to earlier work [45] and the procedure shown in the theory part of this thesis (figure 2.3), the resonator is not placed in the same plane as the feedline but rather at a distance h over it. This should not change the basic process of coupling drastically, just replaces the coupling parameter g in the theory of an in-plane resonator with the distance h of the out of plane resonator. The resonator model is pretty similar to the one presented in section 4.3 except the coupling is realized inductively and the resonator is a $\lambda/4$-resonator instead of a $\lambda/2$-resonator. The resonances of this resonator model therefore appear as dips in the transmission signal of the feedline absorbing energy out of it instead of the $\lambda/2$-resonator model which intensifies the measured signal, thus resulting in peaks.

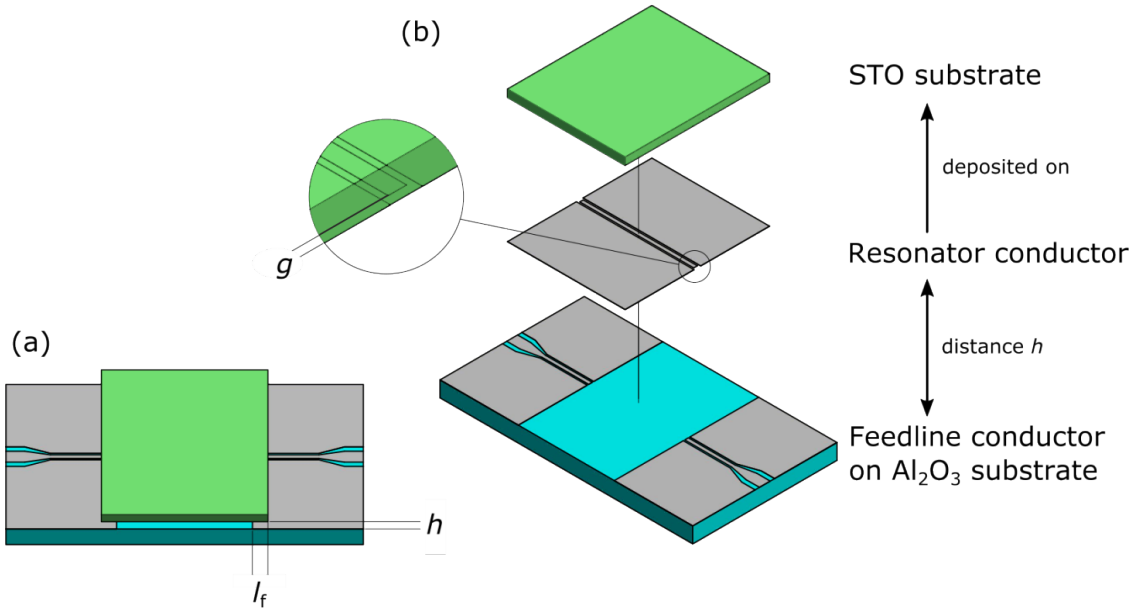

Fig. 4.2.: (a) Schematic sketch of the capacitively coupled flipped $\lambda/2$-resonator on the substrate STO (green) mounted at a distance h over a feedline on an Al_2O_3 substrate (light blue). The coupling parameter feed length l_f is the overlap of the feedline conductor and the resonator conductor. (b) Expanded sketch of the resonator model. The inset shows the coupling parameter g which defines the size of the capacitive coupling gap.

This flip-chip design has the advantages of letting the microwave signal couple into the resonator through air/vacuum instead of the lossy STO substrate. Besides that, it also does not lead to an enormous impedance mismatch in the feedline because the resonator conductor partially shields the high-ϵ_1 STO substrate from the feedline so that the feeding signal is not damped too heavily. Additionally, it also simplifies the experimental setup placing the sample flipped over the feedline.

For this model, the coupling is controlled via two coupling parameters: The distance h describes the space between the resonator conductor and the feedline conductor. This distance does not impact the resonance frequency position of the resonator to a high degree because the dielectric constant $\epsilon_{1,\mathrm{STO}} \gg \epsilon_{1,\mathrm{Al_2O_3}}$, thus dominating the effective dielectric constant. Additionally, the conductor of the resonator and the feedline shield out the influence of the dielectric of the other device. The distance h thus only affects the coupling of the resonator.

The second coupling parameter is the coupling length l_c which is the length of the resonator ideally parallel and centrally placed over the feedline and hence responsible for the coupling. This length still adds to the whole resonator length $l = l_\mathrm{c} + l_\mathrm{r}$ (see figure 2.3).

The fabrication of the chips can also be done separately rather easily and quickly. For this resonator model, only one type of feedline chip is needed in comparison to the model in section 4.3 because no coupling parameter is introduced on the feedline chip. This substantially lowers the fabrication complexity, cost and time.

The mounting of the resonator over the feedline is also challenging but for this model only two directions in space are important because the position of the resonator along the feedline is of no significant importance as long as the coupling length l_c is centrally places over the feedline. This can be simplified by making the inner conductor of the feedline to some degree larger than the inner conductor of the resonator. However, the adjustment and control of the central positioning over the feedline and the distance h is of same importance as for the other model because of the coupling and the gating procedure.

The transition from the superconducting resonator to the LAO/STO resonator follows the same procedure as for the $\lambda/2$-model by replacing the superconducting layer with an LAO layer letting the 2DEG itself form the resonator.

The geometry of this model changes the gating procedure to a certain degree: The fact that this resonator forms a $\lambda/4$-resonator and therefore the inner conductor and the outer conductor share the same potential immensely simplifies gating. Placing a backgate on top of the STO substrate and then gating into the LAO/STO interface should lead to no other difficulties. The challenges concerning the break down of the gate voltage to the feedline and therefore the importance of adjusting the distance h stay the same.

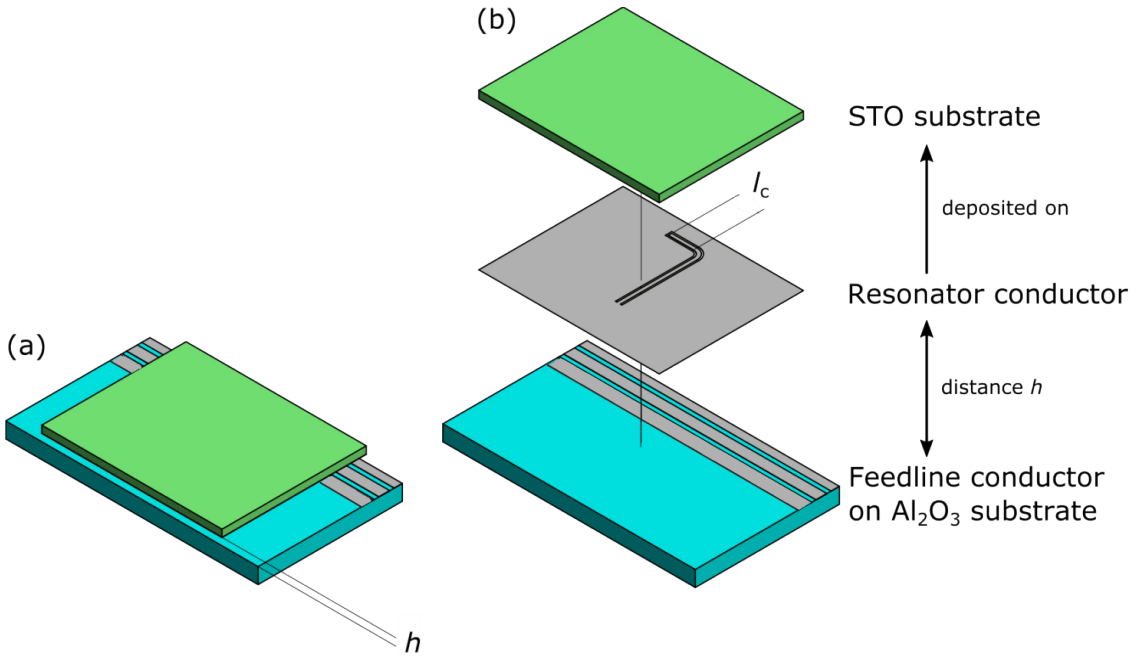

Fig. 4.3.: (a) Schematic sketch of the inductively coupled flipped $\lambda/4$-resonator on the substrate STO (green) mounted at a distance h over a feedline on an Al_2O_3 substrate (light blue). (b) Expanded sketch of the resonator model with the coupling length l_c denoting to the arm of the resonator placed centrally and parallel over the feedline.

5. Simulations

Simulations offer accessibility to complex systems which cannot easily be solved theoretically or experimentally and allow the testing and optimization of a real world system before finalizing it [79]. They are used in this work to analyze and optimize the resonator models presented in chapter 4. Simulations use approaches which numerically and approximately describe a given system making it solvable. This finite element method (FEM) subdivides the complex system into smaller elements simplyfying the problem. The finite elements are then solved individually by describing them with analytic equations. For these equations, certain start values and boundary conditions are chosen which are suitable for the physics of the system and the desired quantities. The individually solved elements on a smaller picture are then put back together to describe the complex complete system of interest [79].

One of these solving approaches often used in commercial simulation programs e.g. *CST Microwave Studio* [80] is the finite integration technique (FIT) [81, 82]. This technique numerically solves electromagnetic field problems by applying the Maxwell equations (see equation (2.1) − (2.4)) in their integral form to a spatial discrete set of mesh cells. These cells can have a large variety of forms e.g. tetrahedral or hexagonal, making it applicable for a lot of different geometries and materials. The cells are then combined and related to each other by the electromagnetic material and Maxwell equations allowing for different material distributions and properties like anisotropy. The accuracy and calculation duration of the simulations thus strongly depend on the form and density of the mesh cells. A denser mesh for areas of large electric and magnetic field gradient should be chosen to achieve an accurate modulation of the reality at a cost of simulation duration.

In this work, the commercially available computer software *CST Microwave Studio* [80] which is a leading tool for the electromagnetic simulation of high frequency (HF) 3D components is used for finite element simulations. The program offers a CAD environment to model any desired 3D object like a coplanar microwave resonator. Certain length or material parameters can be changed on the fly and swept through to allow small changes and quantitative optimizations of the desired resonator model. The frequency domain solver allows to guide an electromagnetic microwave signal with a built-in adaptive frequency sweep through the constructed model by the introduction of waveguide ports. It directly gives access to 3D near-fields as well as the S-parameters of the resonant device. The frequency domain solver best suits small electric devices with a high quality factor Q making it excellently applicable for coplanar microwave resonators. The mesh can be set to cartesian or tetrahedral whereas in this work, the tetrahedral one was chosen because it better describes small and curved structures [83]. The mesh refinement is done manually by allocating the components to different mesh groups of different mesh densities. To reach an even denser mesh, additional mesh dummies are introduced in locations where a large electric field gradient requires a

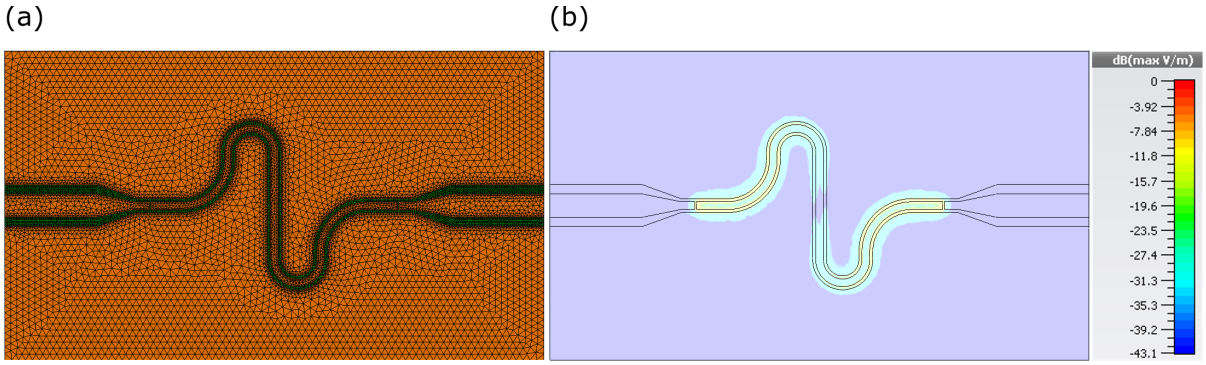

Fig. 5.1.: Simulation of a meander copper resonator structure on an STO substrate (a) Mesh view of the simulated structure. The mesh of the inner conductor and the gap between inner and outer conductor is visibly denser than elsewhere to account for the higher magnetic and electric field density there. (b) Amplitude of the electric field of the first resonant mode with a node in the middle of the resonator.

denser mesh. With this method, a balance between accuracy and time but also resource necessity of the simulation can be found.

At the beginning of this chapter, the consistency of theory, simulation and experiment of a high-ϵ_1 coplanar microwave resonator is presented to show the reliability of the simulation for the ongoing process. Afterwards, the three resonator models of chapter 4 are being investigated in detail.

5.1. Consistency of theory, simulation and experiment

In order to show the reliability of the simulations concerning the coplanar microwave resonators on the high-ϵ_1 dielectric STO, the consistency of theory, simulation and experiment is shown, firstly.

Therefore, a meander shaped coplanar $\lambda/2$-resonator with the conductor material Copper has been constructed in *CST MWS* and fabricated in reality (for the purpose of my bachelor thesis [27]). The length of the resonator was chosen to be $l = 6.17\,\text{mm}$, the coupling gaps $g = 20\,\mu\text{m}$, the inner conductor width $S = 100\,\mu\text{m}$ and the gap to the outer conductor $W = 40\,\mu\text{m}$. The resonator substrate is a single crystal STO substrate (100) with a height of $h = 430\,\mu\text{m}$ and a literature value of the dielectric constant $\epsilon_1 = 300$ at room temperature. Figure 5.1(a) shows the mesh view of the simulated resonator structure. The tetrahedral mesh cells can clearly be seen. The mesh of the inner conductor and the capacitive coupling gaps is visibly denser than at the surrounding areas. This was realized by the manual mesh refinement to account for the higher magnetic and electric field density there. Figure 5.1(b) shows the electric near-field amplitude of the fundamental mode ($n = 1$). The field distribution is exactly how it is expected of the fundamental mode showing a node in the middle of the resonator length and increasing electric field amplitude with the maxima close to the capacitively coupling gaps. This can be compared to the field distribution shown in figure 2.4 in the theory section 2.3.1 and is in agreement with it.

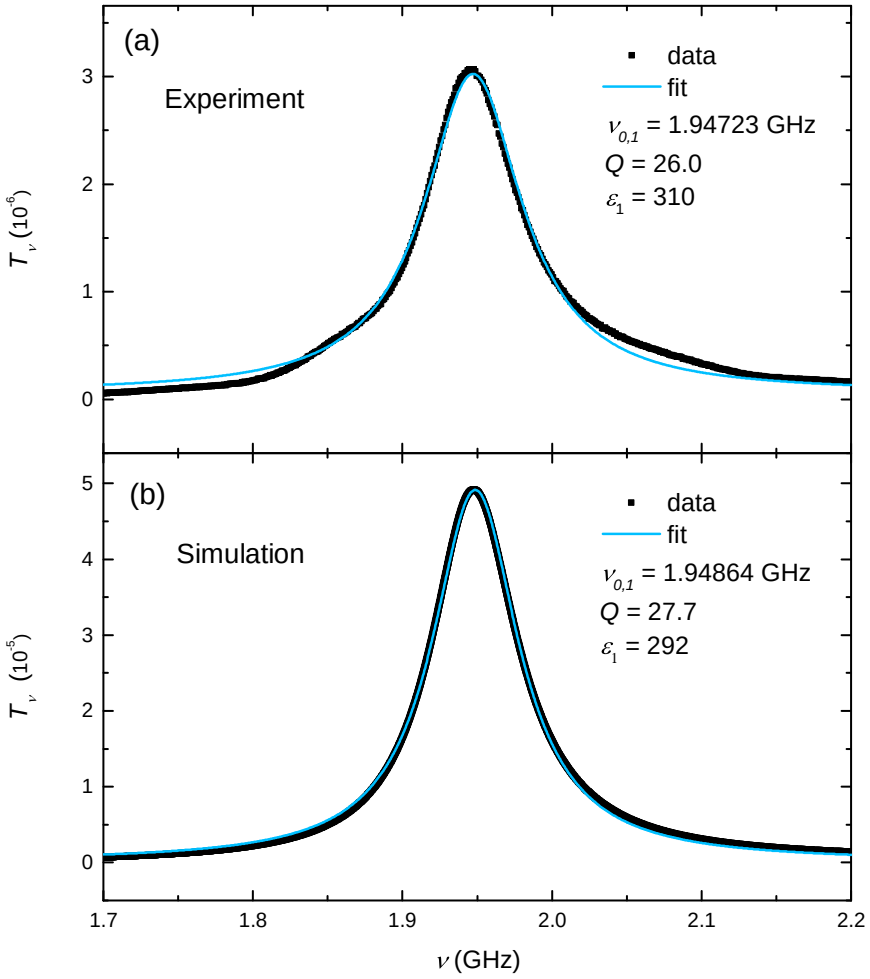

Fig. 5.2.: (a) Measured transmission spectrum ($T_\nu = S_{21}^2$) of the coplanar Cu $\lambda/2$-resonator from $1.7 - 2.2\,\mathrm{GHz}$. (b) Simulated transmission spectrum ($T_\nu = S_{21}^2$) of the coplanar Cu $\lambda/2$-resonator from $1.7 - 2.2\,\mathrm{GHz}$ with a dielectric constant $\epsilon_1 = 292$ and a loss tangent $\tan\delta = 10^{-3}$.

The resonance peak is now analyzed quantitatively: The resonator chip was designed to have its resonance frequency at a theoretic value of $\nu_{0,1} = 1.996\,72\,\mathrm{GHz}$ calculated with the conformal mapping theory presented in section 2.3.2 of this work. Figure 5.2 shows (a) the measured and (b) the simulated transmission spectrum ($T_\nu = S_{21}^2$) of the Cu-resonator from $1.7 - 2.2\,\mathrm{GHz}$ depicting the fundamental mode. Both resonances are precisely described by a Lorentzian line shape. The position of the resonance in the measured spectrum is $\nu_{0,1,\mathrm{meas}} = 1.947\,23\,\mathrm{GHz}$ deviating only around 2 % from theory. The simulation was performed by sweeping the dielectric constant ϵ_1 of the STO substrate in the range of the expected value of 300, while assuming a constant loss tangent of $\tan\delta = 10^{-3}$ to account for the losses in STO (see figure 3.2). The best agreement to the measured value was found for a value of $\epsilon_{1,\mathrm{STO}} = 292$ yielding $\nu_{0,1,\mathrm{sim}} = 1.948\,64\,\mathrm{GHz}$ almost perfectly matching the experimental value.

The intensity of the simulated peak is about a factor of 15 higher than the measured peak which means that a higher portion of the signal passes into the resonator. This gets clear considering the coupling into the resonator of the simulation is ideal only considering losses in the conductor and in the STO substrate, whereas in reality a lot of factors lower the coupling intensity to some degree making it not perfect. Comparing the value of the quality factor Q however, yields 27.7 for the simulation and 26 for the experiment being in sufficient agreement.

The deviation of simulation to theory and experiment for both the resonance frequency ν_0 and the quality factor Q is less than around 5 % which is in an acceptable range considering the experimental error. The major errors to name are probably the misalignment of the substrate, deviations in the resonator length and the inhomogeneous electric field distribution and not ideal coupling process in a coplanar resonator.

In general however, the consistency of theory, simulation and experiment has been shown and is in an acceptable range. This makes the simulations an applicable tool to study and optimize the resonator models of chapter 4 in the following.

5.2. Functionality of the resonator models

5.2.1. Conventional coplanar half-wavelength resonator

The conventional coplanar $\lambda/2$-resonator model was probed for its functionality by simulating the resonance frequency in dependence of the dielectric constant of the external STO sample up to around 24000 which thus corresponds to a temperature range down to mK-temperatures. The substrates were assumed to be lossless for this simulation as only the resonance frequency position was monitored.

Figure 5.3 shows the results of this simulation: The simulated resonance frequency of the fundamental mode ν_0 (dark blue dots) and the theoretical behavior calculated with conformal mapping technique (dark blue solid line) in dependence of the dielectric constant ϵ_1 for a distance (a) $h = 0$ and (b) $h = 100\,\mu\text{m}$ of the sample to the resonator chip. For $h = 0$, the simulated values perfectly follow the dark blue solid line and thus the $1/\sqrt{\epsilon_{\text{eff}}}$ behavior of the theoretical expectations (see equation (2.17)). For the lowest data point at $\epsilon_1 = 1$ the resonance frequency goes up to a value of around 19.26 GHz showing the ν_0-value of the unloaded Al_2O_3-resonator without the sample. When the STO sample comes into account, the effective dielectric constant ϵ_{eff} heavily rises, leading to a decrease and leveling off in resonance frequency.

Because of several reasons (mounting, gating, etc.) mentioned in section 4.1, the simulation was redone with a sample distance of around $h = 100\,\mu\text{m}$. For this distance, the simulated values for the resonance frequency ν_0 show the expected behavior but are slightly above the theoretic values. The air gap between sample and resonator chip is a known source of error for all coplanar resonators where a sample is externally placed on top of the chip [84]. One major reason for the discrepancy of simulation and theory is that the conformal mapping technique assumes an infinitesimal thin and perfectly conducting conductor, isotropic and lossless dielectrics and most importantly an electric field of the resonator completely and

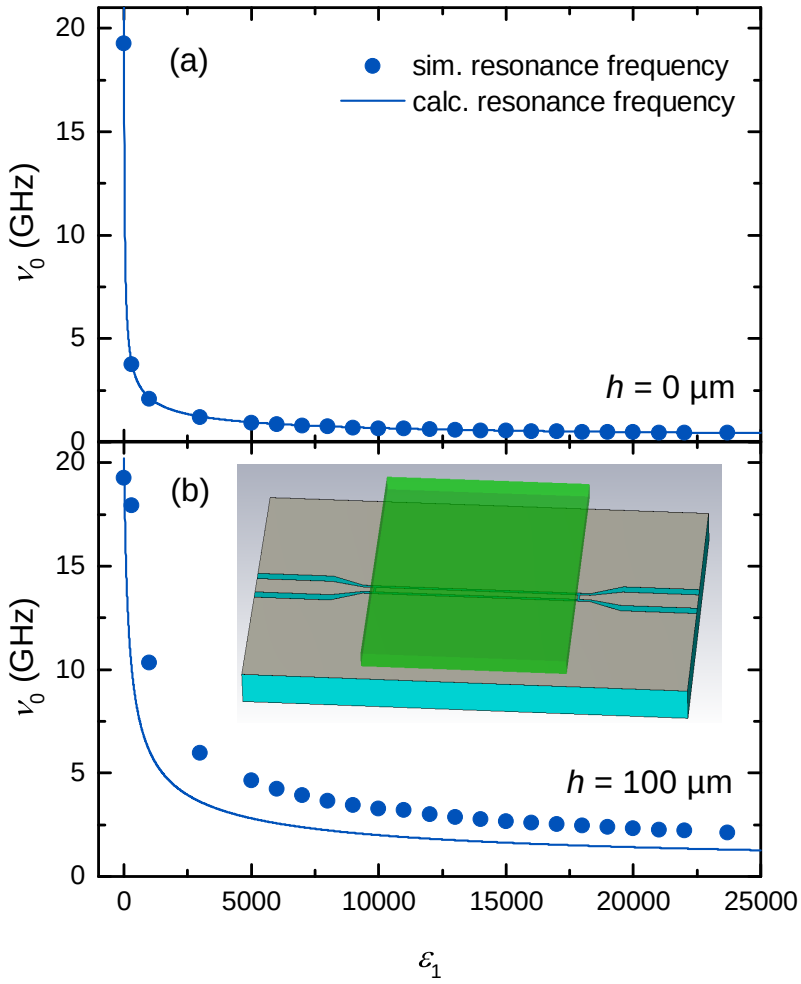

Fig. 5.3.: Simulated (dark blue dots) and theoretically calculated (dark blue solid line) resonance frequency ν_0 of the fundamental mode in dependence of the dielectric constant of the external STO sample at a distance (a) $h = 0\,\mu m$ and (b) $h = 100\,\mu m$ above the coplanar Al_2O_3-resonator. The inset in (b) shows a schematic sketch of this resonator structure for the simulation with the STO sample (transparent green) and the Al_2O_3 substrate (light blue).

homogeneously penetrating all parts of the present dielectrics. This is not the case in reality as well as simulation as the electric field of a coplanar resonator is not perfectly homogeneous. The presence of an air gap intensifies the problem that the sample is not completely penetrated by the electric field. Besides that, the discontinuity at the boundaries of the sample introduced by the air gap leads to depolarization effects reducing the fraction of electric field going into the sample. This gives a lower contribution of the dielectric constant ϵ_{sample} to the effective dielectric constant ϵ_{eff} lowering it and thus a slightly higher resonance frequency than in theory (see figure 5.3(b)) where this effect is not considered at all. A more detailed discussion of the air gap problem can be found in the master thesis of L. Wendel [85].

5.2.2. Capacitively coupled half-wavelength resonator

The capacitively coupled $\lambda/2$-resonator was also probed for its functionality by simulating the resonance frequency in dependence of the dielectric constant of the lossless STO substrate on the flipped resonator up to values of around 24000 and thus in a temperature range down to mK-temperatures. Figure 5.4 shows that this resonator device perfectly follows the theoretically expected $1/\sqrt{\epsilon_{\text{eff}}}$ behavior for all resonant modes and even for non-vanishing distances $h = 20\,\mu\text{m}$ and $h = 100\,\mu\text{m}$. This is due to the air gap not influencing the resonance frequencies of the flipped resonator since the STO substrate dominates the effective dielectric constant. Here, the air gap is only responsible for the coupling of the signal from the feedline to the resonator. Thus, the air gap problem can be avoided with this flip-chip geometry. The simulations show the resonator model is operable in theory and simulation for very high dielectric constants even for non-vanishing distances h.

5.2.3. Inductively coupled quarter-wavelength resonator

The inductively coupled $\lambda/4$-resonator also has the advantages of the flip-chip design and thus is functioning in theory as well as simulation up to a very high dielectric constant and for the distances $h = 50\,\mu\text{m}$, $100\,\mu\text{m}$, $200\,\mu\text{m}$ as depicted in figure 5.5. This also establishes the temperature range for resonator operation on the substrate STO down to mK-temperatures.

5.3. Performance of the inductively coupled quarter-wavelength resonator

In this section, the performance, such as coupling and quality factors, of the inductively coupled $\lambda/4$-resonator model is investigated in detail. This model has been chosen as the main design of this project due to the following reasons:

The advantages over the conventional coplanar $\lambda/2$-resonator are that the model does not have such a high impedance mismatch and does not show the air gap problem because the distance h is only responsible for the coupling and not the resonance frequency shift. Furthermore, the LAO/STO interface would be directly forming the resonator line and would be thus experimentally accessible while for the conventional $\lambda/2$-model, the LAO/STO interface would be external as a sample leading to potential measurement difficulties.

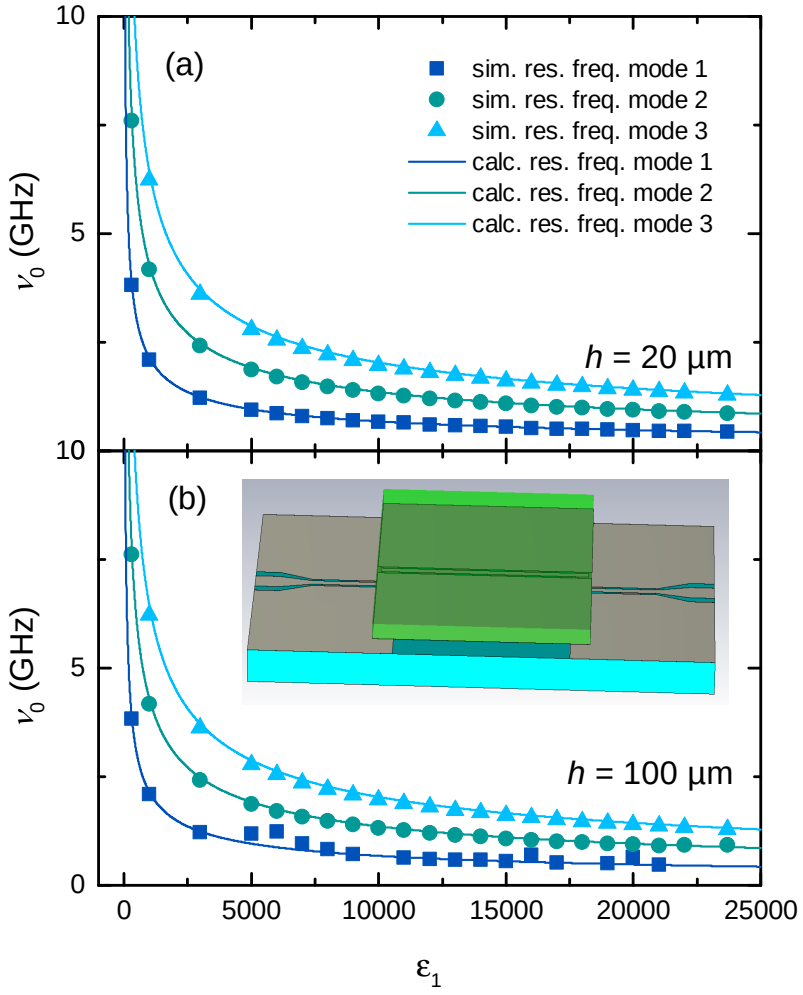

Fig. 5.4.: Simulated (dots) and theoretically calculated (solid lines) resonance frequency ν_0 of the first three modes ($n = 1, 2, 3$) in dependence of the dielectric constant of the STO substrate on the flipped $\lambda/2$-resonator with a distance (a) $h = 20\,\mu m$ and (b) $h = 100\,\mu m$ above the coplanar Al_2O_3-feedline. The inset in (b) shows a schematic sketch of this resonator structure for the simulation with the STO substrate (transparent green) and the Al_2O_3 substrate (light blue).

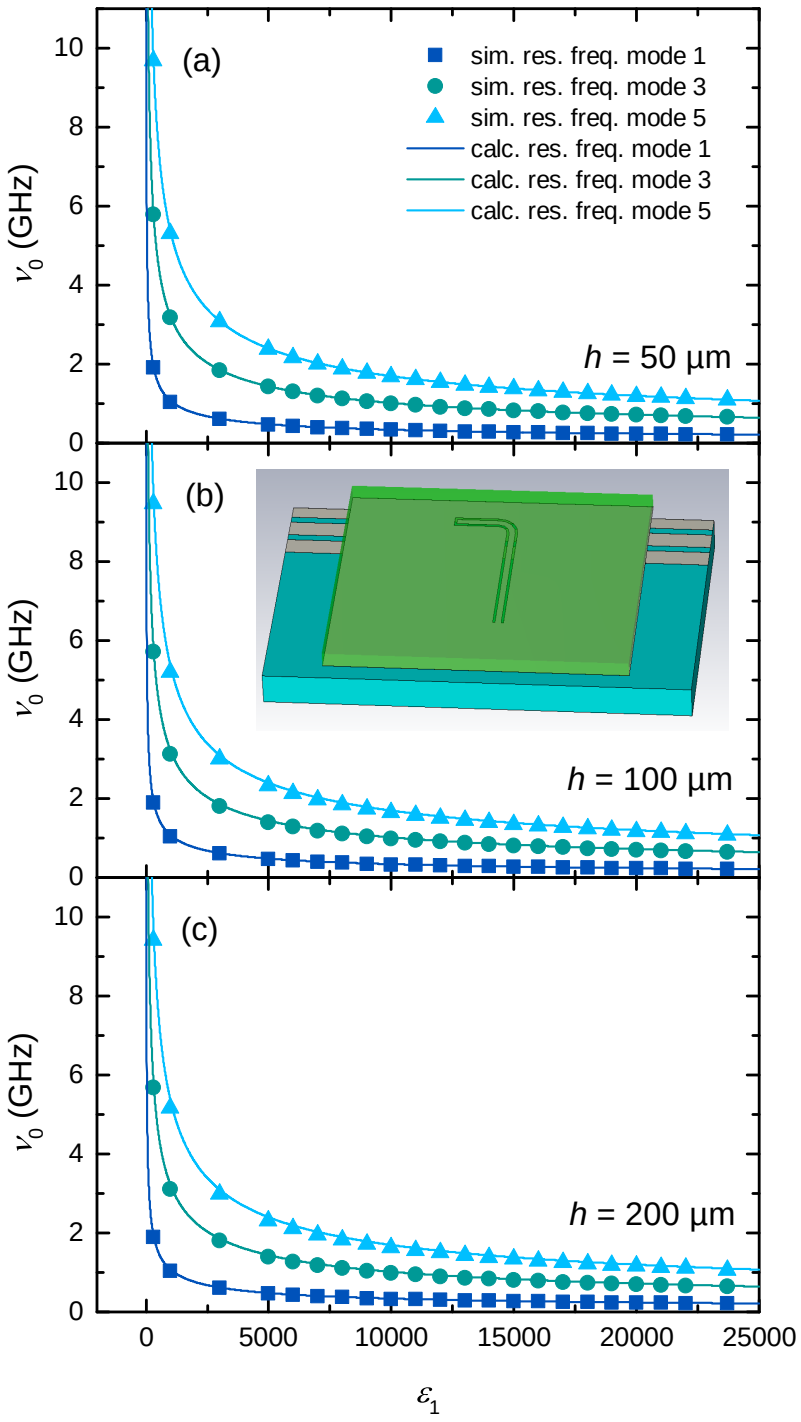

Fig. 5.5.: Simulated (dots) and theoretically calculated (solid lines) resonance frequency ν_0 of the first three modes ($n = 1, 3, 5$) in dependence of the dielectric constant of the STO substrate on the flipped $\lambda/4$-resonator with a distance (a) $h = 50\,\mu m$, (b) $h = 100\,\mu m$ and (c) $h = 200\,\mu m$ above the coplanar Al_2O_3-feedline. The inset in (b) shows a schematic sketch of this resonator structure for the simulation with the STO substrate (transparent green) and the Al_2O_3 substrate (light blue).

The advantages of the flipped $\lambda/4$-model over the flipped $\lambda/2$-model are the following:

The mounting of the resonator over the feedline only depends on the alignment in two directions in space rather than three for the $\lambda/2$-model. In addition to that, the coupling of the model can be controlled more easily, because only one feedline chip is necessary for all flipped $\lambda/4$-resonators chips. The $\lambda/2$ model would need a new feedline chip for every change in the feed length l_f. The gating process is also enormously easier with the $\lambda/4$-model because the inner and outer conductors are on the same potential and not isolated by the gaps W like with the $\lambda/2$-model. All these advantages give a competitive edge to the flipped $\lambda/4$-model and therefore it is being analyzed in the following by more detailed simulations.

5.3.1. Lossless coupling performance

Firstly, the coupling process into the resonator is investigated by evaluating the influence of the two coupling parameters distance h and coupling length l_c on the quality factor Q. For that purpose, the two parameters were swept through while keeping the other coupling parameter constant. The conductor was assumed to be perfectly electrically conducting and the STO substrate was assumed to be lossless with a dielectric constant $\epsilon_{1,\mathrm{STO}} = 300$. Figure 5.6 shows the results of these simulations.

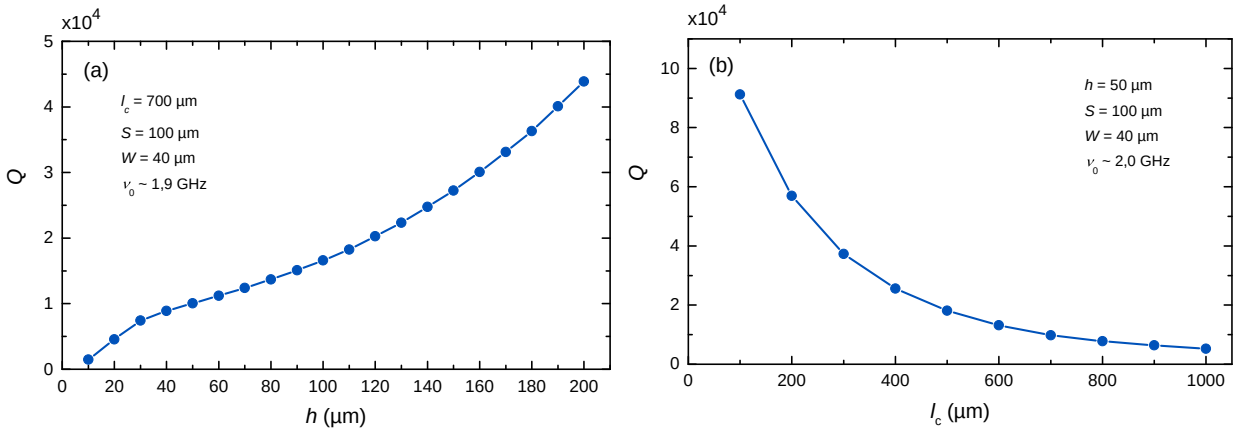

Fig. 5.6.: Quality factor Q simulation of the $\lambda/4$-resonator model in dependence of the two coupling parameters: (a) distance h and (b) coupling length l_c for a perfect electric conductor, non-lossy STO and Al_2O_3 substrate at room temperature.

The graphs show that an increase in the coupling leads to a decrease in the quality factor and vice versa. An increase in the sample distance h for example leads to a weaker coupling and therefore a higher quality factor up to a value of around 4.5×10^4. For the coupling length l_c, it is the other way round because an increase leads to better coupling. The maximum quality factor in this simulation is reached at the shortest coupling length of 100 µm being around 9×10^4. This yields that in the range of interest of the two coupling parameters, the coupling length l_c has a higher impact on the coupling process and thus quality factor Q. In the undercoupled regime (for very high h and low l_c), the quality factor would diverge

to infinity as the graphs indicate. This is due to the non-lossy dielectrics and the perfectly conducting material nearly making the coupling process ideal.

5.3.2. Lossy coupling performance and optimization

As the divergent and non-lossy behavior is not expected in reality, the simulations have been repeated with lossy assumptions making it possible to optimize the resonator operation as a saturation of the quality factor is expected for decreasing coupling.

The two coupling parameters were swept through while keeping the other one constant. When sweeping through the coupling length l_c, the total resonator length $l = l_\mathrm{c} + l_\mathrm{r}$ was always kept constant to not change the position of the resonance frequency. This was done by adjusting the length l_r of the non-parallel arm of the resonator to the feedline (see figure 2.3 in theory section 2.3.1 for clarification) when changing l_c so that $l = l_\mathrm{c} + l_\mathrm{r} = \text{const}$.

For the Al_2O_3 substrate, a by *CST MWS* predefined lossy sapphire substrate ($\epsilon_1 = 9.9$ and $\tan\delta = 10^{-4}$) was used and for the STO substrate a material with a dielectric constant $\epsilon_1 = 300$ and a loss tangent $\tan\delta = 10^{-3}$ was introduced.

To account for the losses in the superconducting material, a surface impedance model [86] was used to simulate the material Nb. The surface impedance model assumes a superconducting current besides a normal metallic current following the two-fluid model as introduced in section 2.2. In electromagnetic simulations, metallic losses are simply described by the surface impedance in dependence of the electrical conductivity σ_n and the skin depth δ with [86]

$$Z_\mathrm{S} = (1+i)R_\mathrm{S} = (1+i)\frac{1}{\delta\sigma_\mathrm{n}}\,. \tag{5.1}$$

However, in a superconducting material, the superconducting current also contributes to the conductivity as [86]

$$\mathbf{j} = \mathbf{j}_\mathrm{n} + \mathbf{j}_\mathrm{s} = \sigma\mathbf{E} = (\sigma_\mathrm{n} + \sigma_\mathrm{s})\mathbf{E} \tag{5.2}$$

with the superconducting conductivity $\sigma_\mathrm{s} = i\left[\omega\mu\lambda_\mathrm{L}^2(T)\right]^{-1}$ and $\lambda_\mathrm{L}(T)$ following the behavior of equation (2.14) and figure 2.1. The model accounts for the surface impedance with volume discretization methods based on the two-fluid model and transmission line theory to simulate superconductors of thickness t (see [86] for a detailed derivation). Note that in general, the normal conductivity σ_n in the normal and the superconducting state is not the same (Mattis-Bardeen theory [87, 88]). For the purpose of this simulation with a very narrow frequency range though, it is neglected.

In the simulation, a thickness $t = 300\,\mathrm{nm}$, a critical temperature $T_\mathrm{c} = 9.3\,\mathrm{K}$, a London penetration depth $\lambda_\mathrm{L}(0) = 71.5\,\mathrm{nm}$ [86] and a conductivity $\sigma_\mathrm{n} = 128\,\mathrm{S/\mu m}$ [86] was assumed to simulate Nb. Figure 5.7 depicts the findings of these simulations.

The figure shows the simulated results of the quality factor Q (top) and resonator absorption $\max(S_{21}) - S_{21}(\nu_0)$ (bottom) of the $\lambda/4$-resonator model in dependence of the distance h (left) and the coupling length l_c (right). $S_{21}(\nu_0)$ refers to the value of the S_{21}-parameter exactly in the dip of the resonance frequency and $\max(S_{21})$ refers to the constant S_{21}-parameter close to the resonance frequency but well away in the constant area (see right side of figure 2.4).

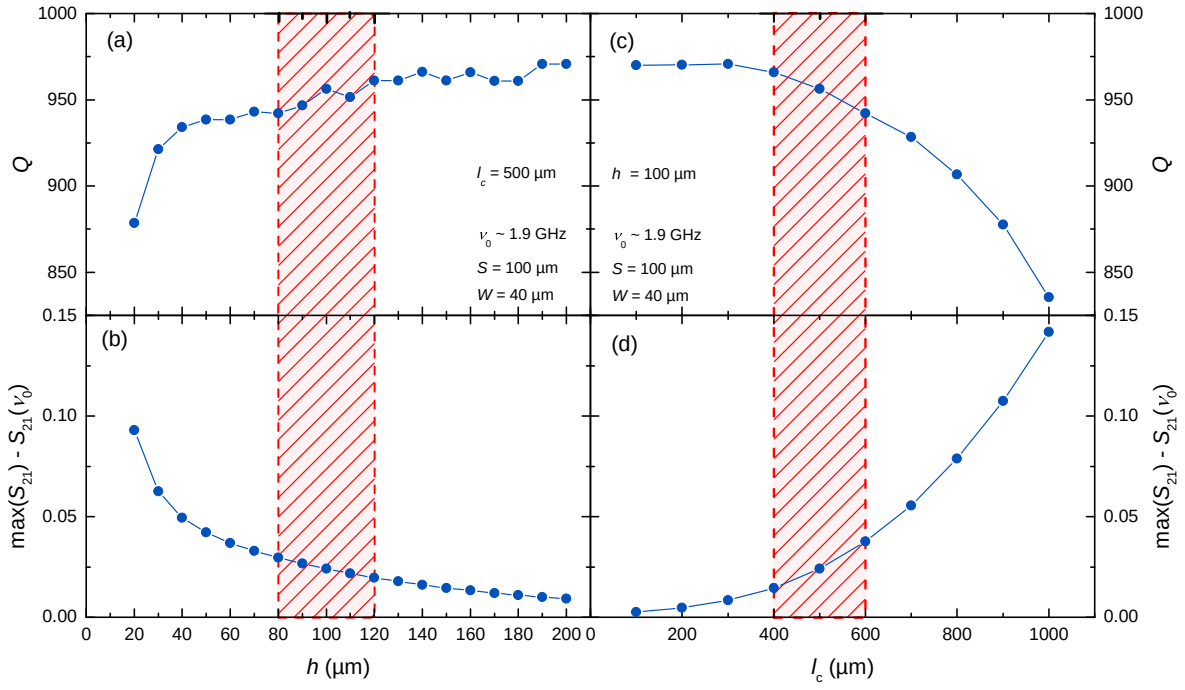

Fig. 5.7.: Quality factor Q (top) and resonator absorption $\max(S_{21}) - S_{21}(\nu_0)$ (bottom) simulation of the $\lambda/4$-resonator model in dependence of the distance h (left) and the coupling length l_c (right) for a Nb-conductor and a lossy STO as well as Al_2O_3 substrate at room temperature. $S_{21}(\nu_0)$ refers to the value of the S_{21}-parameter exactly in the dip of the resonance frequency and $\max(S_{21})$ refers to the constant S_{21}-parameter close to the resonance frequency but well away in the constant area (see right side of figure 2.4).

The difference $\max(S_{21}) - S_{21}(\nu_0)$ thus defines the signal absorbed from the resonator out of the feedline signal.

One can clearly see that the quality factors Q now level off in the undercoupled regime as expected. This off-leveling is at a quality factor of around $Q = 970$ for both the distance h and the coupling length l_c. In the overcoupled regime the quality factor quickly decreases.

The absorption of the resonator shows the opposite behavior. In the overcoupled regime, a relatively big fraction of the feedline signal (around 0.1-0.15) couples into the $\lambda/4$-resonator then quickly decreases to a value close to 0 in the undercoupled regime.

The red areas in the graphs mark the optimal coupling range of the two coupling parameters. In this area, the high leveled off quality factor is almost reached and not close to the overcoupled area but still a sufficient signal gets absorbed into the resonator making a detection and therefore measurement possible. The optimal coupling values were found to be around $h = 100\,\mu m$ and $l_c = 500\,\mu m$ (see red area in figure 5.7).

Note, that in an experiment one can also change the coupling parameters slightly to the overcoupled regime to get a higher absorption signal at a cost of quality factor or the other

way round to get a better quality factor at a cost of absorption signal. The first one is more viable, as the measurement signal for STO resonators is very low and hard to detect.

5.3.3. Temperature dependent behavior

In the previous simulations, the dielectric constant of the STO substrate was kept at the room temperature value $\epsilon_1 = 300$ and the loss tangent was assumed to be constant at $\tan\delta = 10^{-3}$. The assumption of that value generally reflects the overall losses of STO but when operating the resonator device, the real temperature dependent behavior is of great interest.

For that purpose, value pairs of the dielectric constant ϵ_1 and the loss tangent $\tan\delta$ for different temperatures (measured in the GHz-regime) have been taken from [22] (also see green dots in figure 3.2) and assigned to the STO substrate to simulate the real behavior of the quality factor as a function of temperature. The conductor was again assumed to be Nb at a constant temperature of 1.6 K so well below T_c. Figure 5.8 shows the results of these simulations.

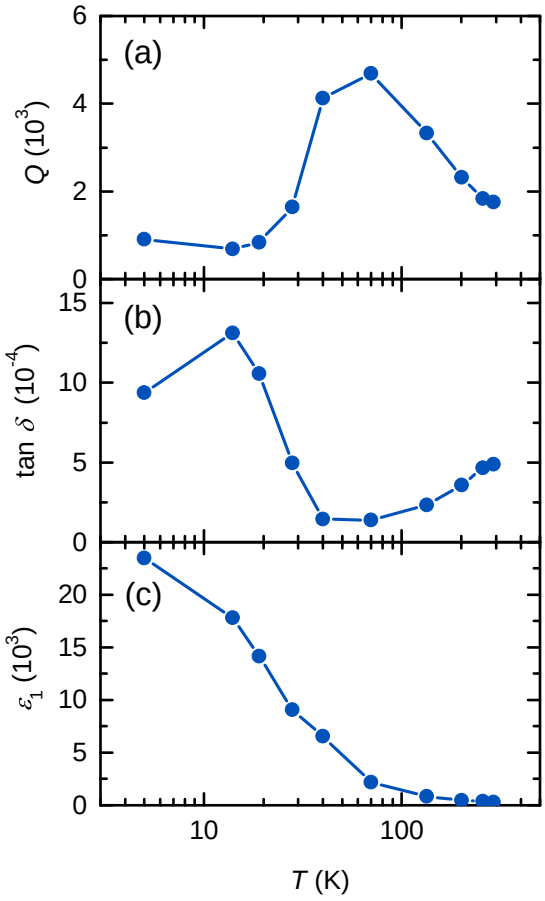

Fig. 5.8.: (a) Simulated quality factor Q, (b) Loss tangent $\tan\delta$ of STO, (c) Dielectric constant ϵ_1 of STO in dependence of the temperature for $h = 100\,\mu\text{m}$ and $l_c = 700\,\mu\text{m}$. Data in (b) and (c) taken from [22].

The losses of the STO substrate dominate the behavior of the quality factor Q as the quality factor shows the opposite behavior of the loss tangent $\tan\delta$. When the loss tangent firstly increases for low temperatures the quality factor goes slightly down. Then at around 10 K the losses start to drop which leads to an increase in the quality factor and vice versa from around 40 K to room temperature. The behavior of the dielectric constant has no significant impact on the quality factor. This is because the broadening and narrowing due to losses dominate over the resonance frequency shift due to the change in the dielectric constant.

Overall, the values of the quality factors are in an acceptable range of around $2000 - 4000$ for the high temperature values but more importantly around 1000 for the low temperature values of under 20 K. The most significant value for our goals, at $T = 5\,\text{K}$, reveals a quality factor of $Q = 910$. This value is of great interest for operating the resonator model in a potential experiment in e.g. a helium bath cryostat and is relatively high and in an acceptable range to operate the resonator model.

6. Experimental principles

6.1. Setups

In the framework of this project, two setups have been used for the majority of the experiments: A liquid helium VTI bath cryostat for the microwave measurements in the temperature range of 1.4 to 300 K and in addition to that, the critical temperatures T_c of the Nb films were measured in a SQUID magnetometer. To perform experiments in the mK-temperature range, a ^{3}He/^{4}He dilution refrigerator has been used, but will not be explained in detail here. A detailed description of this setup can be found in [26].

6.1.1. VTI bath cryostat

For all measurements to low temperatures in this thesis a VTI ^{4}He bath cryostat is used. A schematic sketch of the setup can be seen in figure 6.1. A variable temperature insert (VTI) is placed in a sample chamber covered by an inner vacuum. At the very end of the VTI is a metallic sample holder where the microwave resonator and the coaxial cables are mounted. A VNA performs the microwave measurements in a range of 0.01 to 50 GHz. The temperature gets controlled by a temperature sensor and heater placed at the sample holder. Cooling is realized by a needle valve allowing a flow of liquid helium from the ^{4}He bath which is covered by an outer vacuum to the inner sample chamber. A vacuum pump lowers the pressure in the sample chamber reducing the boiling point of the liquid helium to allow cooling down to a temperature of around 1.4 K.

An operation manual of the VTI bath cryostat can be found in [89].

6.1.2. SQUID magnetometer

In order to analyze the critical temperature T_c of the Nb films, magnetic moment measurements on them are performed using a superconducting quantum interference device (SQUID) magnetometer in a magnetic property measurement system (MPMS). The measuring method is based on the Josephson effect and the flux quantization in a superconducting loop. By moving the superconducting Nb samples through a superconducting loop, the magnetic flux in the loop changes and a current can be measured using the Josephson effect. This allows to measure the magnetization of the sample in dependence of the temperature and therefore to obtain the critical temperature T_c.

An operation manual of the SQUID magnetometer can be found in [90].

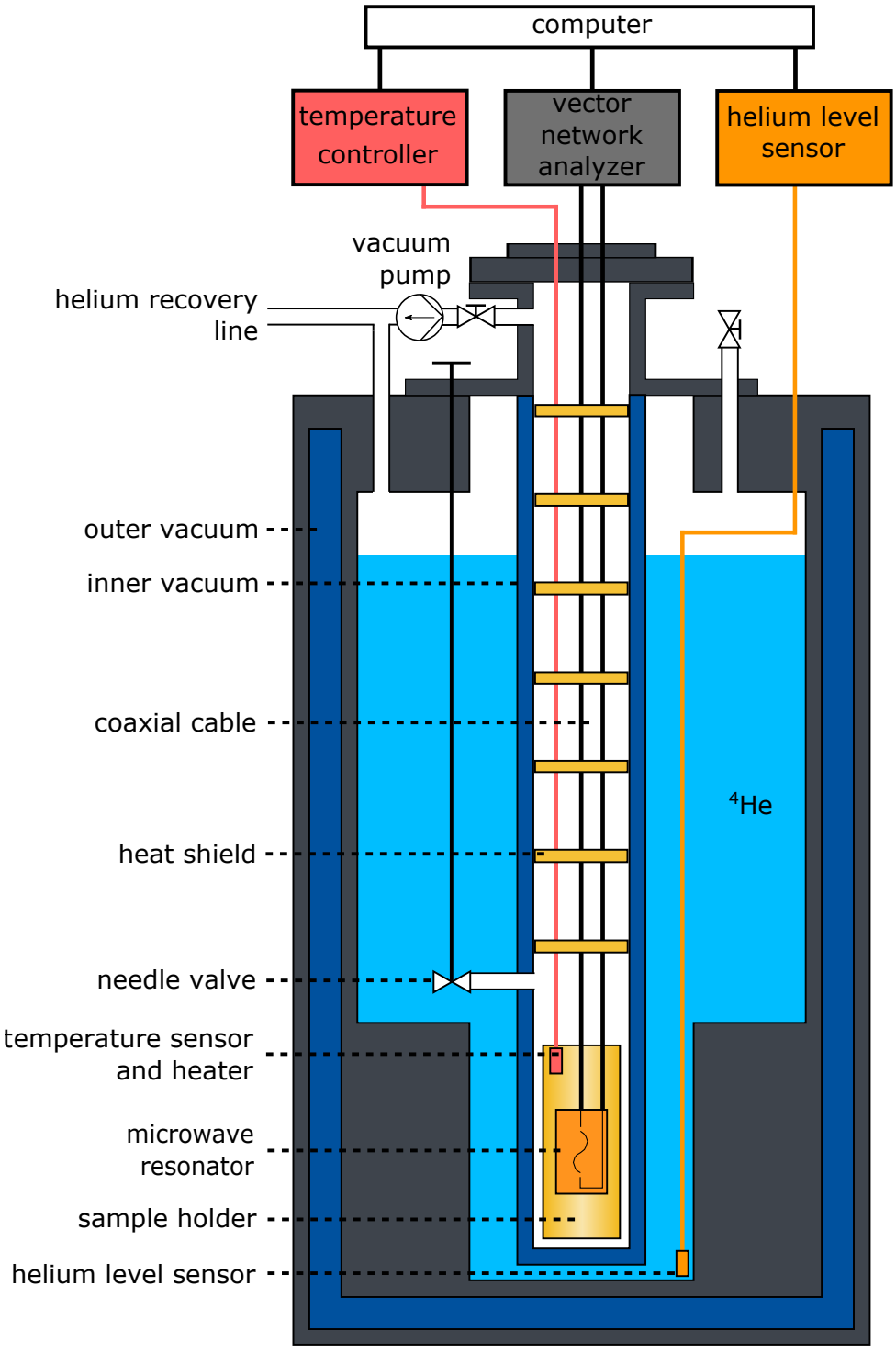

Fig. 6.1.: Schematic setup of the VTI bath cryostat (not to scale). The components include the bath cryostat itself, a vector network analyzer to perform microwave measurements, a temperature controller with a temperature sensor and heater as well as a helium level sensor to control the helium level.

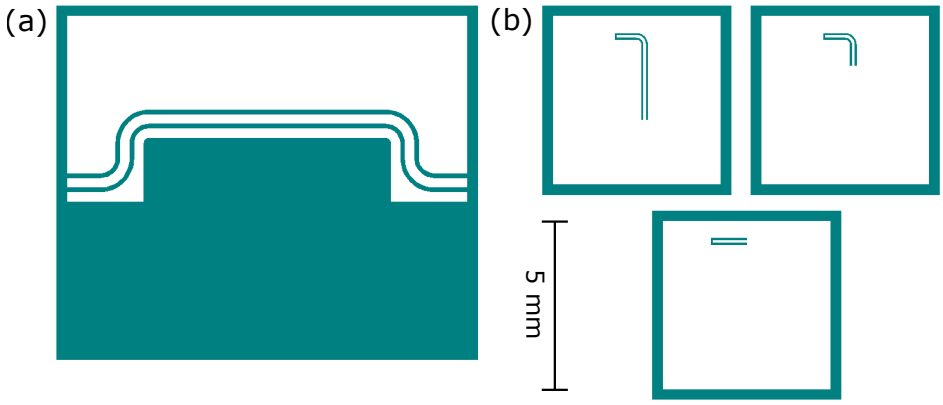

Fig. 6.2.: Schematic sketches of the designed resonator masks for the lithographic process, the white areas will be the conducting area after the process. (a) Feedline mask for fabrication on sapphire. (b) Several resonator masks of different resonator lengths l for fabrication on STO.

6.2. Experiment

6.2.1. Resonator fabrication

The superconducting coplanar $\lambda/4$-resonators on the substrate STO were realized using the element superconductor niobium (Nb). For that purpose, a 300 nm thin film of Nb is sputter-deposited on a 200 µm thin substrate of STO ($5 \times 5\,\mathrm{mm}^2$). The actual resonator structure is then shaped by optical lithography. The resonator masks can be seen in figure 6.2, where (a) shows the mask of a feedline. White areas in the mask will form the conducting part of the feedline, clearly depicting inner and outer conductor. The lower part of the chip is kept free of metal to not perturb the resonator and dielectric mounted on top of it. The feedline conductor parameters were chosen to be $S_\mathrm{f} = 300\,\mu\mathrm{m}$ and $W_\mathrm{f} = 120\,\mu\mathrm{m}$. The feedline boxes have a size of $12 \times 10\,\mathrm{mm}^2$.

Figure 6.2(b) shows the masks of several resonator chips. Resonators with the length $l = 3200\,\mu\mathrm{m}$, $l = 1600\,\mu\mathrm{m}$ and some several smaller ones were designed, while the coupling length l_c was always swept from 500 µm to 1000 µm while keeping the total resonator length l constant. The inner conductor width was chosen to be $S = 100\,\mu\mathrm{m}$ and the gap from inner to outer conductor $W = 40\,\mu\mathrm{m}$ for every chip. Both the sputtering and the optical lithography were carried out by the 4. Physikalisches Institut at the University of Stuttgart [91]. For an exact description of the fabricated resonator model see section 4.4. Clean Nb has a critical temperature of around 9.2 K [33]. Therefore, the microwave measurements with these resonators have to be carried out at temperatures lower than T_c, ideally as low as possible.

6.2.2. Characterization of the Nb-films

After the sputtering process and before the lithography process, the Nb films of the resonators and the feedlines were characterized in the SQUID magnetometer to analyze the quality of

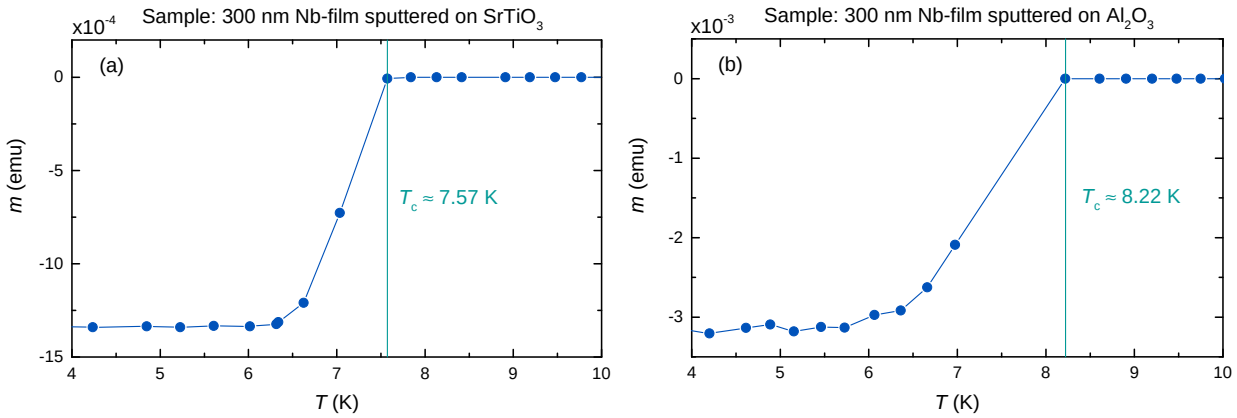

Fig. 6.3.: Magnetic moment m measurement of the Nb films on (a) an STO substrate and (b) an Al_2O_3 substrate revealing the onset critical temperatures T_c.

the films on the STO and the Al_2O_3 substrates and to obtain the critical temperature T_c. Figure 6.3 shows the superconducting transition and the critical temperatures for the Nb film (a) on an STO substrate and (b) on a sapphire substrate. T_c strongly depends on the quality of the films and thus on the sputtering process and on the material as well as surface roughness of the underlying substrate. Therefore, the critical temperatures are slightly below the literature value of Nb but in agreement with results of films previously obtained with the used sputtering facility. The critical temperatures were obtained using the onset method.

6.2.3. Distant flip-chip setup

The flipped resonator chip is placed on top of the feedline at a distance h to inductively couple the signal into the $\lambda/4$-resonator. Figure 6.4 shows the schematic setup of this distant flip-chip geometry with the STO substrate in green, the sapphire substrate in light blue and the superconductor Nb in gray.

On the left side, the non-flipped resonator with its characteristic parameters inner conductor width S, distance to outer conductor W and the coupling length l_c is shown. On the right side, the mounted flipped (indicated by the black arrows) chip with a transparent STO sample at a distance h over the feedline is depicted. The resonator chip is mounted in such a way that the coupling length l_c is parallel and centered above the feedline at a distance h.

The inset shows a photograph of the mounted resonator flip-chip in the feedline box. The inner conductor of the feedline is connected to the microwave connectors and the outer conductor to the box via silver paste. The distance h of the resonator chip to the feedline conductor is realized using vacuum grease in every corner of the chip. The feedline chip as well as the resonator chip are fixed using Fixogum. Under a microscope, the distance h was determined to be around 60 µm using a box with removable side walls (see appendix chapter A).

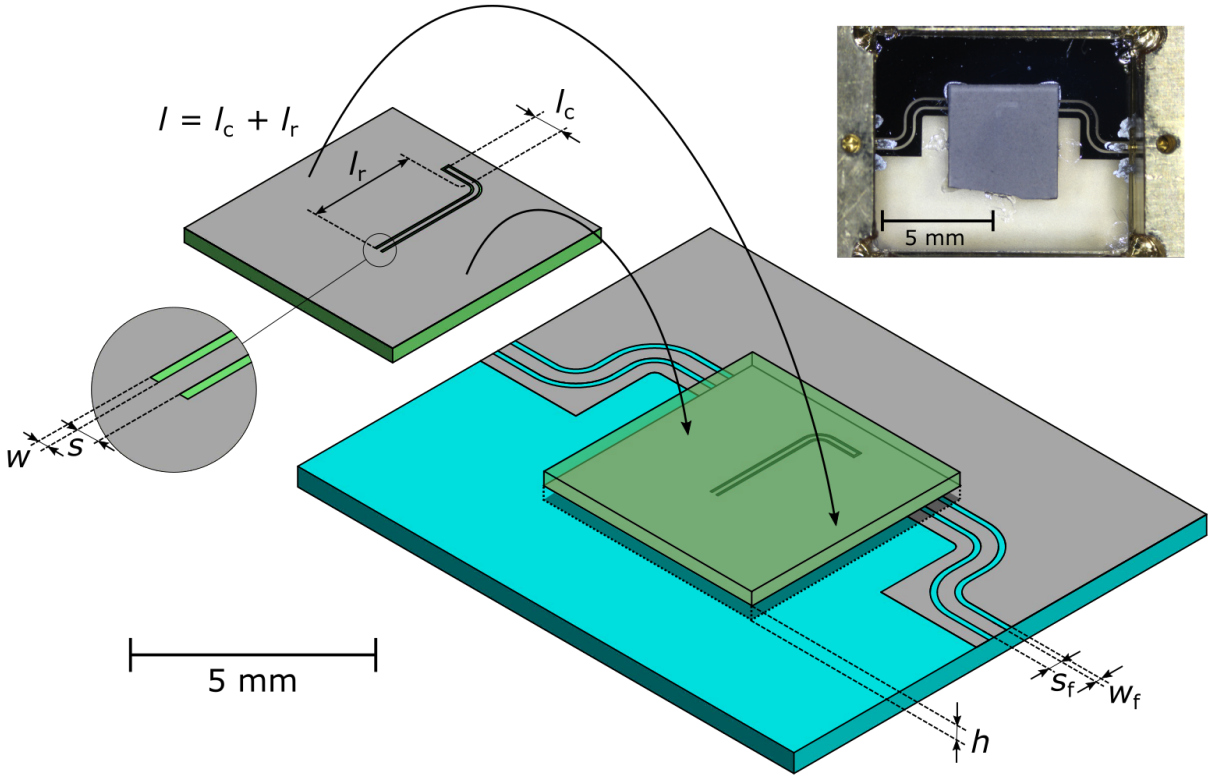

Fig. 6.4.: Schematic sketch of the distant flip-chip setup (to scale) The Nb film is shown in gray, the STO resonator substrate in green and the sapphire feedline substrate in light blue. The inset shows a photograph of the actual mounted chip where the parallel arm of the resonator above the feedline can be seen thorough the slightly transparent sample.

6.2.4. Fitting procedure

To gather desired data such as resonance frequency ν_0 or quality factor Q of the used microwave resonators from the measurement data acquired by the VNA, the data is being fitted. The form of sharp resonances ideally follows the one of a Lorentzian line shape (see equation (2.18)). One can directly fit this formula into the absolute values of the measured transmission ($T_\nu = S_{21}^2$). But as the microwave wavelength in the GHz-regime is in the same range as the dimensions of the typical experiment utilities, the transmission spectrum is affected by unwanted standing waves caused by the resonator box (so called boxmodes) and noisy background of the coaxial cables. A transmission spectrum of a superconducting $\lambda/4$-resonator on an STO substrate inductively coupled over a feedline for $T = 1.4\,\mathrm{K}$ can be seen in figure 6.5(a). The frequency dependent damping of microwave transmission lines causes a continuous decrease with increasing frequency. The sharp resonances originating from the resonator are marked by blue arrows. To take the deformations from an ideal Lorentzian shape caused by background and the boxmodes into account, a first order model for the background is used. The Lorentzian function is rewritten in a complex form including a first order Taylor expansion modeling the background (more details in [26]). This is fitted in the real and imaginary part of the measured S_{21}-parameter as shown in figure 6.5(b). The fit for the absolute values (see figure 6.5(c)) can then be derived from the complex data giving access to the resonance frequency ν_0 and the full width at half maximum ν_B characterizing the quality factor Q of a resonance.

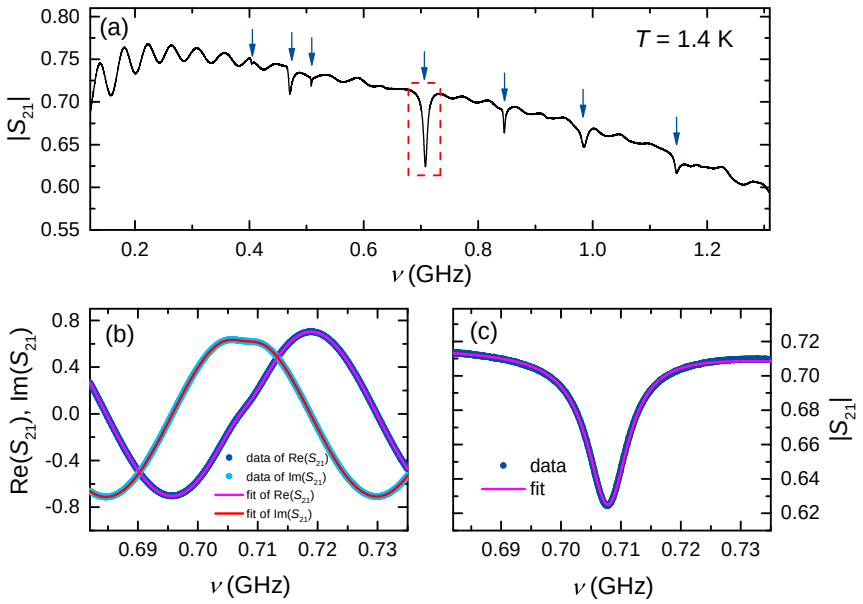

Fig. 6.5.: (a) Transmission spectrum of a $\lambda/4$-resonator on an STO substrate inductively coupled over a feedline for $T = 1.4\,\mathrm{K}$ up to around 1.3 GHz. Resonances are marked by blue arrows. (b) Measured real and imaginary parts and respective fit of the S_{21}-parameter of the highlighted resonance at around 0.71 GHz. (c) Measured absolute value and fit of the S-parameter $|S_{21}|$ of the highlighted resonance at around 0.71 GHz.

7. Results and Discussion

7.1. Metallic coplanar resonators on $SrTiO_3$

The approach to the LAO/STO resonator is done by two intermediate steps before, namely a metallic resonator and a superconducting resonator on STO. The realization of metallic $\lambda/2$-resonators on STO and their performance down to 15 K was successfully realised in my bachelor project [27]. This showed that it is fundamentally possible to realize a coplanar resonator on the substrate STO even with the high impedance mismatch and gave access to the temperature dependent dielectric properties of STO in the microwave regime.

In this present work, the temperature range was further expanded down to a value of 1.6 K. The obtained dielectric constant ϵ_1 of STO in dependence of the temperature can be seen in figure 7.1.

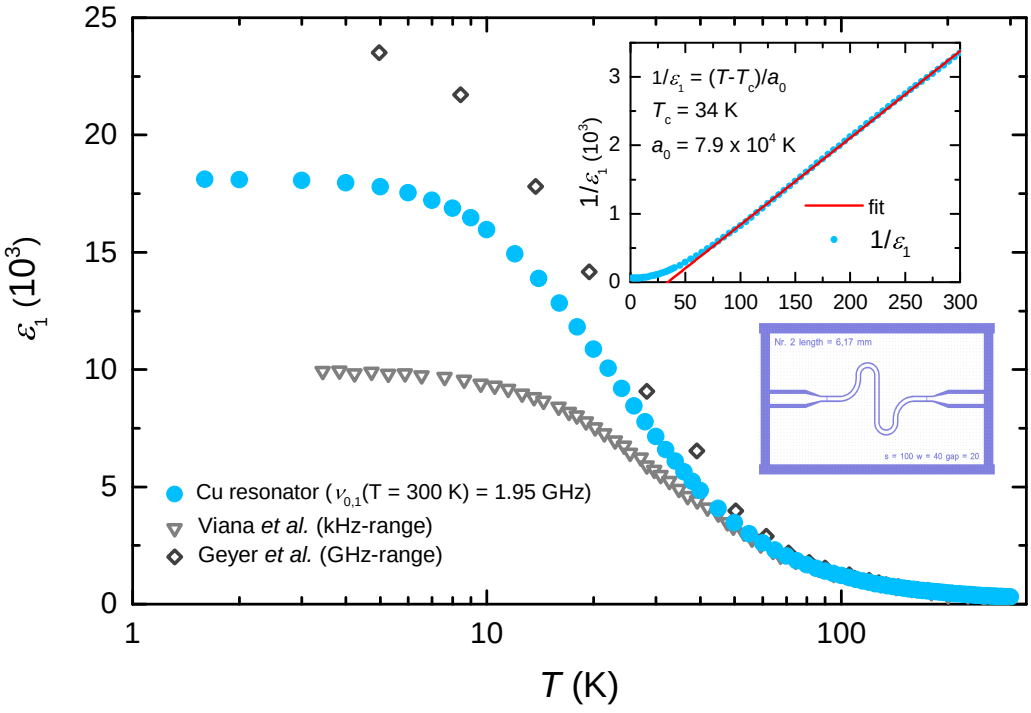

Fig. 7.1.: Dielectric constant ϵ_1 of STO in dependence of the temperature from 1.6 K to 300 K obtained with a Cu-resonator on STO. Values from [21] and [22] have been digitized and added to the plot for comparison. The insets show the inverse dielectric constant $1/\epsilon_1$ with a Curie-Weiss fit (red) and a resonator geometry sketch of the used $\lambda/2$-chip.

The dielectric constant of STO was evaluated by the measured position of the resonance frequency ν_0 using equation (2.17) for a $\lambda/2$-resonator and the approximation $\epsilon_{\text{eff}} = (\epsilon_{\text{STO}} + \epsilon_{\text{air}})/2$ which holds for $\epsilon_{\text{STO}} \gg \epsilon_{\text{air}}$ being the case for all given temperatures, here.

The behavior of the dielectric constant ϵ_1 is in agreement with other studies as shown in the figure. It starts to increase strongly starting with the phase transition at around 105 K. At around 4 K the dielectric constant levels off at a value of around 18.1×10^3 and stays constant down to the lowest measured temperature. This confirms the quantum mechanical fluctuations suppressing the ferroelectric phase transition and stabilizing the paraelectric state. The inset of figure 7.1 shows the inverse dielectric constant versus the linear temperature. The Curie-Weiss fit of the form

$$\epsilon = \frac{a_0}{T - T_{\text{C}}} \tag{7.1}$$

as defined in equation (2.9) was fitted in the high temperature values ($T > 100\,\text{K}$) and reveals a Curie-temperature $T_{\text{C}} \approx 34\,\text{K}$ and a Curie-Weiss constant $a_0 \approx 7.9 \times 10^4\,\text{K}$. Both values are in good agreement with previous works by other authors [20, 54, 57, 60]. The fit shows that the Curie-Weiss law is satisfied for temperatures from around 65 K to 300 K. For lower temperatures, the measured values depart from the Curie-Weiss law which can be explained by the phase transition and quantum effects occurring there [57].

In the interest of deriving some information on the dielectric losses ϵ_2 in STO out of the quality factors Q, the following procedure is used: The quality factor as defined in equation (2.19) is also connected to the resonator length l and the attenuation coefficient α for a $\lambda/2$-resonator via [47]

$$Q = \frac{\pi}{2l\alpha}\,. \tag{7.2}$$

The attenuation coefficient consists of three contributions being $\alpha = \alpha_{\text{c}} + \alpha_{\text{r}} + \alpha_{\text{d}}$. α_{c} is the attenuation in the conductor and α_{r} is the attenuation caused by radiation which can be neglected for frequencies below 100 GHz [92]. α_{d} accounts for the attenuation in the dielectric substrate. For the Cu-resonator on the substrate STO, α_{c} and α_{d} both have a significant impact on the overall losses. Thus, the overall attenuation coefficient is proportional to the reciprocal quality factor: $\alpha = \alpha_{\text{c}} + \alpha_{\text{d}} \propto 1/Q$. Note that the measured loaded quality factor Q is used interchangeably with the internal quality factor Q_{int} because the external factors are negligibly small. Comparing the resonator with the dielectric STO substrate and without the substrate (or a reference resonator) yields: $\alpha_d = 1/Q_{\text{d}} - 1/Q_0$ with Q_{d} being the measured quality factor Q with substrate and Q_0 being the quality factor of the resonator without a substrate (or the reference resonator). The attenuation of the conductor is approximately the same with and without the substrate and therefore cancels out. This allows the determination of the loss tangent $\tan\delta$ of the STO substrate using the equation [48]

$$\tan\delta = \alpha_{\text{d}} \left[\frac{q\epsilon_1 \pi \nu}{\sqrt{\epsilon_{\text{eff}}}c}\right]^{-1} \tag{7.3}$$

with the filling factor q and plugging in $\alpha_d = 1/Q_{\text{d}} - 1/Q_0$. Knowledge of $\tan\delta$ directly allows the calculation of ϵ_2 using equation (2.8)

$$\epsilon_2 = \epsilon_1 \tan\delta\,. \tag{7.4}$$

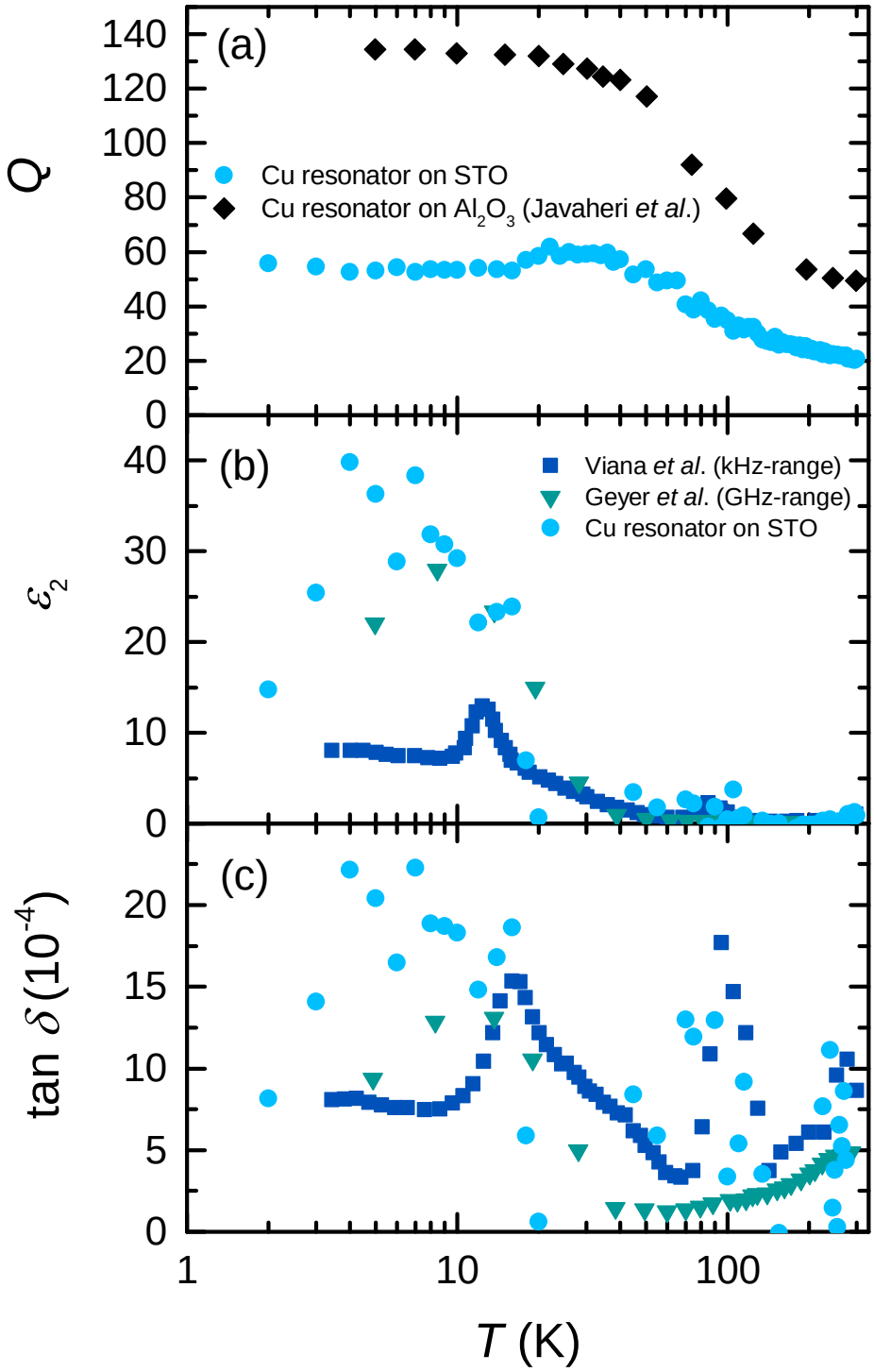

Fig. 7.2.: (a) Quality factors Q of the metallic Cu-resonator on STO (light blue) and a Cu-resonator on a sapphire substrate (black) taken from [42]. (b) Dielectric losses ϵ_2 of STO in dependence of the temperature obtained with the Cu-resonator on STO and from [21, 22]. (c) Loss tangent $\tan\delta$ of STO in dependence of the temperature from this work and [21, 22].

Figure 7.2(a) shows the measured quality factor of the Cu-resonator on the STO substrate and the quality factor of a reference Cu-resonator on an Al_2O_3 substrate taken from [42]. The temperature dependent behavior of the quality factor of the Al_2O_3-resonator can be assumed as the behavior of an empty resonator without a substrate as the losses of sapphire are very low [23, 24]. The Cu conductor was identically fabricated as with the STO-resonator and therefore gives a great temperature dependent reference. The calculations for ϵ_2 and $\tan\delta$ were performed using these quality factors shown in figure 7.2(a) while scaling them down to reach the best agreement with the dielectric loss data from Geyer *et al.* Note, that the obtained data for ϵ_2 and $\tan\delta$ therefore only show the qualitative behavior of the losses obtained with the Cu-resonator on STO and the absolute values are arbitrarily scaled to the values of Geyer *et al.* [22].

Figure 7.2(b) and (c) show the obtained data from the STO resonator and data from [21, 22]. The overall behavior of the losses is in agreement with the data also obtained in the GHz-range. The dielectric losses ϵ_2 are very low for the high temperature values and start to increase at around 20 K. At very low temperatures, a decrease in the losses of STO is indicated by the last two data points which may be of great potential for operating a resonant device on the substrate STO at very low temperatures e.g. a superconducting resonator on STO or an LAO/STO resonator. The structural phase shift at around 105 K which can be seen as an absorption peak in the dark blue data of $\tan\delta$ is also indicated in the measured data of this work.

In general the realization of the metallic $\lambda/2$-resonator on the substrate STO showed that it is fundamentally possible to drive a functioning resonator on STO despite the high impedance mismatch generated by the STO substrate. The resonator also gave access to the dielectric properties of STO in a broad temperature range. The dielectric constant ϵ_1 and the dielectric losses ϵ_2 show great agreement in both qualitative and quantitative behavior compared to existing theoretical models and previously published works by other authors.

7.2. Superconducting coplanar resonators on $SrTiO_3$

The second and final step before realizing the LAO/STO resonator is the realization of a superconducting resonator on STO. This is done to probe the resonator operation at low temperatures and in the superconducting state. The resonator is analyzed in terms of the resonance frequency ν_0 and thus dielectric properties of STO and the quality factor Q to later directly transform it to the LAO/STO resonator. The used resonator model was described in section 4.4 and the fabrication of the resonators as well as the experimental setup of the distant flip-chip geometry was described in chapter 6 of this thesis.

The superconducting Nb-resonator of length $l = 3200\,\mu m$ and coupling length $l_c = 600\,\mu m$ on an STO substrate (100) with a thickness of 200 µm has been measured at cryogenic temperatures in the VTI bath cryostat. Figure 7.3 shows the results of this measurement. The observed absorption modes of the resonator appear as Lorentzian line shape dips in the feedline signal spectrum. There are around seven modes visible in the spectrum up to a frequency of $\nu \approx 1.6\,GHz$. For the lowest temperature of $T = 1.4\,K$, the modes show the highest absorption and are the sharpest. With increasing temperatures, the modes shift to

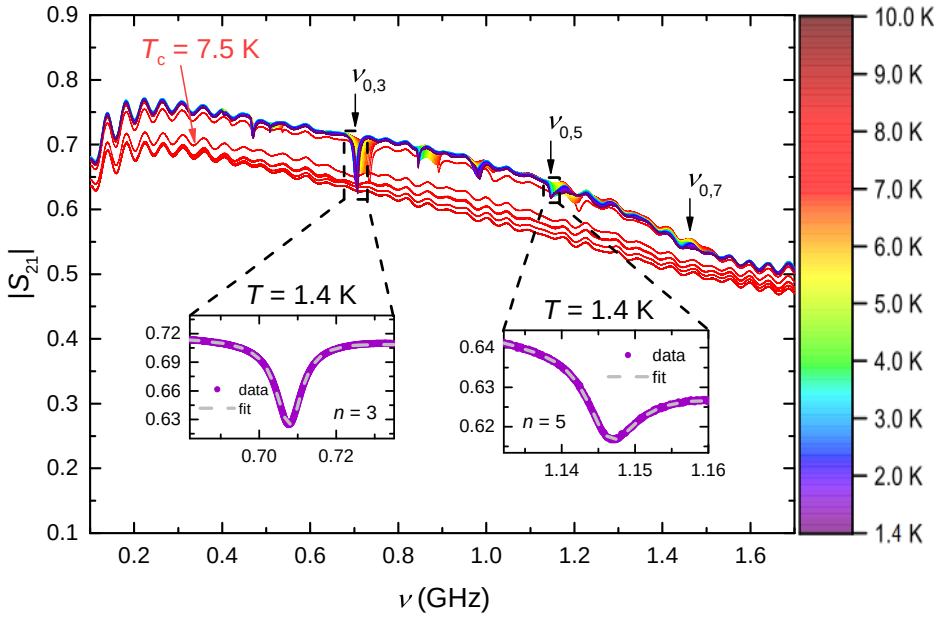

Fig. 7.3.: Transmission spectra of the superconducting $\lambda/4$-resonator on an STO substrate inductively coupled with a feedline in the temperature range from $T = 1.4\,\mathrm{K}$ to $T = 10\,\mathrm{K}$ and up to a frequency ν of around 1.6 GHz. The insets show a Lorentzian line shape fit of the modes $n = 3$ and $n = 5$ originating from the resonator for the lowest temperature.

higher frequencies and then abruptly disappear at a temperature of around $T = 7.5\,\mathrm{K}$. This is due to the superconducting transition of the Nb conductor which the feedline as well as the resonator conductor consist of. This critical temperature is in agreement with the SQUID magnetometer measurements done in advance (see section 6.2.2). The disappearance of the resonant absorption dips results from the transition of the Nb to its non-superconducting state and thus an enormous increase in resistivity. Above T_c, the feedline signal shows no absorption dips and just consists of standing wave background.

The three modes marked with black arrows are the desired resonant modes coming from the absorption of the $\lambda/4$-resonator on STO. This statement gets supported by the fact that these modes have the highest intensity and match the expected dielectric constant ϵ_1 of STO with their resonance frequency position (shown later on). This approves the realization of a superconducting Nb $\lambda/4$-resonator directly on STO operating at frequencies exceeding 1 GHz. This is the highest frequency of a planar superconducting resonator device on STO so far and about a factor of 3 higher than with the resonators published by the groups in Delft [7] and Paris [28] presented in section 3.2 of this thesis.

The fundamental mode which is expected to occur at a frequency of around 0.24 GHz was not observed in the measurement. Possible reasons for this are the heavily increasing S_{21}-signal which is typical for the feedline in that frequency range and the also typical lower sensitivity of the VNA in that area. The remaining other resonant modes in the spectra are assumed to be boxmodes or other undesired parasitic modes as they also depend on T

and disappear above T_c. The insets of figure 7.3 show respective fits to the modes for $n = 3$ and $n = 5$ at the lowest temperature of $T = 1.4\,\mathrm{K}$. The mode for $n = 7$ could not be fitted due to low intensity but shows the expected resonance frequency shift to higher frequencies with increasing temperatures. The modes for $n = 3$ and $n = 5$ have been fitted for every temperature value by subtracting a background using the spectrum of $T = 10\,\mathrm{K}$, well above T_c where all modes disappeared, to allow a more reliable fitting procedure.

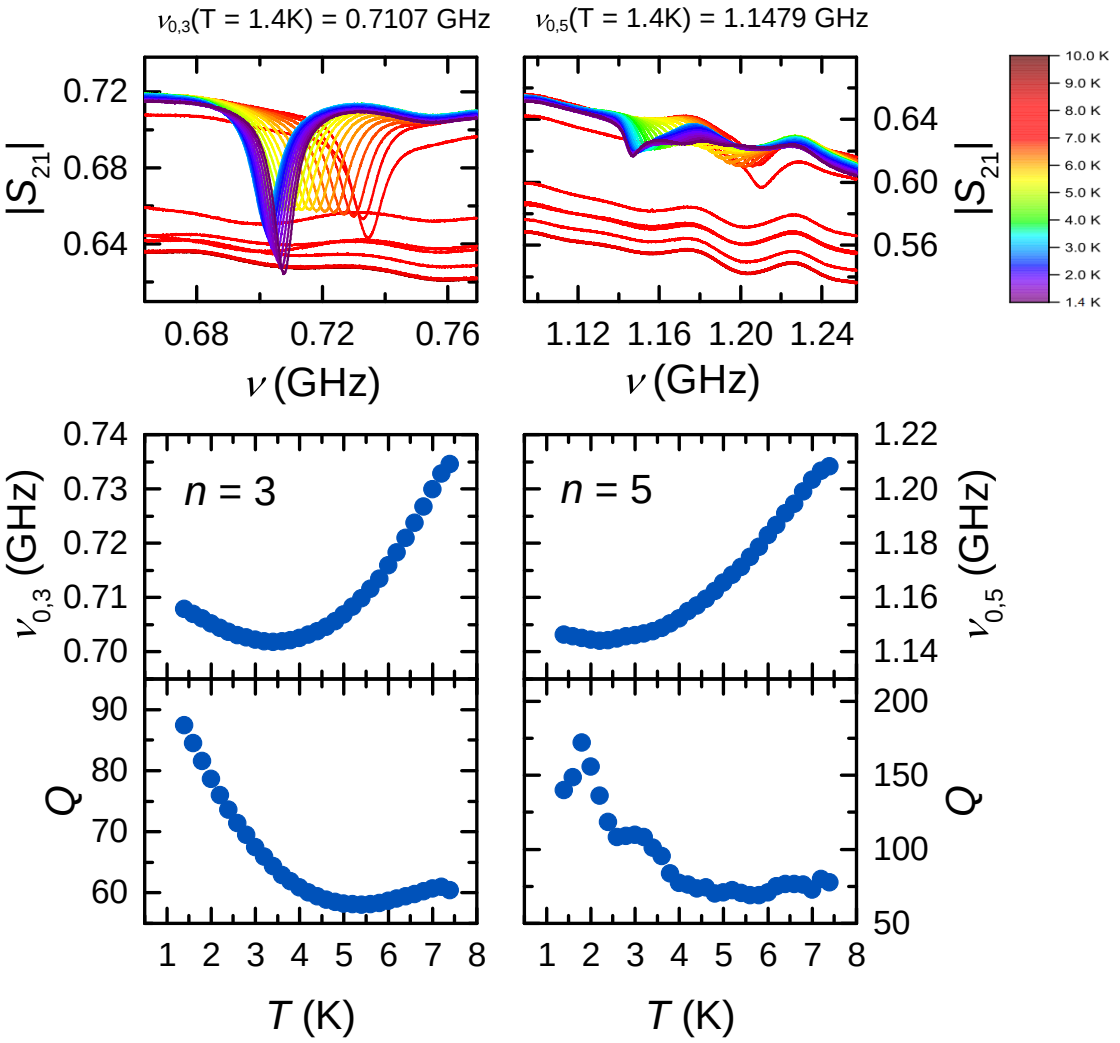

Fig. 7.4.: Analysis of the observed modes $n = 3$ and $n = 5$. Temperature dependent spectrum (top), resonance frequency ν_0 (middle) and quality factor Q (bottom) in dependence of the temperature from $T = 1.4\,\mathrm{K}$ to $T = 10\,\mathrm{K}$ for $n = 3$ (left) and $n = 5$ (right).

Figure 7.4 shows a zoomed in temperature dependent spectrum as well as the resonance frequency and the quality factor in dependence of the temperature for the mode $n = 3$ and $n = 5$. The resonance frequencies ν_0 of the observed modes have two influencing factors leading to a shift in it, the temperature dependent change in the dielectric constant ϵ_1 of STO

and the temperature dependent change in the London penetration depth λ_L and therefore effective geometry of the Nb conductor.

For very low temperatures $T < 3.5\,\mathrm{K}$, the behavior of the superconductor should have no impact on the resonance frequency ν_0 as it is expected to be temperature independent in this range (see figure 2.1). The dielectric constant ϵ_1 of STO should be constant for $T < 3.5\,\mathrm{K}$ and therefore no shift in resonance frequency should be observed. For $n = 5$, this behavior is confirmed by the graph in figure 7.4 (middle, right side) as the resonance frequency stays constant. However, the mode $n = 3$ (middle, left side) shows a decrease in resonance frequency with increasing T for $T < 3.5\,\mathrm{K}$ and then again an increase starting with $T > 3\,\mathrm{K}$. Hence, a minimum in the resonance frequency and thus a maximum in the dielectric constant is observed there. This intriguing behavior was reported to be also observed in [26, 93]. The authors of [93] denote this behavior to the quantum criticality theory effects caused by the coupling of the order parameter field to acoustic phonons, called the electrostrictive effect.

For temperatures $T > 4\,\mathrm{K}$, the shift in ν_0 is impacted by the slight increase in penetration depth λ_L and the decrease of the dielectric constant ϵ_1 of the STO substrate. However, the decrease of the dielectric constant ϵ_1 and thus ϵ_{eff} dominates the resonance frequency shift and hence leads to an increase in ν_0 which can be seen for both modes in figure 7.4 (middle, right and left).

At temperatures very close to T_c, the resonance frequency shift is dominated by the transition of Nb from its superconducting to its non-superconducting state leading to a strong increase of the penetration depth and thus a decrease in resonance frequency. However, this is not observed but only indicated in this measurement because the temperature steps close to T_c were chosen to be not dense enough.

The quality factors both show the same behavior being maximum at the low temperatures and then decreasing with higher temperatures and leveling off at around 4.5 K. The maximal quality factor reached for mode $n = 3$ is $Q = 87$ and for $n = 5$ it is $Q = 172$. Going to very low temperatures, the behavior of both quality factor plots indicate a further increase of Q approaching absolute zero. As the impact of the superconductor is temperature independent in that temperature area, the strong increase of the quality factor is interpreted to occur because of decreasing dielectric losses in the STO substrate. This was also indicated by the results of the metallic resonator on STO in section 7.1. This indication and the high absolute values of Q especially for mode $n = 5$ are of great potential and interest for the dielectric loss properties of STO at mK-temperatures and to realize an LAO/STO resonator with given geometry which would operate at mK-temperatures. This is being addressed later on in section 7.2.1 of this thesis.

The dielectric constant ϵ_1 of STO is calculated with the values of the resonance frequency ν_0 by the same procedure as for the metallic resonator in section 7.1. Figure 7.5 shows dielectric constant ϵ_1 of all measured resonators on STO from this work and two other authors in comparison. The values obtained with the superconducting resonators match the low temperature values of the metallic resonator quite closely. The dielectric constant for the lowest temperature value of $T = 1.4\,\mathrm{K}$ is 19.7×10^3 and 20.9×10^3 for $n = 3$ and $n = 5$, respectively. The decreasing behavior starting at around $T \approx 4\,\mathrm{K}$ is shown by both modes. Inset (a) in figure 7.5 shows the inverse dielectric constant $1/\epsilon_1$ obtained with the metallic

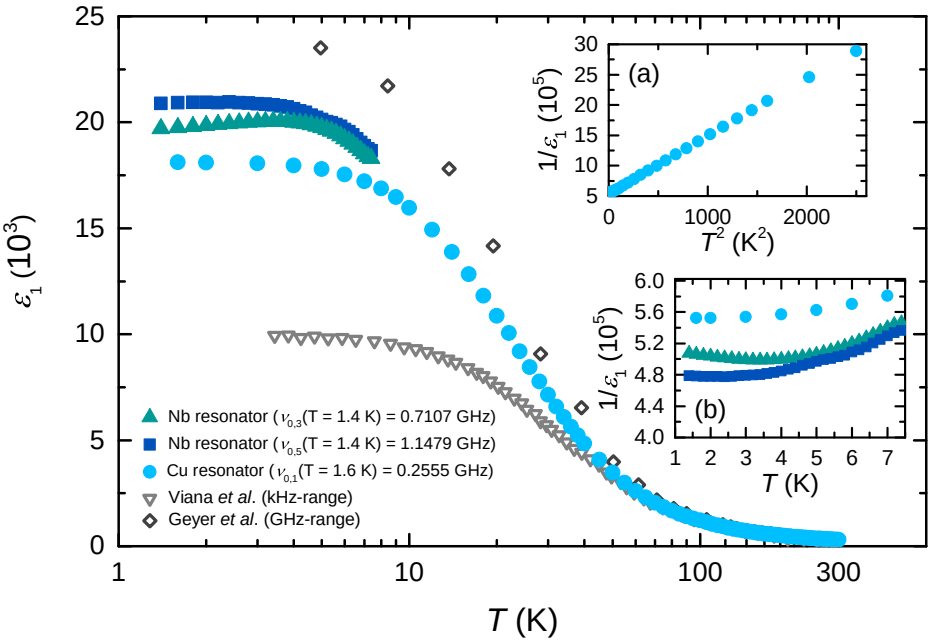

Fig. 7.5.: Dielectric constant ϵ_1 of all measured resonators on STO from this work and two other authors in comparison. Inset (a) shows the inverse dielectric constant $1/\epsilon_1$ in dependence of the quadratic temperature T^2. Inset (b) shows the inverse dielectric constant $1/\epsilon_1$ in dependence of the temperature T.

resonator in dependence of the quadratic temperature T^2 up to temperature values of around 50 K. The inverse dielectric constant does not show the classical high temperature Curie-Weiss law behavior in that area. It rather follows a non-classical T^2-dependence. This behavior can be explained by the ϕ^4-quantum field model [93]. This quantum criticality model in the self-consistent field approximation predicts a T^2-behavior of the inverse dielectric function $1/\epsilon_1$ on the border of displavice ferroelectric quantum phase transitions [93]. This is perfectly matched by the measured values of the metallic resonator on STO as depicted in inset (a). Inset (b) shows the inverse dielectric constant $1/\epsilon_1$ in dependence of the temperature $T < 7\,\mathrm{K}$ for all resonators. The data of the mode $n = 3$ of the Nb-resonator shows the anomalous upturn of $1/\epsilon_1$ towards lower T starting at around 3 K reported in [93] which the authors denote to the quantum criticality theory connecting the electric polarization field with the acoustic phonons called the electrostrictive effect [93].

To reproduce the observed results and to set denser temperature steps close to T_c allowing a quantitative analysis of the superconducting phase transition, the measurement was redone with the exact same resonator chip and feedline but with a completely redone mounting. Figure 7.6 shows the results of the mode with $n = 3$ for the remounted chip with denser temperature steps close to T_c.

The position of the resonance frequency ν_0 at $T = 1.4\,\mathrm{K}$ with the remounted and remeasured chip only varies about 2 % from the previous measurement showing the reproducibility of the measurement method. One has to note though, that the measurement strongly depends on the mounting of the chip as very small changes in the position or orientation and the

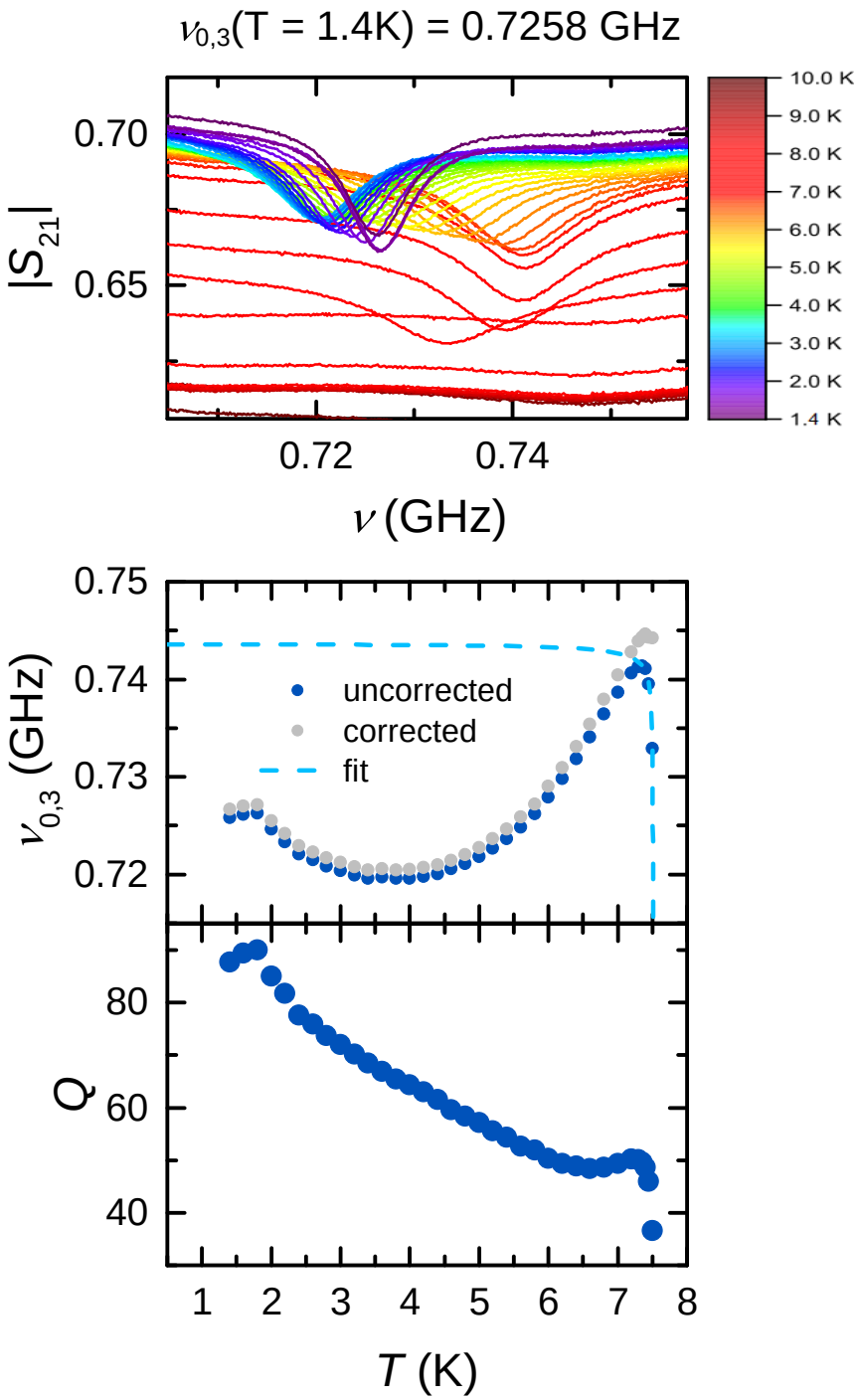

Fig. 7.6.: Analysis of mode $n = 3$ with the remounted resonator chip. Temperature dependent spectrum (top), resonance frequency ν_0 (middle) and quality factor Q (bottom) in dependence of the temperature from $T = 1.4\,\mathrm{K}$ to $T = 10\,\mathrm{K}$.

coupling parameter distance h of the resonator chip on top of the feedline leads to derivations in the intensity and position of the resonance frequencies and the quality factors. Making the mounting more reliable and reproducible would find a remedy to that problem.

In the new measurement, the downturn in resonance frequency close to T_c is now clearly visible. This is due to the change of the effective geometry of the superconductor when approaching T_c provoked by the divergent increase of the London penetration depth λ_L. The penetration depth shortens the effective geometry by $\lambda_L/2$ at every edge of the superconductor leading to a change of the characteristic impedance of the cpw [94]. The characteristic impedance directly changes the effective dielectric constant ϵ_{eff} according to equation (2.30), which changes the resonance frequency according to equation (2.17). This shifted resonance frequency can be described by

$$\nu_{0,\text{shifted}} = \frac{\nu_0}{\sqrt{1 + \frac{\Gamma}{2Z_0}\lambda_L(T)}} = \frac{\nu_0}{\sqrt{1 + \frac{\Gamma}{2Z_0}\frac{\lambda_L(0)}{\sqrt{1-\left(\frac{T}{T_c}\right)^4}}}} \tag{7.5}$$

with a geometrical factor Γ, the characteristic impedance Z_0 and the London penetration depth $\lambda_L(T)$ according to equation (2.14). Note, that this formula is only valid for values close to T_c.

A fit of this formula is performed to the resonance frequency values close to T_c in figure 7.6 (middle) and allows for a quantitative analysis of the superconducting properties of Nb and a correction of the resonance frequencies ν_0. The fit yields a penetration depth at $T = 0$ of $\lambda_L(0) = 69.1 \pm 30.9\,\text{nm}$ which is in reasonable agreement with the literature value of 39 nm [33], considering that the sputtered film has some impurities and is very thin compared to bulk samples which reach the literature value. The critical temperature obtained from the fit is $T_c = 7.51 \pm 0.02\,\text{K}$ very close to the measurement with the same chip before and with the SQUID magnetometer (see section 6.2.2).

The fit allows a correction of the resonance frequencies for the impacts of the superconductor. As depicted in figure 7.6, the corrected values are only slightly above the uncorrected values for all temperatures except for temperatures close to T_c which is as expected. The impact of the superconductor can therefore be neglected for temperatures far below T_c.

The absolute values as well as the behavior of the quality factor Q is also in good agreement with the previous measurement confirming the reproducibility. Very close to T_c, the quality values slightly decrease as the resonant modes broaden and decrease in amplitude before disappearing completely at T_c.

7.2.1. Resonator operation at mK-temperatures

The behavior of the quality factor Q and the anomalous upturn in resonance frequency ν_0 (indicated in figure 7.4) at very low temperatures are of immense interest not only for the operation of the LAO/STO resonator but also for the dielectric properties of STO. This gave rise to measure the superconducting resonator to even lower temperatures in the mK-range. These measurements were performed using a ^{3}He/^{4}He dilution refrigerator ranging down to a temperature of $T \approx 22\,\text{mK}$. The mounting of the resonator chip is the same as the second measurement of figure 7.6. Figure 7.7 shows the results of these measurements. For

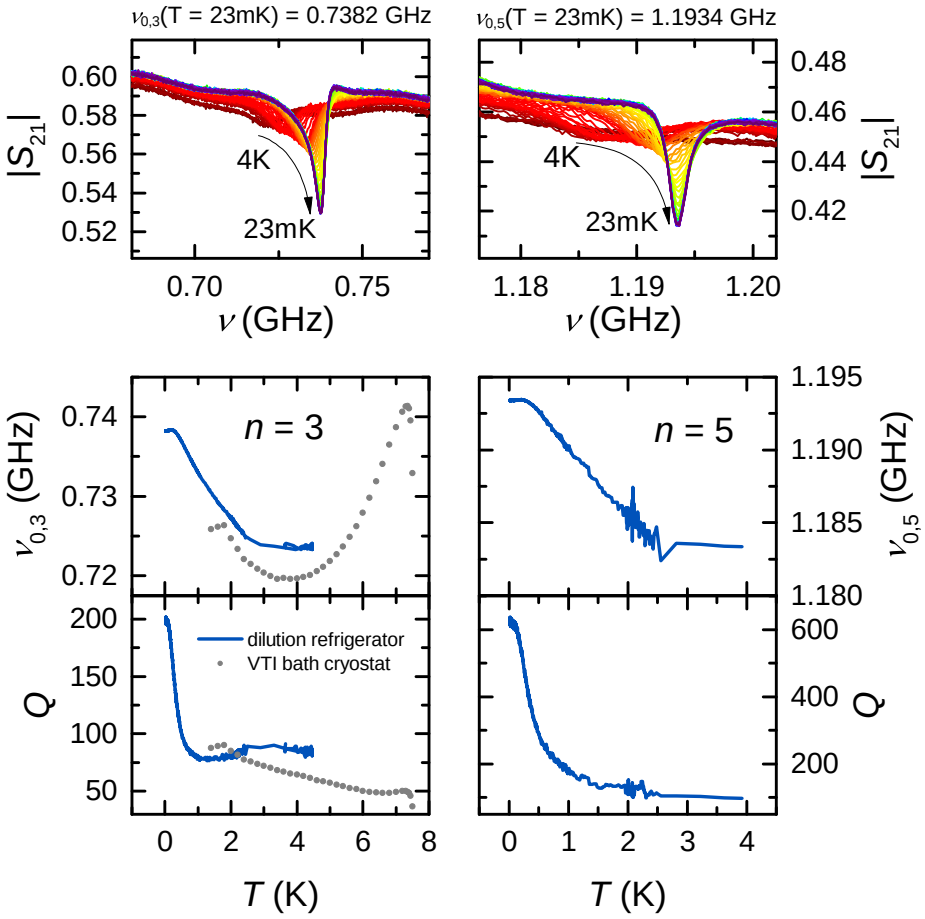

Fig. 7.7.: Analysis of the observed modes $n = 3$ and $n = 5$ in the dilution refrigerator. Temperature dependent spectrum (top), resonance frequency ν_0 (middle) and quality factor Q (bottom) in dependence of the temperature from $T = 23\,\mathrm{mK}$ to $T = 4\,\mathrm{K}$ for $n = 3$ (left) and $n = 5$ (right).

mode $n = 3$, the dilution refrigerator data connects consistently to the data of the VTI bath cryostat. The indicated and supposed increase of the quality factor can clearly be seen in the quality factor (bottom). At a temperature of $T \approx 500\,\mathrm{mK}$, the quality factor steeply rises to a value of around 200 and 600 for $n = 3$ and $n = 5$, respectively. This is of great potential to operate an LAO/STO resonator with the given flip chip geometry at mK-temperatures with a high quality factor Q. The rise of Q at such low temperatures $T < 1\,\mathrm{K}$, where the superconducting properties of Nb are temperature independent also indicates that the strong increase in the quality factor denotes to a substantial decrease of the dielectric losses ϵ_2 of STO at temperatures $T < 500\,\mathrm{mK}$. This could indicate a new phase or other unconventional and undiscovered property of the material STO that was not yet reported so far.

The anomalous upturn in resonance frequency at temperatures below $T \approx 3\,\mathrm{K}$ observed before is confirmed in this measurement, for $n = 5$ now as well. The resonance frequency increases even further up until a value of $T \approx 300\,\mathrm{mK}$. This would show the electrostrictive

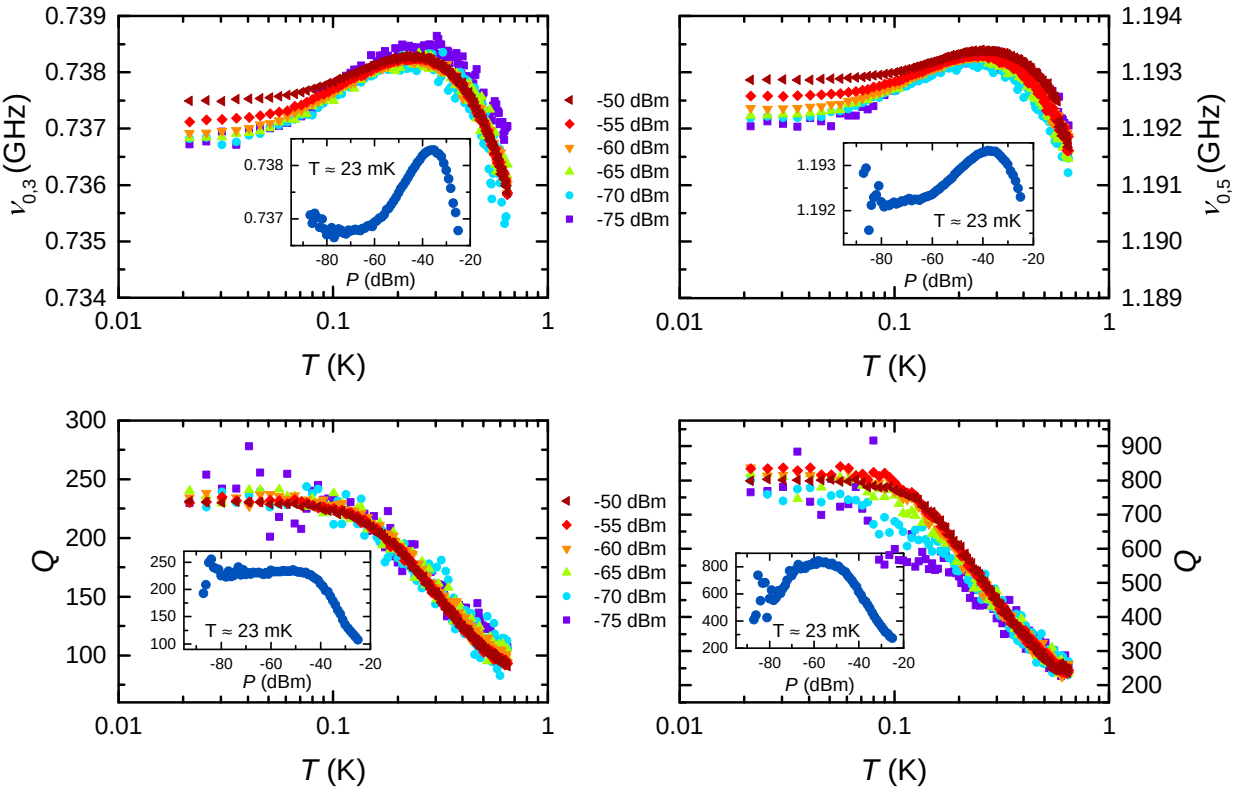

Fig. 7.8.: Power dependent measurements of the resonance frequency ν_0 (top) and quality factor Q (bottom) for $n = 3$ (left) and $n = 5$ (right) in dependence of the temperature for $T < 1\,\mathrm{K}$. The insets show the respective quantity in dependence of the power for a fixed temperature of $T = 23\,\mathrm{mK}$.

effect describing the coupling of the electric polarization field with the acoustic phonons suggested in [93].

Below 400 mK, the resonance frequency ν_0 shows a quite intriguing behavior saturating, then decreasing slightly and then leveling off at around 40 mK (see figure 7.8). The saturation is indicated by numerical calculations of the quantum criticality model from Rowley *et al.* [93] and shown in figure 7.9(d) but has not yet been measured.

In the interest of increasing the quality factor Q even further, the power of the used microwave signal was swept from $-75\,\mathrm{dBm}$ to $-50\,\mathrm{dBm}$. The power dependent measurements are depicted in figure 7.8. A power sweep at the constant temperature of $T = 23\,\mathrm{mK}$ indicated a maximal quality factor at around $-60\,\mathrm{dBm}$ (see insets). The maximum quality factor value of $Q = 840$ is found for a power of $P = -55\,\mathrm{dBm}$ at a temperature of $T = 56\,\mathrm{mK}$ with the $n = 5$ mode. The insets also show that the behavior of the temperature dependent resonance frequency shift is real and can be denoted to STO. When increasing the power P at a constant temperature of $T = 23\,\mathrm{mK}$ (insets), the sample eventually gets heated by the microwave measurement signal. The resonance frequency shift in this heating process shows the same behavior as for the temperature dependent measurement at fixed power. This can be confirmed by checking the value of the resonance frequency at a reference point e.g. in

the maximum at around $T \approx 300\,\mathrm{mK}$. The corresponding values of the maxima in the power dependent measurement (insets) show the same absolute values of ν_0 as in the temperature run. This is also confirmed for the quality factors Q. The behavior of the resonance frequency shift and the quality factor thus are real and induced by the material STO. The measurement data show, that starting with a power $P \approx -60\,\mathrm{dBm}$ to higher values, the microwave signal begins to heat the sample as these graphs differ from the graphs with a lower power signal that are all showing the same qualitative and quantitative behavior.

Figure 7.9 shows a comparison of the full temperature dependence of ϵ_1 of STO for the different experiments in this work and literature. The high temperature data (figure 7.9(a)) is obtained with the metallic Cu resonator and is in excellent agreement with data from [21, 22]. The classical Curie-Weiss-law is followed for temperature values down to $T \approx 50\,\mathrm{K}$. The inverse dielectric constant $1/\epsilon_1$ for temperature values $T < 50\,\mathrm{K}$ (figure 7.9(b)) satisfies a T^2-behavior predicted with the Φ^4-quantum field model in the quantum criticality theory described by Rowley *et al* [93]. The data obtained with the Cu resonator is in agreement with the measurement data from Rowley *et al.* showing a similar slope. Figure 7.9(c) and (d) show a comparison of the data obtained by the Nb resonator in figure (c) with the data from Rowley *et al.* in figure (d) from a measurement and calculations in the Φ^4-quantum field model. The calculations include the coupling of the order parameter field with acoustic phonons called the electrostrictive effect. The anomalous upturn in the inverse dielectric constant can be seen in the measured data of the Nb resonators (figure 7.9(c)). The saturation predicted by numerical calculations of Rowley *et al.* (figure 7.9(d)) are confirmed by the low temperature data obtained with the dilution refrigerator measurement.

Overall, the data of the dielectric properties of STO over the whole measured temperature range obtained with both the Cu and the Nb resonator fit well to existing theoretic models and to previously published literature, but they also reveal new phenomenology for the dielectric losses of STO.

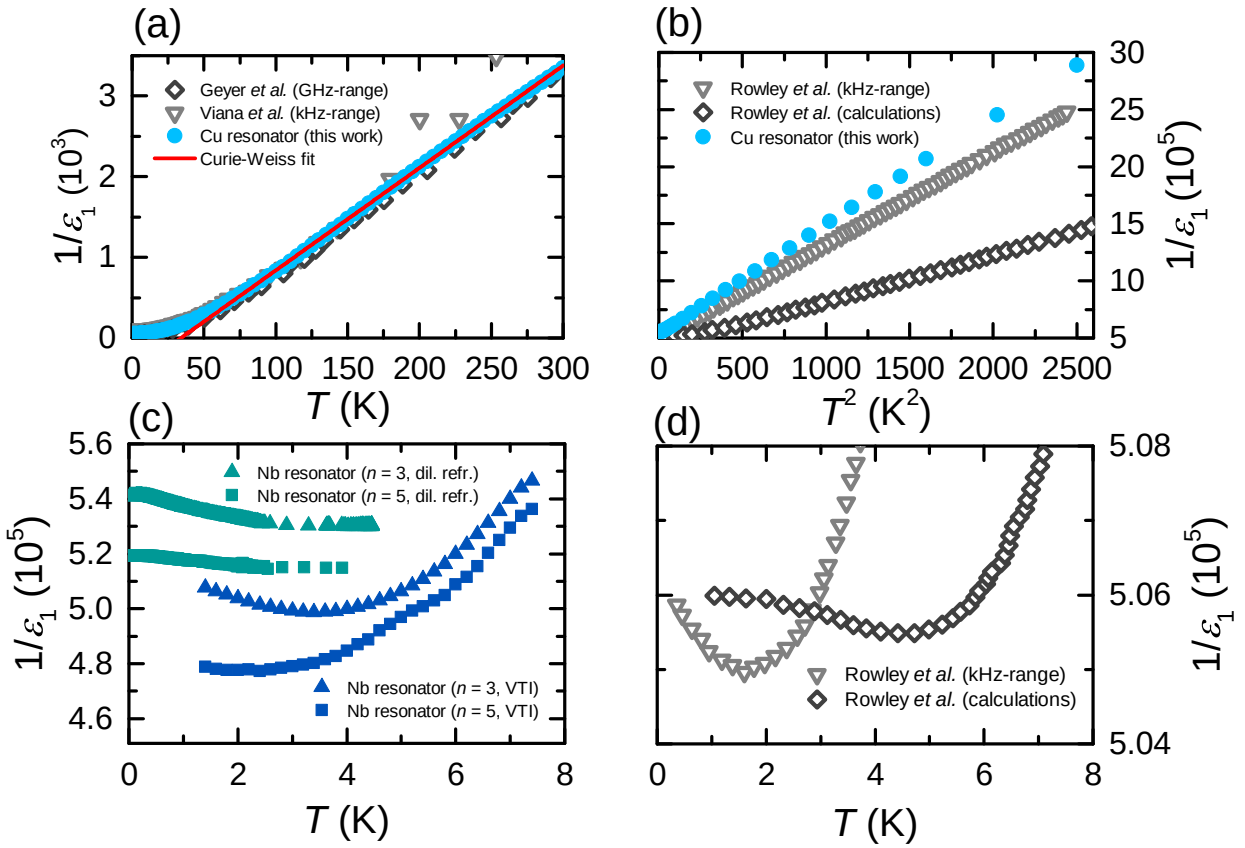

Fig. 7.9.: Comparison of the full temperature dependence of ϵ_1 of STO for the different experiments. (a) Inverse dielectric constant $1/\epsilon_1$ in dependence of the high temperature values up to $T = 300\,\mathrm{K}$ obtained with the Cu resonator and from [21, 22] with a Curie-Weiss-fit. (b) T^2-behavior of the inverse dielectric constant $1/\epsilon_1$ in dependence of the temperature for $T < 50\,\mathrm{K}$ obtained with the Cu resonator and from [93]. (c) Very low temperature data of the inverse dielectric constant $1/\epsilon_1$ obtained with the Nb resonator in the VTI bath cryostat (dark blue data points) and the dilution refrigerator (green data points) for $n = 3$ (triangles) and $n = 5$ (squares) showing an anomalous upturn. (d) Low temperature data from a measurement in the kHz-range and from numerical calculations by Rowley *et al.* [93].

8. Summary

This project addresses the realization of an LAO-resonator on the substrate STO to eventually give experimental access at GHz frequencies to the fascinating properties of the 2DEG formed in the LAO/STO interface. For that purpose, a new resonator geometry, which is a coplanar $\lambda/4$-resonator coupled inductively over a feedline using a distant flip-chip mounting, was developed. In a first step, this geometry was realized using the element superconductor Nb on the substrate STO. It can immediately be transferred to a gateable LAO/STO resonator to probe the interesting quantities of the 2DEG, e.g. the superfluid density, critical temperature or superconducting gap energy in dependence of the frequency, temperature and electrostatic gating by monitoring the resonance frequencies and microwave losses of the LAO/STO-resonator.

In finite element simulations, this resonator geometry was tested, showing that the resonance frequency ν_0 matches the analytical formula obtained with the conformal mapping theory. It was found to be in agreement with substrates of dielectric constants ϵ_1 up to very high values in the order of 10^4 and thus for STO in a temperature range down to mK-temperatures. The simulations allowed an optimization of the coupling strength of the resonator geometry with the two coupling parameters distance h of the resonator chip to the feedline and the coupling length l_c, which defines the parallel arm of the resonator above the feedline, even for a high dielectric constant $\epsilon_1 \approx 300$.

The superconducting resonator was realized in an experiment using the elemental superconductor Nb on an STO substrate while the feedline was fabricated on an Al_2O_3 substrate. The resonator is operating at frequencies exceeding 1 GHz, which is the highest frequency of a coplanar superconducting resonator device on STO published so far. The temperature dependence of the dielectric properties of lossy and high-ϵ STO governs the temperature dependence of the resonator performance and in this regard dominates over the superconducting influences of the Nb.

High temperature values of the dielectric constant ϵ_1 were tracked between 1.6 and 300 K using a conventional Cu $\lambda/2$-resonator, developed previously in my bachelor project [27]. The temperature dependent dielectric properties of both ϵ_1 and ϵ_2 are in agreement with previous works by other authors. The high temperature values of ϵ_1 satisfy a Curie-Weiss-behavior revealing a Curie-temperature of $T_C = 34$ K. Below $T \approx 50$ K, the temperature dependence follows a T^2-behavior predicted by the ϕ^4-quantum field model [93] for incipient ferroelectric quantum phase transitions in the self-consistent field approximation.

Experiments in the mK-temperature range revealed an anomalous upturn of $1/\epsilon_1$ towards lower T due to the coupling of the electric polarization field with acoustic phonons [93]. In addition to that, an abrupt increase in the quality factor Q up to values of 840 was observed below temperatures of $T \approx 1$ K. This indicates a strong drop in the dielectric losses ϵ_2 of the material STO and could refer to an unconventional property or phase of STO, not yet

discovered. The rise in the quality factor Q could be tuned up to values of $Q = 840$ by sweeping the input power P and is of enormous interest and potential for future mK-operation of superconducting STO resonators and the LAO/STO resonator.

9. Outlook

In this thesis, it was shown that it is possible to inductively couple a coplanar superconducting $\lambda/4$-resonator on the substrate STO via a superconducting feedline on an Al_2O_3 substrate. The coupling strength can be controlled via the coupling length l_c and the distance h. The coupling strength and thus the quality factor Q strongly depends on these two coupling parameters. Therefore, the success of the experiment strongly depends on the mounting of the resonator above the feedline. To improve the mounting procedure, microwave resonator boxes with removable side walls have been developed and realized (see figure A.1 in the appendix). These boxes enable experimental access to the resonator and feedline chip from the side and substantially facilitate the mounting procedure. Future experiments with these boxes can improve the accuracy and reliability of the adjustment of the distance h by using e.g. small insulating pillars or foils with known thicknesses. The functionality of these boxes was tested for a Cu chip at room temperature as depicted in figure A.3 in the appendix and shows the normal feedline spectrum as expected. Removing the side walls changes the frequency position of the boxmodes as the boundary conditions of the box change.

Furthermore, the results of this thesis pave the way for accessing the 2DEG in the LAO/STO interface using the developed flip-chip geometry for an LAO/STO resonator. These resonator chips were recently fabricated and the respective LAO/STO interfaces were tested to be superconducting below temperatures of $T \approx 250\,\mathrm{mK}$. Figure B.1 in the appendix shows a microscope image of one fabricated LAO/STO chip with three resonator structures of different lengths l (right side) and contacts for gating (left side). With these resonators, it is possible to probe the interesting quantities of the 2DEG, e.g. the superfluid density, critical temperature or superconducting gap energy in dependence of the frequency, temperature and electrostatic gating by monitoring the resonance frequencies of the resonator.

It is of high interest to increase the accessible frequency range to higher values not only for the fundamental properties of the superconducting dome (directly measure the superconducting gap energy), but also for new device applications e.g. qubits which operate in the microwave frequency range. The highest frequency value of published LAO/STO devices could be increased by a factor of around 3 but it is very appealing to further expand this frequency area to even higher values. This could be addressed in future experiments e.g. by shortening the resonator length l.

A. Microwave resonator boxes with removable side walls

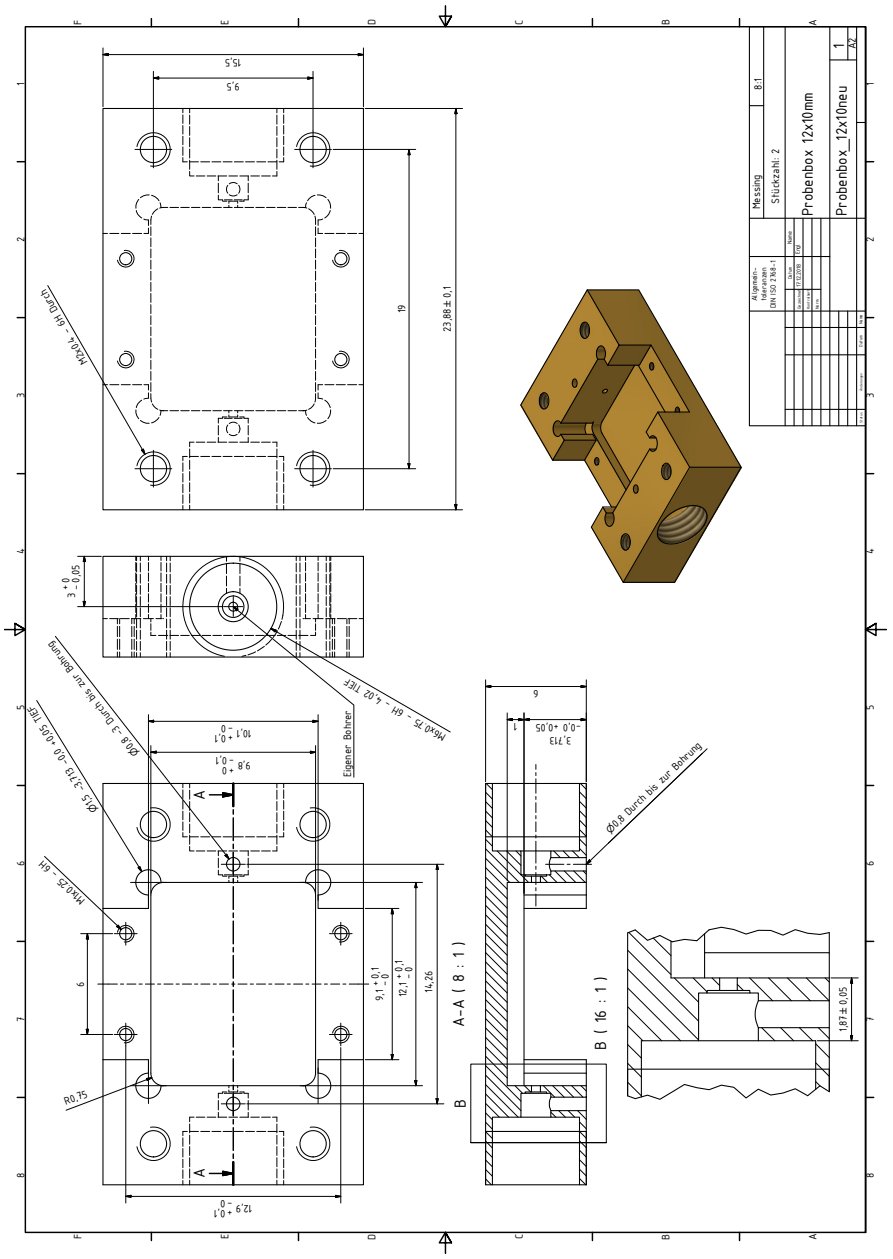

Fig. A.1.: Mechanical drawing of the microwave resonator box with removable side walls.

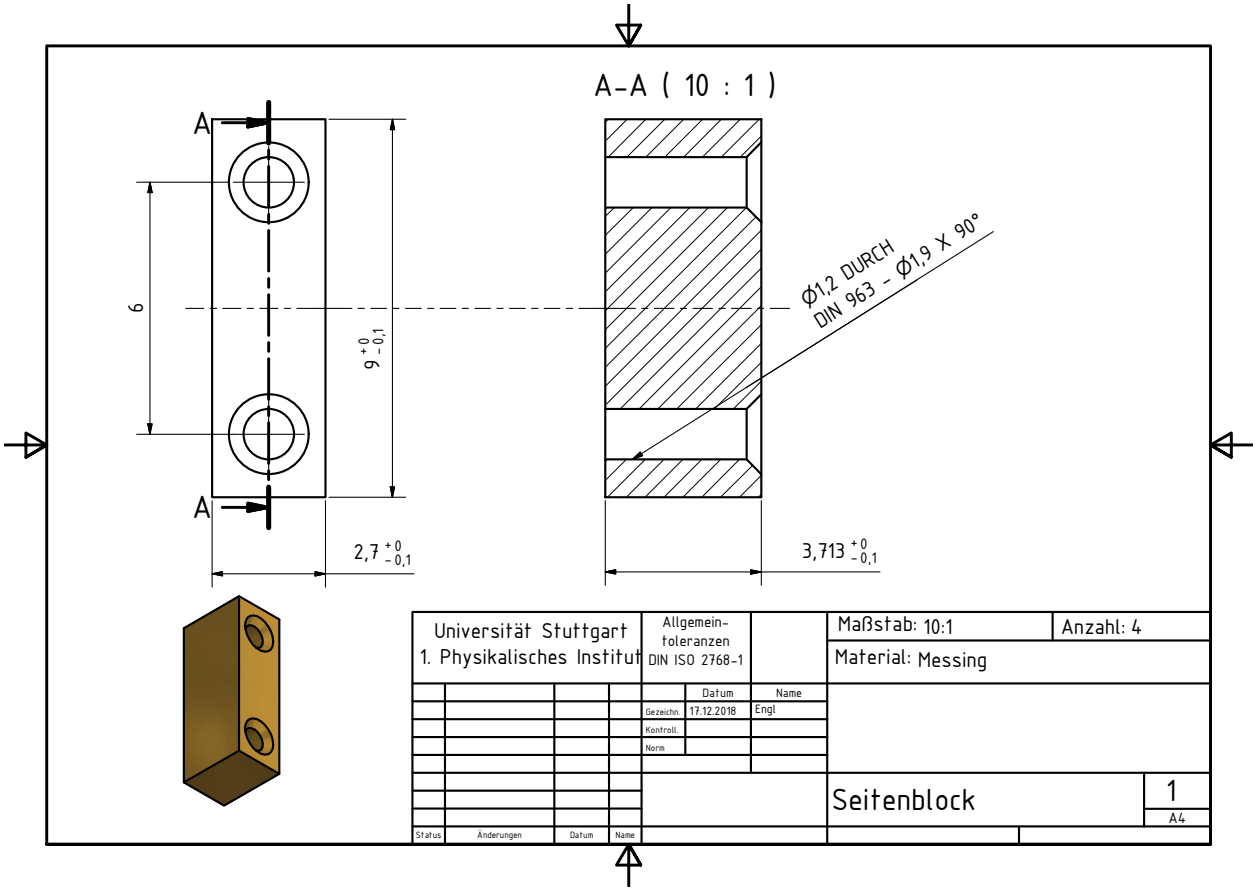

Fig. A.2.: Mechanical drawing of the removable side wall.

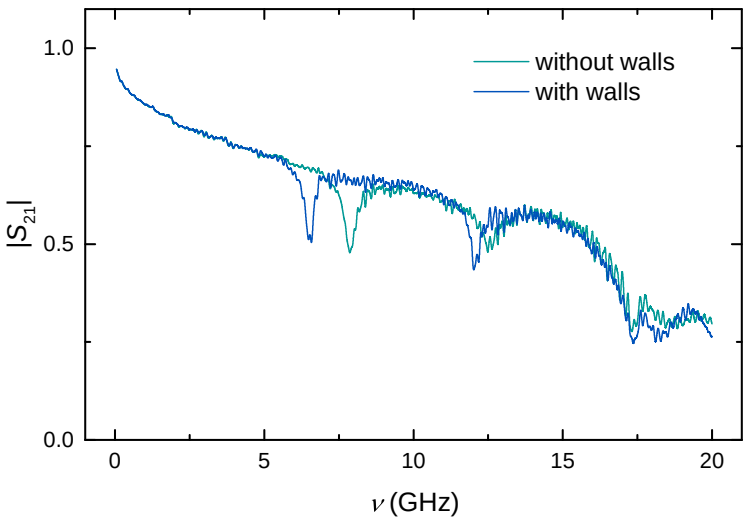

Fig. A.3.: Transmission spectrum of a coplanar Cu-feedline placed in the newly designed boxes with and without side walls ($P = -20\,\mathrm{dBm}$).

B. LAO/STO resoantor

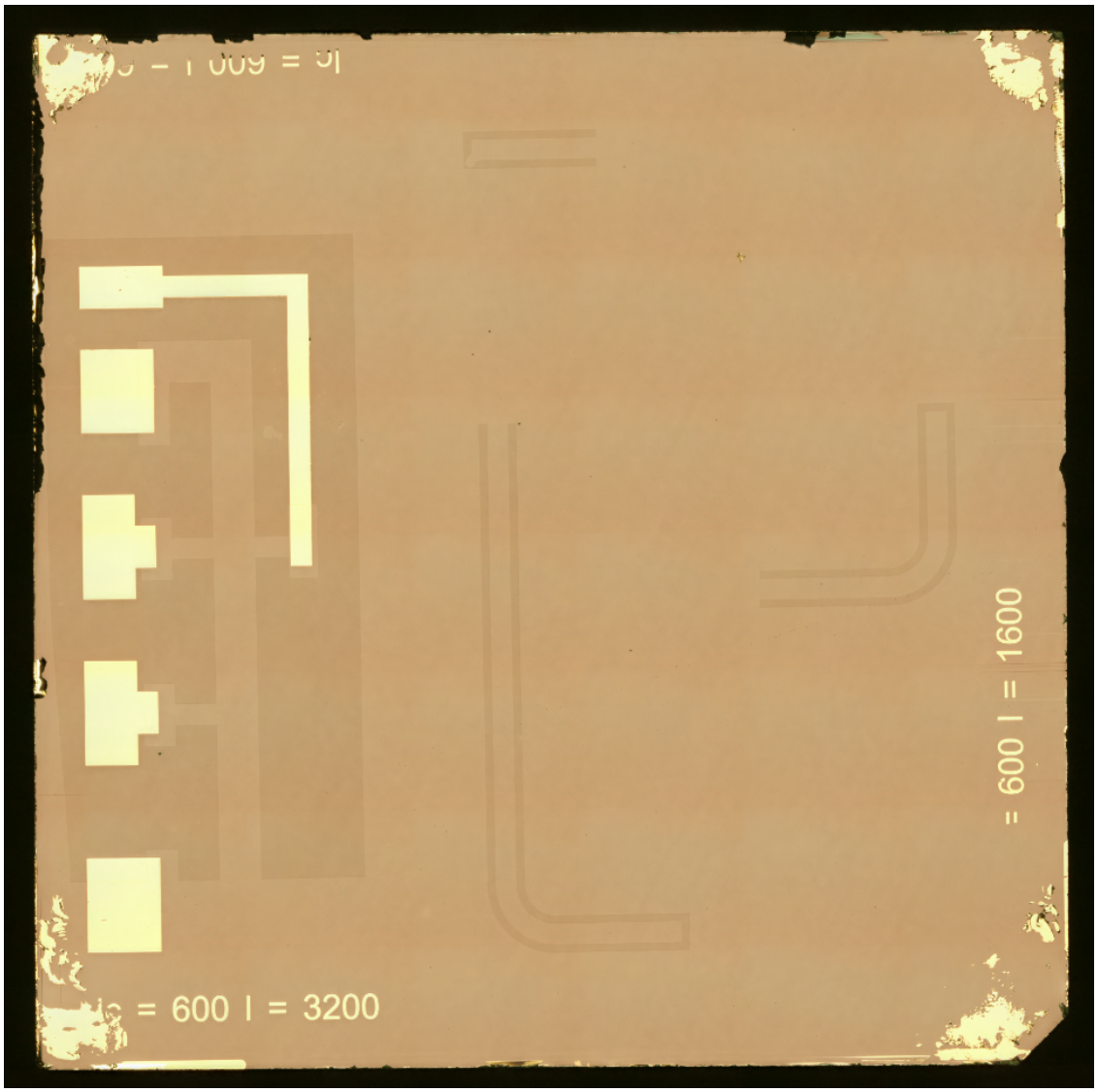

Fig. B.1.: Microscope image of the fabricated LAO/STO chip with three resonator arms of different lengths l and a structure for Hall measurements and the gating procedure on the left side of the chip.

Acknowledgments

I want to thank everyone who helped me writing this master thesis, especially:

- Prof. Dr. Martin Dressel for letting me perform this project at PI1.
- Prof. Dr. Jürgen Weis for being my second examiner.
- Dr. Marc Scheffler for being my supervisor, for giving me all the support in his high frequency group at PI1 since my bachelor project and for useful discussions.
- Nikolaj Ebensperger for being my direct supervisor, for all the help with both experimental or theoretical questions, for all the fun we had while working on this project and for the help with the dilution refrigerator.
- Lars Wendel and Christoph Müller for everything.
- Gabriele Untereiner for all the sample preparation and for experimental discussions.
- Ahmed Farag and Monika Ubl for the fabrication of the Nb resonators and feedlines.
- Prof. Dr. Jochen Mannhart and Dr. Hans Boschker for the fabrication of the LAO/STO resonators and for useful discussions.
- Mario Zinßer for all the help especially in the early stages of this project.
- Alessandro D'Arnese for the help with *Autodesk Inventor*.
- Dr. Markus Thiemann, Björn Miksch and Dr. Guilherme Gorgen Lesseux for the help in the lab and for useful discussions.
- Manfred Beutel for preceding work on this project.
- the low temperature department for the constant supply with liquid helium and nitrogen.
- the mechanical workshop for the fabrication of the microwave resonator boxes.
- the whole PI1 for the nice working atmosphere.
- my family and friends for supporting me throughout all the studies leading up to this thesis.

Deutsche Zusammenfassung

Oxid-Grenzflächen sind ein faszinierendes und hochaktuelles Forschungsgebiet in der Festkörperphysik, das sich vor allem durch die jüngsten Fortschritte in der Dünnfilmtechnik weiterentwickeln konnte. Diese Grenzflächen können eine Vielzahl an besonderen und unkonventionellen elektronischen Eigenschaften und Phasen wie z.B. Supraleitung, Ferroelektrizität oder Magnetismus aufweisen, die nicht in den jeweiligen separaten Ausgangsmaterialien auftreten. Darüber hinaus beinhaltet das Forschungsgebiet noch einige bisher ungeklärte Fragen. Antworten auf diese Fragen sind von großem Interesse, nicht nur für die Grundlagenforschung, sondern auch für potentielle zukünftige Anwendungen.

Ein Beispiel für ein solches Oxid-Interface ist das, welches sich zwischen den beiden Isolatoren $LaAlO_3$ (LAO) und $SrTiO_3$ (STO) befindet, das sogenannte LAO/STO-Interface. In diesem Interface bildet sich ein zweidimensionales Elektronengas (2DEG) aus, welches leitende Eigenschaften besitzt, obwohl die Materialien LAO und STO separat Isolatoren sind. Die Gründe für das Auftreten des 2DEG sind noch nicht abschließend erforscht. Außerdem wurde in diesem 2DEG auch 2D-Supraleitung mit einer kritischen Temperatur $T_c = 200\,\mathrm{mK}$ entdeckt. Diese Supraleitung ist für den Fall, dass kein extern angelegtes, elektrisches Feld existiert, im Einklang mit der BCS-Theorie. Mit einem extern angelegten E-Feld jedoch lassen sich sowohl die kritische Temperatur als auch die suprafluide Dichte durchstimmen. Dies zeigt eine kuppelförmige Abhängigkeit dieser Größen von der Ladunsträgerdichte n im Interface, die es erlaubt, einen Supraleiter-Isolator-Übergang herbeizuführen. Die Leitfähigkeit im normalleitenden Zustand ist ebenfalls kontrollierbar, was einen Metall-Isolator-Übergang ermöglicht. Neben diesen faszinierenden Eigenschaften wurden im LAO/STO-Interface auch Ferromagnetismus, ein großer negativer Magnetowiderstand und starke Spin-Bahn-Kopplung beobachtet.

Die Nutzung von planaren Mikrowellenresonatoren ist eine etablierte Methode, um die elektromagnetischen Eigenschaften von sowohl dicken als auch ultradünnen Proben bei GHz-Frequenzen zu untersuchen, da sie direkten experimentellen Zugang zu diesen erlauben. Das Material STO erschwert dieses Vorgehen allerdings immens. STO hat eine sehr hohe, anisotrope und temperaturabhängige, dielektrische Konstante ϵ_1 mit Werten von ca. 300 bei Raumtemperatur und in der Größenordnung von ca. 10^4 bei sehr niedrigen Temperaturen. Weiterhin sind die dielektrischen Verluste ϵ_2 auch viel höher als die von üblichen Resonator-Substraten wie z.B. Saphir. Dies führt dazu, dass es von enormer Schwierigkeit ist, die charakteristische Impedanz Z_0 des Wellenleiters auf den Koaxialkabelstandard von $50\,\Omega$ anzupassen. In vorangehenden Arbeiten wurde jedoch gezeigt, dass es sowohl prinzipiell als auch experimentell möglich ist, einen Resonator auf STO, aber auch einen LAO/STO-Resonator zu realisieren. Die höchste Frequenz von bisher veröffentlichten LAO/STO-Resonatoren reicht jedoch nicht über $\nu \approx 400\,\mathrm{MHz}$ hinaus und gleichzeitig werden nur niedrige Werte in der Güte Q erreicht. Für eine direkte Messung der supraleitenden Bandlücke Δ und

für neue Quantenapplikationen wie z.B. Qubits, welche im Mikrowellenbereich operieren, ist es von großer Bedeutung, den erreichbaren Frequenzbereich von LAO/STO-Resonatoren zu höheren Frequenzen zu erweitern.

Das Ziel dieser Arbeit ist es, einen supraleitenden Resonator auf STO mit einem bekannten Supraleiter wie z.B. Nb zu realisieren. Dies ist nötig, um zu sehen, ob diese Resonatomethode generell für Anwendungen wie LAO/STO möglich ist und, um einige Resonatorgrößen wie beispielsweise die Güte zu messen. Die Funktion planarer metallischer Resonatoren auf STO bis hinab zu einer Temperatur von 15 K wurde bereits in meinem Bachelorprojekt aufgezeigt. Der darauf aufbauende supraleitende Resonator soll so konzipiert sein, dass er sofort zu einem LAO/STO-Resonator, an dem eine Gatespannung anlegbar ist, transferiert werden kann. Dies geschieht, indem die supraleitende Schicht auf dem STO-Substrat durch einen Dünnfilm aus LAO ersetzt wird und so das 2DEG im LAO/STO-Interface den Resonator bildet.

Im Hinblick auf dieses Ziel wurde im Rahmen dieser Arbeit eine neue Resonatorgeometrie entwickelt: Ein koplanarer $\lambda/4$-Resonator, welcher mittels einer Distanz-Flip-Chip-Montage induktiv aus der Ebene an eine Feedline gekoppelt wird. Dieser Resonator wurde mit dem Element-Supraleiter Nb auf einem STO-Substrat realisiert. Die Resonatorgeometrie kann sofort auf einen LAO/STO-Resonator übertragen werden, indem man den supraleitenden Dünnfilm durch einen ultradünnen LAO-Film ersetzt. Mit diesem Resonator lassen sich die interessanten physikalischen Größen des 2DEG, wie z.B. die suprafluide Dichte, die kritische Temperatur oder die supraleitende Energielücke in Abhängigkeit der Frequenz, der Temperatur und der externen Gatespannung messen, indem man die Verschiebung der Resonanzfrequenzen erfasst.

In Computersimulationen wurde die Resonatorgeometrie zunächst auf ihre Funktion getestet. Es zeigte sich, dass die Werte der simulierten Resonanzfrequenzen die analytische Formel der Theorie der konformen Abbildungen erfüllen. Somit wurde die Funktion der Resonatorgeometrie für dielektrische Substrate bis zu einer sehr hohen dielektrischen Konstante $\epsilon_1 = 10^4$, also für STO in einem Temperaturbereich bis mK-Temperaturen, bestätigt. Die Simulationen erlaubten auch eine Optimierung der beiden Kopplungsparameter Abstand h und Kopplungslänge l_c für eine hohe dielektrische Konstante $\epsilon_1 = 300$. h beschreibt den Abstand des umgedrehtem Resonatorchips zum darunter befindlichen Feedlinechip und die Kopplungslänge l_c beschreibt die Länge des parallelen Arms des Resonators über der Feedline.

Der supraleitende Resonator wurde im Experiment mit einem 300 nm-Dünnfilm aus Nb auf einem 200 µm dicken STO-Substrat realisiert. Die Feedline wurde ebenfalls mit einem Nb-Leiter auf einem 430 µm dicken Saphir-Substrat gefertigt. Der Resonator arbeitet bei Frequenzen, die größer als 1 GHz sein können. Das ist die höchste Frequenz eines koplanaren, supraleitenden Resonators auf dem Material STO, welcher bisher veröffentlicht wurde. Die Temperaturabhängigkeit der Resonator-Performance wird hierbei durch die Temperaturabhängigkeit der dielektrischen Eigenschaften von STO dominiert.

Die Hochtemperaturwerte der dielektrischen Konstante ϵ_1 und der dielektrischen Verluste ϵ_2 wurden mit einem konventionellen, metallischen $\lambda/2$-Resonator aus Cu aufgenommen. Die dielektrische Konstante als Funktion der Temperatur ist mit dem Curie-Weiss-Gesetz von Raumtemperatur bis hin zu einer Temperatur von ca. 50 K in Einklang und ergibt eine Curie-Temperatur von $T_\mathrm{C} \approx 34\,\mathrm{K}$. Beide dielektrischen Größen passen zu vorherigen Veröffentlichungen anderer Autoren. Für $T < 50\,\mathrm{K}$ folgt die inverse dielektrische Konstante

$1/\epsilon_1$ einem T^2-Verhalten, was durch das Φ^4-Quantenmodell für ferroelektrische Quanten-Phasenübergänge vorausgesagt wird.

Experimente im mK-Temperaturbereich haben einen anomalen Anstieg der inversen Dielektrizitätskonstante für sehr niedrige Temperaturen gezeigt. Dieser Anstieg wurde bisher kaum untersucht. Er ist mit der Kopplung des elektrischen Polarisationsfeldes mit akustischen Phononen, dem elektrostriktiven Effekt, zu erklären. Darüber hinaus wurde ein extremer Anstieg der Güte Q bei mK-Temperaturen beobachtet, welcher auf einen starken Abfall der dielektrischen Verluste im Material STO hindeutet. Dies könnte auf eine unkonventionelle und bisher unentdeckte Eigenschaft oder Phase in STO hindeuten. Durch Anpassung der Mikrowellenleistung konnte ein maximaler Wert der Güte von 840 erreicht werden.

Die Ergebnisse dieser Arbeit ebnen den Weg, mit der entwickelten Distanz-Flip-Chip-Resonatorgeometrie die interessanten Eigenschaften des 2DEG im LAO/STO-Interface zu erforschen. Die entsprechenden LAO/STO-Resonator-Chips wurden kürzlich angefertigt und können analog zu den Experimenten dieser Arbeit untersucht werden.

Eigenständigkeitserklärung

Ich versichere hiermit, dass ich die vorliegende Arbeit selbständig verfasst habe. Es wurden keine anderen als die angegebenen Quellen benutzt und alle wörtlich oder sinngemäß aus anderen Werken übernommenen Aussagen als solche gekennzeichnet. Diese Arbeit wurde weder vollständig, noch in wesentlichen Teilen in einem anderen Prüfungsverfahren verwendet und weder vollständig noch in Teilen bereits veröffentlicht. Der Inhalt des elektronischen Exemplars stimmt mit dem des Druckexemplars überein.

Stuttgart, den 09. April 2019

References

[1] H. Y. Hwang, Y. Iwasa, M. Kawasaki, Keimer, N. Nagaosa, and Y. Tokura, *Nat. Mater.* **11**, 103 (2012).

[2] J. Chakhalian, A. J. Millis, and J. Rondinelli, *Nat. Mater.* **11**, 92 (2012).

[3] A. Ohtomo and H. Y. Hwang, *Nature* **427**, 423 (2004).

[4] M. Huijben, A. Brinkman, G. Koster, G. Rijnders, H. Hilgenkamp, and D. H. A. Blank, *Adv. Mater.* **21**, 1665 (2009).

[5] N. Reyren, S. Thiel, A. D. Caviglia, L. F. Kourkoutis, G. Hammerl, C. Richter, C. W. Schneider, T. Kopp, A.-S. Rüetschi, D. Jaccard, M. Gabay, D. A. Muller, J.-M. Triscone, and J. Mannhart, *Science* **317**, 1196 (2007).

[6] C. Richter, H. Boschker, W. Dietsche, E. Fillis-Tsirakis, R. Jany, F. Loder, L. F. Kourkoutis, D. A. Muller, J. R. Kirtley, C. W. Schneider, and J. Mannhart, *Nature* **502**, 528 (2013).

[7] N. Manca, D. Bothner, A. M. R. V. L. Monteiro, D. Davidovikj, Y. G. Saglam, M. Jenkins, M. Gabay, G. Steele, and A. D. Caviglia, *Phys. Rev. Lett.* **122**, 036801 (2019).

[8] A. D. Caviglia, S. Gariglio, N. Reyren, D. Jaccard, T. Schneider, M. Gabay, S. Thiel, G. Hammerl, J. Mannhart, and J.-M. Triscone, *Nature* **456**, 624 (2008).

[9] C. Bell, S. Harashima, Y. Kozuka, M. Kim, B. G. Kim, Y. Hikita, and H. Y. Hwang, *Phys. Rev. Lett.* **103**, 226802 (2009).

[10] S. Thiel, G. Hammerl, A. Schmehl, C. W. Schneider, and J. Mannhart, *Science* **313**, 1942 (2006).

[11] J. A. Bert, B. Kalisky, C. Bell, M. Kim, Y. Hikita, H. Y. Hwang, and K. A. Moler, *Nat. Phys.* **7**, 767 (2011).

[12] L. Li, C. Richter, J. Mannhart, and R. C. Ashoori, *Nat. Phys.* **7**, 762 (2011).

[13] M. B. Shalom, M. Sachs, D. Rakhmilevitch, A. Palevski, and Y. Dagan, *Phys. Rev. Lett.* **104**, 126802 (2010).

[14] A. D. Caviglia, M. Gabay, S. Gariglio, N. Reyren, C. Cancellieri, and J.-M. Triscone, *Phys. Rev. Lett.* **104**, 126803 (2010).

[15] M. S. DiIorio, A. C. Anderson, and B. Y. Tsaur, *Phys. Rev. B* **38**, 7019 (1988).

[16] M. Göppl, A. Fragner, M. Baur, R. Bianchetti, S. Filipp, J. M. Fink, P. J. Leek, G. Puebla, L. Steffen, and A. Wallraff, *J. Appl. Phys.* **104**, 113904 (2008).

[17] M. Scheffler, K. Schlegel, C. Clauss, D. Hafner, C. Fella, M. Dressel, M. Jourdan, J. Sichelschmidt, C. Krellner, C. Geibel, and F. Steglich, *Phys. Status Solidi B* **250**, 439 (2013).

[18] D. S. Rausch, M. Thiemann, M. Dressel, D. Bothner, D. Koelle, R. Kleiner, and M. Scheffler, *J. Phys. D* **51**, 465301 (2018).

[19] D. Hafner, M. Dressel, and M. Scheffler, *Rev. Sci. Instrum.* **85**, 014702 (2014).

[20] K. A. Müller and H. Burkard, *Phys. Rev. B* **19**, 7 (1979).

[21] R. Viana, P. Lunkenheimer, J. Hemberger, R. Bohmer, and A. Loidl, *Phys. Rev. B* **50**, 601 (1994).

[22] R. G. Geyer, B. Riddle, J. Krupka, and L. A. Boatner, *J. Appl. Phys.* **97**, 104111 (2005).

[23] D. G. Blair and I. N. Evans, *J. Phys. D* **15**, 1651 (1982).

[24] V. Braginsky and V. Panov, *IEEE Trans. Magn.* **15**, 30 (1979).

[25] D. Davidovikj, N. Manca, H. S. J. van der Zant, A. D. Caviglia, and G. A. Steele, *Phys. Rev. B* **95**, 214513 (2017).

[26] M. Beutel, "Microwave spectroscopy meets $SrTiO_3$: development of resonators with very high dielectric constant and investigation of superconducting properties at mK temperatures", Master thesis (University of Stuttgart, 2016).

[27] V. Engl, "Temperaturabhängige Mikrowellenmessungen an $SrTiO_3$ mittels metallischer Resonatoren", Bachelor thesis (University of Stuttgart, 2016).

[28] G. Singh, A. Jouan, L. Benfatto, F. Couëdo, P. Kumar, A. Dogra, R. C. Budhani, S. Caprara, M. Grilli, E. Lesne, A. Barthélémy, M. Bibes, C. Feuillet-Palma, J. Lesueur, and N. Bergeal, *Nat. Commun.* **9**, 407 (2018).

[29] A. Wallraff, D. I. Schuster, A. Blais, L. Frunzio, R.-S. Huang, J. Majer, S. Kumar, S. M. Girvin, and R. J. Schoelkopf, *Nature* **431**, 162 (2004).

[30] J. C. Maxwell, *Philos. Trans. Roy. Soc. London* **155**, 459 (1865).

[31] M. Dressel and G. Grüner, *Electrodynamics of solids: optical properties of electrons in matter* (Cambridge University Press, 2011).

[32] S. Hunklinger, *Festkörperphysik* (Oldenbourg Wissenschaftsverlag GmbH, 2009).

[33] C. Kittel, *Introduction to solid state physics* (John Wiley & Sons, Inc., 2004).

[34] F. London and H. London, *Proc. Roy. Soc. A* **149**, 71 (1935).

[35] J. E. Hirsch, *Phys. Rev. B* **69**, 214515 (2004).

[36] M. Tinkham, *Introduction to superconductivity* (Dover Publications, 2004).

[37] J. Bardeen, L. N. Cooper, and J. R. Schrieffer, *Phys. Rev.* **108**, 1175 (1957).

[38] T. Wollandt, M. Thiemann, M. Dressel, and M. Scheffler, *J. Phys.: Conf. Ser.* **969**, 012082 (2018).

[39] Y. Wiemann, J. Simmendinger, C. Clauss, L. Bogani, D. Bothner, D. Koelle, R. Kleiner, M. Dressel, and M. Scheffler, *Appl. Phys. Lett.* **106**, 193505 (2015).

[40] M. Thiemann, M. Dressel, and M. Scheffler, *Phys. Rev. B* **97**, 214516 (2018).

[41] N. G. Ebensperger, M. Thiemann, M. Dressel, and M. Scheffler, *Supercond. Sci. Technol.* **29**, 115004 (2016).

[42] M. Javaheri Rahim, T. Lehleiter, D. Bothner, C. Krellner, D. Koelle, R. Kleiner, M. Dressel, and M. Scheffler, *J. Phys. D* **49**, 395501 (2016).

[43] L. Bondorf, M. Beutel, M. Thiemann, M. Dressel, D. Bothner, J. Sichelschmidt, K. Kliemt, C. Krellner, and M. Scheffler, *Physica B* **536**, 331 (2018).

[44] C. Clauss, D. Bothner, D. Koelle, R. Kleiner, L. Bogani, M. Scheffler, and M. Dressel, *Appl. Phys. Lett.* **102**, 162601 (2013).

[45] N. Ebensperger, "Dielectric properties on the insulating side of the superconductor-insulator transition", Master thesis (University of Stuttgart, 2017).

[46] R. Gupta, L. Rana, A. Sharma, A. P. Freundorfer, M. Sayer, M. Tomar, and V. Gupta, *Ferroelectrics* **515**, 8 (2017).

[47] D. M. Pozar, *Microwave engineering* (John Wiley & Sons, Inc., 2011).

[48] R. N. Simons, *Coplanar waveguide circuits, components, and systems* (Wiley-IEEE Press, 2001).

[49] G. Ghione and C. U. Naldi, *IEEE Trans. Microw. Theory Tech.* **35**, 260 (1987).

[50] S. Gevorgian, L. J. P. Linnér, and E. L. Kollberg, *IEEE Trans. Microw. Theory Tech.* **43**, 772 (1995).

[51] A. Caviglia, "Two-dimensional electron gas in functional oxide interfaces", PhD thesis (University of Geneva, 2010).

[52] K. van Benthem, C. Elsässer, and R. H. French, *J. Appl. Phys.* **90**, 6156 (2001).

[53] M. Cardona, *Phys. Rev.* **140**, A651 (1965).

[54] R. C. Neville, B. Hoeneisen, and C. A. Mead, *J. Appl. Phys.* **43**, 2124 (1972).

[55] R. D. Leapman, L. A. Grunes, and P. L. Fejes, *Phys. Rev. B* **26**, 614 (1982).

[56] A. C. L. S. Marques, "Advanced Si pad detector development and $SrTiO_3$ studies by emission channeling and hyperfine interaction experiments", PhD thesis (University of Lisbon, 2009).

[57] T. Sakudo and H. Unoki, *Phys. Rev. Lett.* **26**, 851 (1971).

[58] G. Shirane and Y. Yamada, *Phys. Rev.* **177**, 858 (1969).

[59] F. W. Lytle, *J. Appl. Phys.* **35**, 2212 (1964).

[60] R. A. Cowley, *Phys. Rev. Lett.* **9**, 159 (1962).

[61] P. A. Fleury and J. M. Worlock, *Phys. Rev.* **174**, 613 (1968).

[62] M. Itoh, R. Wang, Y. Inaguma, T. Yamaguchi, Y.-J. Shan, and T. Nakamura, *Phys. Rev. Lett.* **82**, 3540 (1999).

[63] H. W. Jang, A. Kumar, S. Denev, M. D. Biegalski, P. Maksymovych, C. W. Bark, C. T. Nelson, C. M. Folkman, S. H. Baek, N. Balke, C. M. Brooks, D. A. Tenne, D. G. Schlom, L. Q. Chen, X. Q. Pan, S. V. Kalinin, V. Gopalan, and C. B. Eom, *Phys. Rev. Lett.* **104**, 197601 (2010).

[64] J. H. Haeni, P. Irvin, W. Chang, R. Uecker, P. Reiche, Y. L. Li, S. Choudhury, W. Tian, M. E. Hawley, B. Craigo, A. K. Tagantsev, X. Q. Pan, S. K. Streiffer, L. Q. Chen, S. W. Kirchoefer, J. Levy, and D. G. Schlom, *Nature* **430**, 758 (2004).

[65] M. D. Biegalski, Y. Jia, D. G. Schlom, S. Trolier-McKinstry, S. K. Streiffer, V. Sherman, R. Uecker, and P. Reiche, *Appl. Phys. Lett.* **88**, 192907 (2006).

[66] M. Scheffler, M. M. Felger, M. Thiemann, D. Hafner, K. Schlegel, M. Dressel, K. S. Ilin, M. Siegel, S. Seiro, C. Geibel, and F. Steglich, *Acta IMEKO* **4**, 47 (2015).

[67] M. Thiemann, M. H. Beutel, M. Dressel, N. R. Lee-Hone, D. M. Broun, E. Fillis-Tsirakis, H. Boschker, J. Mannhart, and M. Scheffler, *Phys. Rev. Lett.* **120**, 237002 (2018).

[68] M. Thiemann, "Microwave investigations on superconducting Nb-doped $SrTiO_3$", PhD thesis (University of Stuttgart, 2018).

[69] U. S. Pracht, N. Bachar, L. Benfatto, G. Deutscher, E. Farber, M. Dressel, and M. Scheffler, *Phys. Rev. B* **93**, 100503 (2016).

[70] F. Levy-Bertrand, T. Klein, T. Grenet, O. Dupré, A. Benoît, A. Bideaud, O. Bourrion, M. Calvo, A. Catalano, A. Gomez, J. Goupy, L. Grünhaupt, U. v. Luepke, N. Maleeva, F. Valenti, I. M. Pop, and A. Monfardini, *Phys. Rev. B* **99**, 094506 (2019).

[71] N. D. Mathur, F. M. Grosche, S. R. Julian, I. R. Walker, D. M. Freye, R. K. W. Haselwimmer, and G. G. Lonzarich, *Nature* **394**, 39 (1998).

[72] D. N. Basov, R. D. Averitt, D. van der Marel, M. Dressel, and K. Haule, *Rev. Mod. Phys.* **83**, 471 (2011).

[73] U. S. Pracht, "Electrodynamics of quantum-critical conductors and superconductors", PhD thesis (University of Stuttgart, 2017).

[74] S. Goswami, E. Mulazimoglu, A. M. R. V. L. Monteiro, R. Wölbing, D. Koelle, R. Kleiner, Y. M. Blanter, L. M. K. Vandersypen, and A. Caviglia, *Nat. Nanotechnol.* **11**, 861 (2016).

[75] G. Singh, A. Jouan, G. Herranz, M. Scigaj, F. Sanchez, L. Benfatto, S. Caprara, M. Grill, G. Saiz, F. Couedo, C. Feuillet-Palma, J. Lesueur, and N. Bergeal, *Single-band to two-band superconductivity transition in two-dimensional oxide interfaces*, `https://arxiv.org/abs/1806.02212`, Accessed: 27/03/2019.

[76] H. H. Barrett, *J. Appl. Phys.* **35**, 1420 (1964).

[77] S. Giere, M. Kurrat, and U. Schumann, in 20th International Symposium on Discharges and Electrical Insulation in Vacuum (2002), pp. 119–122.

[78] R. V. Latham, *High Voltage Vacuum Insulation: Basic Concepts and Technological Practice* (Academic Press, 1995).

[79] J. N. Reddy, *Introduction to the finite element method* (McGraw-Hill Education - Europe, 2005).

[80] Computer Simulation Technology, *CST MICROWAVE STUDIO (CST MWS)*, `https://www.cst.com/products/cstmws`, Accessed: 11/03/2019.

[81] T. Weiland, *AEU-Int. J. Electron C.* **31**, 3 (1977).

[82] M. Clemens and T. Weiland, *J. Electromagnet. Wave.* **15**, 1 (2001).

[83] CST MICROWAVE STUDIO, *Frequency Domain Solver*, `https://www.cst.com/products/cstmws/solvers/frequencydomainsolver`, Accessed: 11/03/2019.

[84] J. Krupka, K. Derzakowski, A. Abramowicz, M. Tobar, and R. G. Geyer, *Microw. Theory Tech.* **47**, 6 (1999).

[85] L. Wendel, "Dielectric measurements at GHz frequencies", Master thesis (University of Stuttgart, 2019).

[86] M. Kunze, in 2011 IEEE MTT-S International Microwave Symposium (2011), pp. 1–4.

[87] D. C. Mattis and J. Bardeen, *Phys. Rev.* **111**, 412 (1958).

[88] U. S. Pracht, E. Heintze, C. Clauss, D. Hafner, R. Bek, D. Werner, S. Gelhorn, M. Scheffler, M. Dressel, D. Sherman, B. Gorshunov, K. S. Il'in, D. Henrich, and M. Siegel, *IEEE Trans. Terahertz Sci. Technol.* **3**, 269 (2013).

[89] M. Zinßer, "Microwave investigations on $SrTiO_3$-based materials at mK temperatures", Master thesis (University of Stuttgart, 2018).

[90] D. Davoudi, Master thesis (University of Stuttgart, 2019).

[91] A. Farag, Master thesis (University of Stuttgart, 2018).

[92] J. Zhang, S. Alexandrou, and T. Hsiang, *IEEE Trans. Microw. Theory Tech.* **53**, 11 (2005).

[93] S. E. Rowley, L. J. Spalek, R. P. Smith, M. P. M. Dean, M. Itoh, J. F. Scott, G. G. Lonzarich, and S. S. Saxena, *Nat. Phys.* **10**, 367 (2014).

[94] H. A. Wheeler, *Proceedings of the IRE* **30**, 412 (1942).